MEASUREMENT OF THE ELASTIC FORM FACTOR RATIO $\mu G_E/G_M$ USING ELECTRON SCATTERING SPIN ASYMMETRIES

by

Jessica N.A. Campbell

Submitted in partial fulfillment of the requirements
for the degree of Doctor of Philosophy

at

Dalhousie University
Halifax, Nova Scotia
July 2018

Dedicated to my family for their support and love over the years.

Table of Contents

List of Tables . . . . . **v**

List of Figures . . . . . **viii**

Abstract . . . . . **xiv**

Acknowledgements . . . . . **xv**

Chapter 1 Introduction **1**

1.1 Background 1
1.1.1 General 1
1.1.2 Proton Form Factor: Early History 2
1.1.3 Proton Form Factors: Polarization Techniques 3
1.1.4 Proton Form Factors: Focus on Low Q^2 4
1.1.5 JLab Experiment E08-007 6

1.2 Definitions and Formalisms 7
1.2.1 Electron Scattering 7
1.2.2 Formalism 8
1.2.3 Nucleon Form Factors 11
1.2.4 Hadronic Current 12

1.3 Measurement Techniques 14
1.3.1 The Rosenbluth Technique 14
1.3.2 Polarization Transfer Measurements 15
1.3.3 Double Spin Asymmetry Measurements 17
1.3.4 Single Arm Asymmetry Measurements 21

1.4 Motivation for Form Factor Ratio Measurements at Low Q^2 22

1.5 Models and Global Fits 25

Chapter 2 Experiment **31**

2.1 Experimental Setup 31

2.2 Kinematics 31

2.3 CEBAF 33

2.4 Experimental Hall A 35
2.4.1 Rasters 35

2.4.2 Møller Polarimeter . . . 36
2.4.3 Chicane Magnet . . . 37
2.4.4 Septum Magnets . . . 38
2.4.5 High Resolution Spectrometer . . . 38

2.5 Polarized Target . . . 44
2.5.1 Dynamic Nuclear Polarization . . . 44
2.5.2 Target Material . . . 45
2.5.3 Target Setup . . . 46

2.6 Data Acquisition . . . 51

Chapter 3 Analysis . . . 52

3.1 Spectrometer Optics . . . 52
3.1.1 Definition of Coordinate Systems used in Hall A . . . 53
3.1.2 Analysis Coordinate Systems . . . 58
3.1.3 Reaction Variable Reconstruction . . . 59

3.2 Methodology . . . 63
3.2.1 Data Processing . . . 64
3.2.2 Monte Carlo Simulation . . . 64
3.2.3 The Fitting Process . . . 65
3.2.4 Run Lists . . . 79
3.2.5 Uncertainty Analysis . . . 80
3.2.6 Measurement Cuts . . . 85
3.2.7 Asymmetries . . . 91
3.2.8 Experimental Issues . . . 95

Chapter 4 Discussion and Conclusions . . . 103

Appendix A Reaction Component Parameter Values . . . 111

Bibliography . . . 114

List of Tables

2.1 Central kinematics for the left and right HRS where θ is the scattering angle and the star angles are the angles associated with the polarization axis relative to the recoil direction. Note that when the target polarization field is flipped $\phi^*_{new} = 180^\circ$ and $\theta^*_{new} = 180^\circ - \theta^*$. 33

2.2 Main design characteristics of the Hall A high resolution spectrometers showing their resolution and acceptance [46]. 41

3.1 Mean BPM entries are in mm and mrad. 63

3.2 LHRS elastic hydrogen asymmetries for experiment E08-007 reported in Reference [35]. 72

3.3 Convention used for identifying run lists. 79

3.4 Target and beam polarization data for each run list processed for the 2.2 GeV series of runs. 81

3.5 Single arm FFR results for the LHRS and the 2.2 GeV NI run list. Values for μ and M_p are obtained from Reference [87]. . . 84

3.6 Single arm FFR Results for the RHRS and the 2.2 GeV NI run list. Values for μ and M_p are obtained from Reference [87]. . . 84

3.7 DSA FFR Results where RHRS and LHRS are denoted by subscripts 1 and 2, respectively. This is for the 2.2 GeV NI run list. Values for μ and M_p are obtained from Reference [87]. 84

3.8 The initial focal plane momentum cuts for each of the kinematic settings. 85

3.9 P_m and Q^2 cuts algorithm used to investigate the cut-sensitivity of the extracted hydrogen elastic asymmetry. 85

3.10 Physical asymmetry results obtained for the cuts made in Q^2 and P_m on the LHRS Elastic Hydrogen reaction component for Algorithm 3 and run list NI, for the 2.2 GeV setting. 88

3.11 Physical asymmetry results obtained for the cuts made in Q^2 and P_m on the RHRS Elastic Hydrogen reaction component for Algorithm 3 and run list NI, for the 2.2 GeV setting. 88

3.12 Physical asymmetry results obtained for the cuts made in Q^2 and P_m on the LHRS Elastic Hydrogen reaction component for Algorithm 3 and run list NO, for the 2.2 GeV setting. 88

3.13 Physical asymmetry results obtained for the cuts made in Q^2 and P_m on the RHRS Elastic Hydrogen reaction component for Algorithm 3 and run list NO, for the 2.2 GeV setting. 88

3.14 Physical asymmetry results obtained for the cuts made in Q^2 and P_m on the LHRS Elastic Hydrogen reaction component for Algorithm 3 and run list PI, for the 2.2 GeV setting. 89

3.15 Physical asymmetry results obtained for the cuts made in Q^2 and P_m on the RHRS Elastic Hydrogen reaction component for Algorithm 3 and run list PI, for the 2.2 GeV setting. 89

3.16 Physical asymmetry results obtained for the cuts made in Q^2 and P_m on the LHRS Elastic Hydrogen reaction component for Algorithm 3 and run list PO, for the 2.2 GeV setting. 89

3.17 Physical asymmetry results obtained for the cuts made in Q^2 and P_m on the RHRS Elastic Hydrogen reaction component for Algorithm 3 and run list PO, for the 2.2 GeV setting. 89

3.18 The 2.2 GeV physical proton elastic asymmetries extracted via the fit process. 92

3.19 The 2.2 GeV raw proton elastic asymmetries extracted via the fit process. 92

4.1 The 2.2 GeV form factor ratios obtained for the NI and NO run lists generated using DSA and single arm calculations. In addition, an error of 2.3×10^{-5} GeV^2 is associated with the values of Q^2 in the table. 104

4.2 Contribution sources from the differential uncertainty analysis to the overall form factor ratio errors for the 2.2 GeV NI and NO run lists. The form factor ratio partials with respect to a variable 'x' are denoted by "∂_x" and represents the error term $|\partial_x FFR \times \Delta x|$. The percent error is determined by dividing this term by the FFR value and multiply by 100%. Therefore, if these % errors are added in quadrature they result in the ΔFFR values shown in this table. 108

A.1 Fit parameters for the left HRS NI run list for the -1 helicity events. 112

A.2 Fit parameters for the left HRS NI run list for the +1 helicity events. 112
A.3 Fit parameters for the right HRS NI run list for the −1 helicity events. 112
A.4 Fit parameters for the right HRS NI run list for the +1 helicity events. 112
A.5 Fit parameters for the left HRS NO run list for the −1 helicity events. 113
A.6 Fit parameters for the left HRS NO run list for the +1 helicity events. 113
A.7 Fit parameters for the right HRS NO run list for the −1 helicity events. 113
A.8 Fit parameters for the right HRS NO run list for the +1 helicity events. 113

List of Figures

1.1 Data of the proton Electric to Magnetic Form Factor Ratio. The crosses represent older Rosenbluth separation data from a global re-analysis [7], the triangles display the newer polarization transfer data [20, 21, 22] and the most recent JLab Rosenbluth separation data are represented via filled circles [11]. . . 5

1.2 A schematic representation showing the elastic scattering interaction in the lab frame. 8

1.3 Leading order Feynman electron-proton elastic scattering diagram. 9

1.4 The kinematics for the two simultaneous measurements where the scattered electrons e_1 and e_2 are detected in right and left high resolution spectrometer (HRS), respectively. The recoil protons p_1 and p_2 point in the direction of the transferred momenta $\vec{q_1}$ and $\vec{q_2}$, respectively. $\vec{S}$ denotes the target spin direction where θ_1^* and θ_2^* represent the angles with respect to $\vec{q_1}$ and $\vec{q_2}$ in the coordinate frame illustrated in Figure 3.8 [27]. 20

1.5 High precision results of the proton form factor ratio having a total uncertainty of $\sigma_{tot} < 3\%$ compared to several fits and parameterizations [27]. 23

1.6 A summary of some recent proton charge radius determinations: Sick [39], CODATA 2006 [40], Bernauer *el al.* [41], CODATA 2010 [42], and Zhan *el al.* [28] represent results associated with electron-proton scattering experiments. Experiments by Pohl *el al.* [43] and Antognini *el al.* [44] used muonic hydrogen lamb shift. 24

1.7 Ratio $\mu_p G_E^p / G_M^p$ extracted from the polarization transfer (filled blue diamonds) and Rosenbluth method (open red circles). The top/bottom figures show Rosenbluth method data without/with TPE corrections applied to the cross-section data. These figures were obtained from reference [35]. 26

1.8 Fits to nucleon electromagnetic form factors. For G_E^n, data using recoil or target polarization [62] - [68] are shown as filled circles while data obtained from the deuteron quadrupole form factor [69] are shown as open circles. Figure obtained from reference [60]. 29

1.9 Extracted values of G_E and G_M from the global analysis. The open circles are the results of the combined analysis of the cross-section data and polarization measurements. The solid lines are the fits to TPE-corrected cross-section and polarization data. The dotted curves show the results of taking G_E and G_M from a fit to the TPE-uncorrected reduced cross-sections. Figure obtained from Reference [70]. 30

2.1 Schematic diagram of the E08-007 experimental setup [35]. The upper graphic displays a top-down view of the layout of both HRS arms while the lower graphic displays a lateral view of the same. These illustrations show the individual placement of the equipment along the beam line. 32

2.2 Schematic of the Jefferson Lab continuous electron beam accelerator facility (CEBAF). This system consists of two linacs that are connected by recirculation arcs (magnets) that are used to accelerate the electron beam to higher energies for experimental purposes. 34

2.3 Schematic cross section of Hall A with one of the HRS spectrometers in the (fictitious) 0° position [46]. 35

2.4 The fast and slow raster patterns are shown respectively in the left and right images. They illustrate the distribution of the beam over the surface of the target as indicated by the green and blue that respectively represent greater and lesser degrees of intensity in these images [35]. 36

2.5 The two chicane magnets used to bend the beam. 38

2.6 Illustration of septum magnets [35]. 39

2.7 Layout of the detector package. The arrow illustrates particle trajectories. 39

2.8 Layout of the HRS magnetic and detection systems in Hall A [35]. 40

2.9 Schematic layout of a pair of Vertical Drift Chambers for one HRS. The active area of each wire plane is rectangular and has a size of 2118 mm x 288 mm. Each VDC consists of a single U and V wire plane with the lower VDC positioned as close as possible to the spectrometer's focal plane [46]. 43

2.10 Layout of the scintillator planes used in the E08-007 experiment [35]. 43

2.11 Schematic of the target assembly and its major components. This figure illustrates the location of the target, the location of the beam's input and the target polarization field orientation, as well as the NMR coil used to measure the target's polarization. Also shown, are the major refrigeration elements and the access points used to inject the microwave input and retrieve the NMR output signals from this assembly [35]. 47

2.12 This figure shows the vertical orientation of the target insert shown in Figure 2.11 along with the placement of each of its target cells. In particular, it highlights the locations associated with the top and bottom NH_3 targets, the carbon and dummy targets, as well as the CH_2 target and the position of the carbon holes [73]. 50

3.1 Geometric configuration of the sieve slit where dimensions are given in mm. The two large holes in the plate are used to determine the orientation of the sieve slit and have a diameter of 2.7 mm. The smaller sized holes have a diameter of 1.4 mm [78]. 53

3.2 Hall A Coordinate System [77]. 54

3.3 Target Coordinate System [28]. 55

3.4 Vertical Drift Chamber Detector Coordinate System [77]. . . . 56

3.5 Four planes of the VDC [77]. 56

3.6 Vertical Drift Chamber Transport Coordinate System [77]. . . 57

3.7 The Focal Plane Coordinate System (FCS). [77]. 57

3.8 Coordinate systems for the scattering of polarized electrons from polarized target. In this figure, the vectors $\vec{u}_N$ and $\vec{u}_L$ are respectively normal to the scattering plane and parallel to $\vec{k}$ with $\vec{u}_S = \vec{u}_N \times \vec{u}_L$. The starred coordinate system is defined by vectors $\vec{u}_z = \vec{q}$, $\vec{u}_y = \vec{k} \times \vec{k}'$, and $\vec{u}_x = \vec{u}_y \times \vec{u}_z$. Illustration taken from Reference [36]. 59

3.9 Left HRS and right HRS positional distributions of the data when observed in the focal plane coordinate system. 61

3.10 Left HRS and right HRS positional distributions of the data when observed in the target coordinate system. 62

3.11 These plots illustrate the visual placement of each reaction component using vertical dashed lines (momentum markers) to support the fitting process. Each reaction component is plotted using a different colour. Elastic H, He, and N are respectively plotted as purple, dark green, and cyan. The quasi-elastic He and N show up as magenta and brown. In addition, the blue dots/curve represents the measured data. 68

3.12 LHRS histograms showing the results for eleven and seven parameter fits. The top plot shows the fit results when all reaction components are shifted as a single unit but are free to scale and skew independently when being fit. The bottom plot shows the case when they are skewed and shifted as a single unit but scaled independently of each other. The description in Figure 3.11 provides a legend for the reaction components. The overall fit model is represented by the black curve. 71

3.13 The 2.2 GeV baseline run-pair physical asymmetry results for the LHRS and RHRS are plotted for each initialization algorithm. The points encompassed in the blue circle contain two groupings with four entries. The first and second group of four entries represent the LHRS and RHRS asymmetries, respectively. Within one grouping the colours represent the cuts in momentum: None (blue), Large (red), Medium (green), and Small (pink). In addition, each grouping of the LHRS and RHRS results are associated with similar cuts in Q^2 defined along the x-axis of the plot. The definition of these cuts is described in Table 3.9 of Section 3.2.6. 73

3.14 The 2.2 GeV baseline run-pair fits for the +1 helicity spectra associated with each arm of the spectrometer. The black curves in the plots represent the fitted model, the blue curve represents the measured data, while the colour of each reaction component is provided in the caption of Figure 3.11. 75

3.15 The 2.2 GeV baseline run-pair fits for the −1 helicity spectra associated with each arm of the spectrometer. The black curves in the plots represent the fitted model, the blue curve represents the measured data, while the colour of each reaction component is provided in the caption of Figure 3.11. 76

3.16 The 2.2 GeV fits for the +1 helicity measurements for each arm of the spectrometer for run list NI. The blue curves represent the measured data, the black curves in the plots represent the fitted model while the magenta and purple curves represent the estimated background and elastic hydrogen reaction component associated with each fit, respectively. 77

3.17 The 2.2 GeV fits for the −1 helicity measurements for each arm of the spectrometer for run list NI. The blue curves represent the measured data, the black curves in the plots represent the fitted model while the magenta and purple curves represent the estimated background and elastic hydrogen reaction component associated with each fit, respectively. 78

3.18 This figure shows the cuts made in P_m for the left and right arms of the spectrometer. These cuts are identified as being None, Large, Medium, and Small delineated respectively by vertical lines that are black, red, green, and blue. The horizontal axis units are in GeV for P_m. These plots are for the 2.2 GeV NI run list. 86

3.19 This figure shows the cuts made in Q^2 for the left and right arms of the spectrometer. These cuts are identified as being None, Large, Medium, and Small delineated respectively by vertical lines that are black, red, green, and blue. The horizontal axis units are in GeV^2 for Q^2. These plots are for the 2.2 GeV NI run list. 87

3.20 The LHRS and RHRS Q^2 simulated distributions for the elastic hydrogen events using a medium cut in P_m. The distribution having no cuts is indicated in red while the one in blue shows the effect of the cut for the 2.2 GeV setting. 90

3.21 The 2.2 GeV physical asymmetries extracted via the fit process for each run list and spectrometer arm. Estimated means and standard deviations for each arm of the spectrometer are provided on the plot. The mean asymmetries are plotted and indicated by the coloured dashed curves. 93

3.22 The 2.2 GeV physical asymmetries extracted for each run list via the fit process for the LHRS are replotted from Figure 3.21. Also plotted are the asymmetries obtained for the lower and upper Q^2 cut regions from Reference [35]. These regions are delineated by ($Q2$:LC) and ($Q2$:UC), respectively. The mean run list asymmetry lies between the Reference [35] results as indicated by the blue dashed line. 94

3.23 The 1.7 GeV baseline run-pair fits for the +1 helicity spectra associated with each spectrometer. The black curves in the plots represent the fitted model while the colour of each reaction component is provided in the caption of Figure 3.11. 96

3.24 The 1.7 GeV baseline run-pair fits for the −1 helicity spectra associated with each spectrometer. The black curves in the plots represent the fitted model while the colour of each reaction component is provided in the caption of Figure 3.11. 97

3.25 The simulated LHRS and RHRS scattering angle distributions for the 1.1 GeV kinematic created using the mean beam data provided in Table 3.1. 98

3.26 The 2.2 GeV simulated Q^2 distributions for LHRS and RHRS created using the mean beam data provided in Table 3.1 are shown in the top two plots of this figure. The perfect beam alignment results are shown in the bottom two plots. 100

3.27 The 1.7 GeV simulated Q^2 distributions for LHRS and RHRS created using the mean beam data provided in Table 3.1 are shown in the top two plots of this figure. The perfect beam alignment results are shown in the bottom two plots. 101

3.28 The 1.1 GeV simulated Q^2 distributions for LHRS and RHRS created using the mean beam data provided in Table 3.1 are shown in the top two plots of this figure. The perfect beam alignment results are shown in the bottom two plots. 102

4.1 The 2.2 GeV single arm form factor ratios from Table 4.1 are plotted along with the established body of data. The left graphic contains the individual run list results while the right graphic shows the averaged results for the LHRS and the RHRS. . . . 106

4.2 The 2.2 GeV single arm form factor ratios from Table 4.1 are plotted with recent world data [2, 23, 28, 88] and the Carlson Model results [38]. The top graphic contains the individual run list results while the bottom graphic shows the averaged results for the LHRS and the RHRS. 107

4.3 The 2.2 GeV form factor ratio as a function of the asymmetry ratio A_1/A_2 using the data found in Table 3.7 and Equation 1.61. An asymptote exists at x_o and the form factor ratio is plotted as the blue square. 109

Abstract

Electron scattering is a powerful tool for studying the internal structure of the proton. In particular, elastic electron-proton scattering is used to access the electromagnetic form factors (G_E and G_M) due to an implied connection between the spatial distribution of the proton's charge and magnetism to the form factors' dependence on the scattering momentum transfer (Q^2). This focus was spurred by experimental developments of polarization parameters in scattering to access the elastic form factor ratio (FFR $= \mu\, G_E/G_M$). There is a renewed interest in the low Q^2 region where the FFR can only be described by QCD-inspired models and phenomenological fits that are sensitive to the long-range structure of the proton. This is important because the form factors' Q^2 slope, as Q^2 tends to zero, defines the proton's radius.

This thesis reports on a novel method to analyze and extract the proton elastic FFR at the lowest Q^2 range ever attempted ($0.01 \leq Q^2 \leq 0.08$ GeV^2) from an experiment conducted in 2012 at Jefferson Lab (E08-007). The experiment used a polarized electron beam, a polarized proton target, and two high resolution spectrometers (HRS) to detect scattered electrons at $\approx 6^\circ$ on either side of the beam (left, right) for independent measurements. A previous independent analysis had been conducted on the left HRS data, but experimental difficulties prevented that analysis from extracting the FFR, but provided polarization asymmetries for the left HRS.

Our analysis method did not rely on the standard use of the magnetic optical transformation matrix. The analysis utilized the measured momentum distributions from the scattering reactions. A Monte Carlo simulation of the experiment was used to model and fit the observed momentum distributions to extract the FFR. While this method did not yield a reliable FFR result for the right HRS, it was able to confirm the left HRS asymmetry found in the previous analysis and extracted one value at $Q^2 = 0.0513$ GeV^2 for $\mu\, G_E/G_M = 1.147 \pm 0.017$. This result indicates an upward trend in the ratio as Q^2 approaches zero, since it is significantly higher than existing data at low Q^2. Given the connection of the low Q^2 form factor slope to the proton size, the result of this thesis points to a need for follow-up measurements.

Acknowledgements

I would like to thank Dr. Adam Sarty for being my supervisor and for his guidance, motivation, and support. I would like to give thanks to everyone at Jefferson Lab for their help including Dr. Doug Higinbotham, the g_p^2 students, and Dr. Moshe Friedman. Last but not least, I would like to thank my family and friends for their love, encouragement, and support over these last few years.

Chapter 1

Introduction

1.1 Background

1.1.1 General

Nuclear physics experiments are used to study the fundamental constituents of matter and their interactions. The first modern model of the atom was proposed by Ernest Rutherford whose alpha-scattering experiments pointed to the atom being composed of a densely charged core surrounded by an electron cloud. We now understand that this core, or nucleus, is composed of neutrons and protons. These particles (protons and neutrons—collectively called nucleons) were discovered in 1919 and 1931, respectively, and account for 99.9% of an atom's mass. Unraveling the internal structure of these nucleons was, and still is, one of the most challenging fundamental questions in modern physics.

Originally, nucleons were believed to be Dirac particles that were predicted to have a Dirac magnetic moment μ similar to that of an electron given by:

$$\mu = \frac{q}{mc}|\vec{S}| \tag{1.1}$$

where the speed of light c, the magnetic moment μ, the electric charge q, the mass m, and the spin $\vec{S}$ of the particle are used to define this moment. However, modern measurements of μ provide indications of nucleonic substructure. In particular, the measurements made by O. Stern *et al.* [1] provided the first conclusive evidence confirming that protons exhibited an internal substructure, having a magnetic moment:

$$\mu_p = 2.79\,\mu_N \tag{1.2}$$

where μ_N is the nuclear magneton[1]. This observation directly contradicts (1.1) and

[1]The nuclear magneton is defined in terms of the proton mass m_p, the speed of light c, Plank's constant $\hbar$, and the electron's charge e as: $\mu_N = \frac{e\hbar}{2m_pc}$.

its underlying assumption of the proton being a structureless Dirac particle, with the consequence that these particles must have some form of internal structure.

The fundamental properties of nucleons, and therefore of nuclei, are governed by this internal structure. In the simplest picture, nucleons are composed of three bound valence quarks that interact through the exchange of virtual gluons. This model is the theory of the strong interaction, also known as quantum chromodynamics (QCD). This theory can be used to make rigorous predictions when quarks become asymptotically free, which occurs when the four-momentum transfer squared Q^2 is large, which is sensitive to decreasingly small spatial extents. Unlike quantum electrodynamics (QED), the coupling to gluons in QCD is strong and increases as the energy decreases and the distance scale probed increases. As a result, particle confinement dominates at low-energies. The strong coupling of QCD at low energies prevents the perturbative expansions used in QED. Consequently, no exact analytic solutions of QCD are forthcoming, so several phenomenological models are used in an attempt to explain the data in this domain. As a result, precise measurements of the nucleon form factors are desired in order to constrain and test these models.

1.1.2 Proton Form Factor: Early History

In the 1950s, electron scattering was used as a precise and powerful tool for studying internal nuclear structure. The electron interacts with the nucleus through the electromagnetic interaction, which is well understood through QED. This interaction is both weak and dominated by the one-photon-exchange (OPE) process. In the approximation of this process, the electron-proton elastic scattering cross-section can be expressed in terms of the electric G_E and magnetic G_M form factors as a function of Q^2. As a result, electron scattering experiments allow one to unravel the distributions of the electric charge and magnetization in nucleons. These experiments have had a rich history over the past half century in that they have provided measurements of the proton charge radius and a detailed mapping of the elastic form factors over a wide range of Q^2 [2].

For over 40 years, the Rosenbluth separation technique based upon using unpolarized electron-proton scattering cross-sections has dominated form factor studies (this technique is detailed later in Section 1.3). Experiments based on this technique show

that both G_E^p and G_M^p roughly follow the dipole form factor parameterization model [3]. This approximation showed that the nucleon form factors, with the exception that $G_E^n \to 0$ when $Q^2 \to 0$, approximately follow the dipole form factor given by,

$$G_D = \left(1 + \frac{Q^2}{\lambda_D^2}\right)^{-2} \tag{1.3}$$

where the empirical parameter $\lambda_D^2 \approx 0.71$ GeV^2 is identical for the proton and neutron form factors G_E^p, G_M^p, and G_M^n resulting in $G_E^p \approx G_D$ and $G_M^{p,n} \approx \mu'_{p,n} G_D$ with $\mu'_{p,n} = \mu_{p,n}/\mu_N$. To a good approximation these form factors then satisfy the following relationships [4],

$$\begin{aligned} G_E^p(Q^2) &\approx \frac{G_M^p(Q^2)}{\mu'_p} \approx \frac{G_M^n(Q^2)}{\mu'_n} = G_D(Q^2) \\ G_E^n &\approx 0 \end{aligned} \tag{1.4}$$

These form factors tend to unity when divided by G_D and differ only by an overall scale factor based upon their magnetic moments. This behaviour suggests that G_E^p and G_M^p have similar spatial distributions.

Experiments performed in the 1960s and 70s using the Rosenbluth technique started to show deviations from the dipole formula in (1.3). Studies performed by Bartel *et al.* [5] and Berger *et al.* [6] both showed deviations at high Q^2 for G_E^p and G_M^p [7]. However, these measurements were not precise. Experiments performed later at SLAC [8, 9] and JLab [10, 11] measured more precise cross-sections and agreed to within 10% of the values predicted by the dipole formula at high Q^2 (more discussion on this topic appears later in this sub-section). Also, later in the 1970s, more precise proton cross-section measurements at low Q^2 were made [12, 13, 14]. These low Q^2 studies also observed deviations from the dipole formula; nevertheless, these observations appear to have had little impact at the time because of the shift in focus to the high Q^2 regime and the determination of G_E^n form factors [7].

1.1.3 Proton Form Factors: Polarization Techniques

Advances in the technology of intense polarized electron beams, polarized targets, and polarimetry have ushered in a new generation of electron scattering experiments that rely on spin degrees of freedom. Compared to cross-section measurements, polarization techniques have several distinct advantages. First, they have increased

sensitivity to small effects by observing the interference between large and small amplitudes of interest. For example, the polarized cross-section for electron-proton scattering contains a mixed term proportional to $G_E G_M$, which is absent in unpolarized cross-sections [2]. Secondly, spin-dependent experiments involve the measurement of polarization or helicity asymmetries, and these asymmetries are independent of the cross-section normalization. To first order, this eliminates the effects of luminosity, detection acceptance, and detector efficiency. Other systematics such as beam and target polarization, or polarimeter analyzing power, can also be canceled by measuring a ratio of polarization observables [2].

The first experiment to measure the recoil proton polarization observable in electron-proton elastic scattering was done at SLAC by Alguard [15]. However, the results of the experiment were limited by low statistics. In addition, other proof-of-principle proton form factor measurements using recoil polarimetry were carried out at MIT-Bates [16, 17] and MAMI [18, 19]. Due to limited statistics and kinematics coverage, these form factor ratios were found to agree, within uncertainties, with the earlier unpolarized measurements.

More recent measurements using the recoil polarization method to measure the proton form factor ratio [20, 21, 22, 23] at high Q^2, have better precision and deviate dramatically from the unpolarized data as seen in Figure 1.1. This has prompted intense theoretical and experimental activities over the last 15 years to resolve these discrepancies. The validity of analyzing data in the OPE approximation has been questioned. However, it is now generally accepted that the two-photon exchange (TPE) processes are considered as a significant correction to the unpolarized data, and mostly account for the discrepancy at high Q^2 [7]. As a result, it is believed that the two-photon exchange corrections have little impact on the polarization technique for determining form factors but do have a large impact on the Rosenbluth extraction of the electric form factor contribution at high Q^2.

1.1.4 Proton Form Factors: Focus on Low Q^2

While measurements at large momentum transfer have provided information on the details of the proton structure in regions sensitive to smaller spatial extents (approaching the QCD realm), the low Q^2 form factor behaviour is sensitive to the

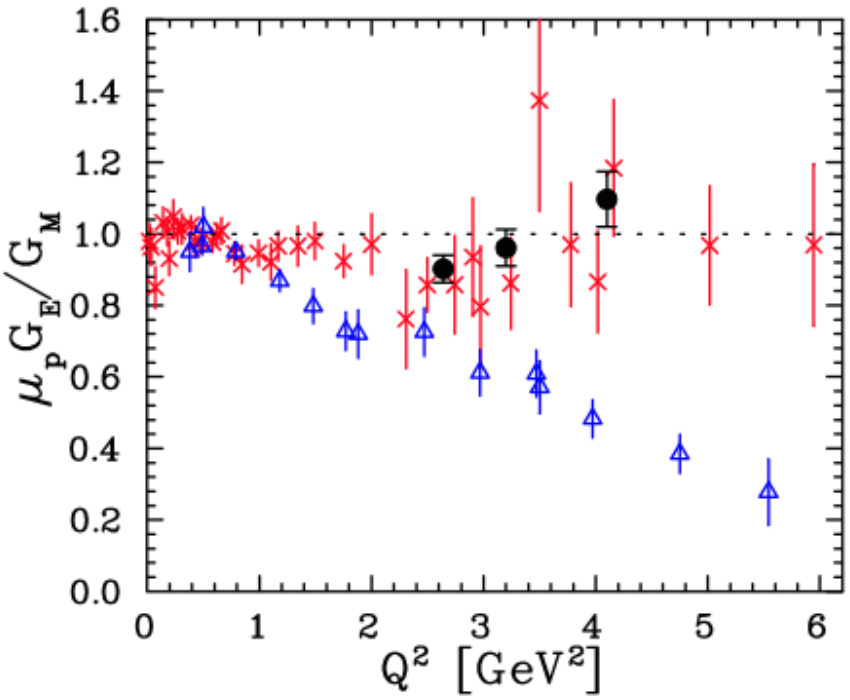

Figure 1.1: Data of the proton Electric to Magnetic Form Factor Ratio. The crosses represent older Rosenbluth separation data from a global re-analysis [7], the triangles display the newer polarization transfer data [20, 21, 22] and the most recent JLab Rosenbluth separation data are represented via filled circles [11].

long-range structure where the best descriptions show dominance of the 'pion cloud' [24]. High-precision measurements at low Q^2 were initially motivated by a recent semi-phenomenological fit [25], which suggested that structure might be present in all four nucleon form factors at[2] $Q^2 \approx 0.3$ GeV^2 [24]. However, later polarization measurements from MIT-Bates [2] and JLab [26] that probed the low Q^2 region with a precision of approximately 2% found no indication of such structure in the form factor ratio $\mu_p G_E^p/G_M^p$ [24].

The proton form factor ratio behaviour at low Q^2 has become the subject of considerable interest after a potential discrepancy was observed from the most recent high precision measurements for $Q^2 < 1$ GeV^2. BLAST [2] conducted the first proton form factor ratio measurements using beam-target asymmetry for a Q^2 range of $0.15 - 0.65$ GeV^2 and found them to be consistent with $\mu_p G_E^p/G_M^p \to 1$. Nonetheless, the LEDEX experiment at JLab used recoil polarimetry and observed a substantial deviation from unity at $Q^2 \approx 0.35$ GeV^2 [26]. However, the LEDEX data quality was compromised due to background issues and the low degree of beam polarization. As a result, it was necessary to carry out new high precision measurements to either confirm or refute these observations.

1.1.5 JLab Experiment E08-007

To meet this requirement, in 2012 experiment E08-007 was conducted in Hall A of the Thomas Jefferson National Accelerator facility (JLab) in Newport News, VA, USA [27]. This experiment had two separate components. The first part of this experiment measured the proton form factor ratio $\mu_p G_E^p/G_M^p$ over a Q^2 range of $0.3 - 0.7$ GeV^2 using recoil polarimetry. This new data set has been analyzed and published [24, 28] and had two major implications. First, previous measurements had suggested that the ratio was flat up until $Q^2 \approx 0.2$ GeV^2 prior to decreasing, which further implied that the form factors had identical low Q^2 behaviour suggesting that the charge and magnetization radii for the proton were equal. However, this experiment observed that the form factor ratio was significantly below unity over the entire Q^2 range for this data set and there was no indication that the ratio approached unity noticeably

[2]The units of Q^2 and energy used in this report assume natural units of $\hbar = c = \epsilon_0 = 1$ and are given repeatedly as GeV^2 and GeV.

above $Q^2 = 0$. Secondly, there was also no indication of any structure in the form factor ratio over the Q^2 range of these high precision measurements.

The analysis and results of the second component of experiment E08-007 are the principle focus reported in this thesis. This component of the experiment measured the proton form factor ratio $\mu_p G_E^p/G_M^p$ over a Q^2 range of $0.01 - 0.08$ GeV^2 using the Double Spin Asymmetry (DSA) and the single beam asymmetry techniques, utilizing a polarized electron beam and a polarized proton target. The relevant theoretical background and terminology are provided in the remaining sections of Chapter 1. The experimental setup, kinematics, target preparation, and data acquisition systems are described in Chapter 2. Chapter 3 describes the data analysis process used and discusses experimental issues. Finally, Chapter 4 summarizes the overall results achieved and presents final conclusions along with recommendations to support further experimental research in this field of study.

1.2 Definitions and Formalisms

The following sections cover the fundamental definitions and topics that relate to the the descriptions and formalisms of the elastic scattering process, the electromagnetic form factors, and hadronic currents.

1.2.1 Electron Scattering

Elastic scattering of electrons in the OPE, or Born, approximation is a simple process that conserves both energy and momentum. In QED, the leading order approximation for electron-proton elastic scattering is described by the exchange of a single virtual photon γ^* in the field of the nucleus. As a result, an incident electron of energy E and momentum $\vec{k}$ emits a photon that carries the momentum $\vec{q}$ and the energy ω lost by the electron during the scattering process. This photon is absorbed by a component of the nucleus in a fundamental process described by QED [29]. Consequently, this process is ideal for probing the electromagnetic structure of the nucleus. The incident electron is deflected by an angle θ having a scattered energy E' and momentum $\vec{k}'$. This process is illustrated in Figure 1.2.

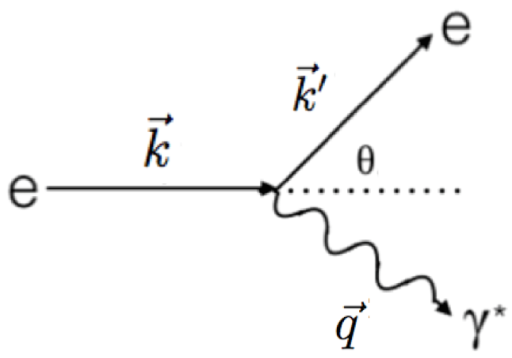

Figure 1.2: A schematic representation showing the elastic scattering interaction in the lab frame.

In the lab frame, the four momentum transfer q^μ is defined by [29]:

$$\left.\begin{array}{rcl} q^\mu & = & (\omega, \vec{q}) \\ \omega & = & E - E' \\ \vec{q} & = & \vec{k} - \vec{k}' \end{array}\right\} \tag{1.5}$$

The angle through which the electron is scattered is related to the momentum transferred by the photon from the electron to the nucleon by:

$$q^2 = -4\,E\,E'\,\sin^2\,(\theta/2) \tag{1.6}$$

where the mass of the electron has been neglected and $q^2 = \sum_\mu q^\mu q_\mu$. For convenience, the four momentum transfer Q^2 is defined to be positive, i.e.,

$$Q^2 = -q^2\ = -(\omega^2 - \vec{q}^{\,2}) \tag{1.7}$$

The OPE approximation is justified at low momentum transfer based upon the small electromagnetic coupling constant[3] α; however, it is not valid above $Q^2 \approx 1$ GeV^2 for the same reason as stated in the previously noted discrepancies between cross-section and polarization measurements [7]. For these reasons, the approximation is considered valid for the primary focus of this work.

1.2.2 Formalism

The OPE amplitude for the electron-proton elastic scattering is determined from the Feynman diagram in Figure 1.3. This figure shows the four-momenta associated with

[3]This constant is also know as the electromagnetic fine structure constant and has a value of $\alpha = e^2/4\pi \approx 1/137$ written in natural units of $\hbar = c = \epsilon_0 = 1$.

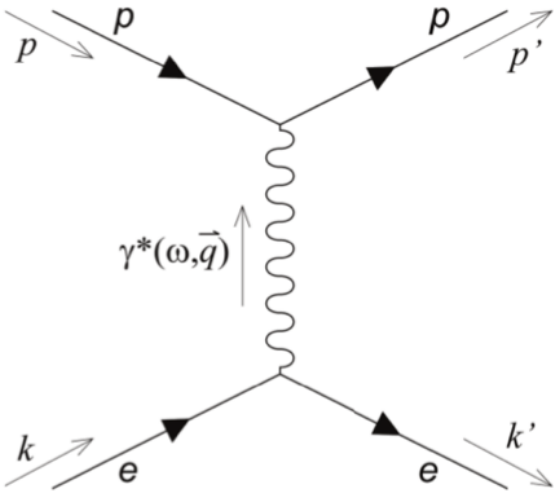

Figure 1.3: Leading order Feynman electron-proton elastic scattering diagram.

the electron (k, k') and the proton (p, p') that results from the exchange of the virtual photon $\gamma^*(\omega, \vec{q})$. One of the advantages of using electrons as an electromagnetic probe lies in the fact that the leptonic vertex $e(k) \rightarrow e(k') + \gamma^*(q)$ is fully described by QED. Furthermore, the information that relates to the unknown electromagnetic properties of the nucleon are solely contained by the hadronic vertex $\gamma^*(q) + P(p) \rightarrow P(p')$. In the OPE process, the elastic scattering amplitude can be written as the product of the leptonic ℓ_μ and hadronic $\mathcal{J}_\mu$ currents [3]. Using this Feynman diagram, the elastic scattering amplitude is represented by the following expression:

$$\begin{aligned} i\,\mathcal{M} &= \left[i\,e\,\bar{v}\,(p')\;\Gamma^{\mu}\,(p',p)\;v\,(p)\right]\;\frac{-i\,g_{\mu\nu}}{q^2}\left[ie\bar{u}\,(k')\,\gamma^{\nu}u\,(k)\right] \\ &= -\frac{i}{q^2}\left[i\,e\,\bar{v}\,(p')\;\Gamma^{\mu}\,(p',p)\;v\,(p)\right]\;\left[i\,e\,\bar{u}\,(k')\;\gamma_{\mu}\,u\,(k)\right], \end{aligned} \tag{1.8}$$

where $g_{\mu\nu}$ is the metric tensor and the γ^μ terms represent the following Dirac matrices[4]:

$$\gamma^0 = \begin{pmatrix} \mathbf{0} & \mathbf{I} \\ \mathbf{I} & \mathbf{0} \end{pmatrix}; \quad \gamma^i = \begin{pmatrix} \mathbf{0} & \sigma_i \\ -\sigma_i & \mathbf{0} \end{pmatrix} \tag{1.9}$$

where $\mathbf{0}$ and $\mathbf{I}$ denote 2×2 null and identity matrices, respectively. The σ_i's represent the following three Pauli matrices:

$$\sigma_x = \begin{pmatrix} 0 & 1 \\ 1 & 0 \end{pmatrix}; \quad \sigma_y = \begin{pmatrix} 0 & -i \\ i & 0 \end{pmatrix}; \quad \sigma_z = \begin{pmatrix} 1 & 0 \\ 0 & -1 \end{pmatrix}. \tag{1.10}$$

[4]The Dirac matrices are shown in the Weyl or chiral basis.

The initial and final electron Dirac four-spinors are represented by the functions $u(k)$ and $\bar{u}(k')$, respectively. While the target and recoil proton Dirac four-spinors are correspondingly given by $v(p)$ and $\bar{v}(p')$. The wave-functions associated with spin-1/2 particles are represented by plane-waves $\psi(x)=v(p)\,e^{-i\,p_\mu x^\mu}$ that satisfy the Dirac equation[5]:

$$(-i\,\gamma^\mu\,\partial_\mu - m)\;\psi(x) = 0 \tag{1.11}$$

Solutions to this equation have the following form:

$$v(p) = \begin{bmatrix} \sqrt{p_\mu \cdot \sigma^\mu}\,\chi \\ \sqrt{p_\mu \cdot \bar{\sigma}^\mu}\,\chi \end{bmatrix} \tag{1.12}$$

where χ is a normalized two-spinor such that $\chi^\dagger\chi = 1$ and the four-vectors $\sigma^\mu = (\mathbf{I},\ \vec{\sigma})$ and $\bar{\sigma} = (\mathbf{I}, -\vec{\sigma})$ are defined in terms of the Pauli vector $\vec{\sigma} = (\sigma_x, \sigma_y, \sigma_z)$. While QED fully describes the leptonic current $\ell_\mu = ie\,\bar{u}\,(k')\;\gamma_\mu\,u\,(k)$, the hadronic current $\mathcal{J}^\mu = ie\,\bar{v}\,(p')\;\Gamma^\mu\,(p',p)\;v\,(p)$ contains the additional factor $\Gamma^\mu\,(p',p)$. This factor represents the information about the internal electromagnetic structure of the proton, which is not known in QED. The symmetries of the electromagnetic interaction implies that the most general form of Γ^μ is a linear combination of p, p', and γ^μ in addition to containing constants such as the proton mass m and the electric charge e. Since the hadronic current transforms as a vector, Γ^μ must be a linear combination of these vectors having coefficients that are solely functions of Q^2. That is,

$$\Gamma^\mu = \gamma^\mu\,F_1\left(Q^2\right) + i\,\frac{\sigma^{\mu\nu}}{2M_p}\,\kappa_p\,F_2\left(Q^2\right)\,. \tag{1.13}$$

Using this results in the following expression for the hadronic current [30]:

$$\mathcal{J}^\mu = ie\,\bar{v}\,(p')\;\left[\gamma^\mu\,F_1\left(Q^2\right) + i\,\frac{\sigma^{\mu\nu}}{2M_p}\,\kappa_p\,F_2\left(Q^2\right)\right]\;v\,(p) \tag{1.14}$$

where $\sigma^{\mu\nu} = \frac{i}{2}[\gamma^\mu, \gamma^\nu]$, κ_p is the proton anomalous magnetic moment, and $F_{1,2}\,(Q^2)$ are the proton elastic form factors. All of the information concerning the electromagnetic structure of the proton are therefore contained in these form factors.

[5]This equation is written in natural units of $\hbar = c = \epsilon_0 = 1$, where these constants are included in the specific units implemented.

1.2.3 Nucleon Form Factors

Since the elastic scattering cross-section is proportional to the square of the amplitude, it can be expressed in terms of the form factors, as a function of Q^2. The Dirac and Pauli form factors are denoted by $F_1(Q^2)$ and $F_2(Q^2)$, respectively. They are distinguished according to their helicity states, which is defined as the projection of the electron's spin along its direction of momentum. The Dirac form factor $F_1(Q^2)$ represents the helicity preserving part of the scattering process, while the Pauli form factor $F_2(Q^2)$ represents the helicity flipping part. These form factors are usually normalized according to their static properties at $Q^2=0$. Specifically, for the proton:

$$F_1^p = 1 \quad F_2^p = 1 \tag{1.15}$$

and for the neutron:

$$F_1^n = 0 \quad F_2^n = 1 \tag{1.16}$$

An alternative definition of the form factors provided by Sachs [31] conveniently links experimental observation with theoretical analysis. In particular, the distribution of electric charge within the nucleus and the magnetization over the volume of the nucleus are described by the respective functions G_E and G_M. These functions are expressed in the following form:

$$G_E = F_1 - \tau\kappa F_2 \tag{1.17}$$

$$G_M = F_1 + \kappa F_2 \tag{1.18}$$

with the kinematic factor $\tau = \frac{Q^2}{4m^2}$ and κ is the nucleon anomalous magnetic moment. The Sachs form factors allow for a more simple physical interpretation when they are expressed in the Breit reference frame, described below in Section 1.2.4. These form factors are normalized according to the static properties of the corresponding nucleon at $Q^2=0$. That is,

$$G_E^p(0) = 1 \quad G_M^p(0) = \mu_p \tag{1.19}$$

$$G_E^n(0) = 0 \quad G_M^n(0) = \mu_n \tag{1.20}$$

where $\mu_p = 2.79\,\mu_N$ and $\mu_n = 1.91\,\mu_N$ are respectively the magnetic moments of the proton and neutron in units of the nuclear magneton μ_N.

1.2.4 Hadronic Current

The physical meaning of the electric and magnetic form factors, G_E and G_M, are best understood when the hadronic current is written in the Breit frame[6] [3]. In this frame of reference, scattered electrons only transfer momentum $\vec{q_B}$ not energy ($\omega_B = 0$). As a result, the proton undergoes only a change in its momentum. Specifically, it undergoes a change from $-\vec{q_B}/2$ to $+\vec{q_B}/2$. Consequently, the initial and final nucleon momenta are equal and opposite in this framework resulting in a simplified interpretation of the the hadronic current[7]. Using the Gordon identity [30]:

$$\bar{v}(p')\,\gamma^\mu\,v(p) = \bar{v}(p')\left[\frac{p'^\mu + p^\mu}{2M_p} + \frac{i\,\sigma^{\mu\nu}\,q_\nu}{2M_p}\right]v(p) \tag{1.21}$$

allows the $(p' + p)$ term to be swapped for the one involving the $\sigma^{\mu\nu}\,q_\nu$. Doing so results in the following expression in terms of the Dirac and Pauli form factors:

$$\mathcal{J}^\mu = \bar{v}(p')\,\Gamma^\mu\,v(p) = \bar{v}(p')\left[(F_1 + \kappa\,F_2)\,\gamma^\mu - \frac{(p+p')^\mu}{2M_p}\,\kappa\,F_2\right]v(p) \tag{1.22}$$

Consequently, the time and spacial components of the hadronic current in this framework are respectively given by:

$$\mathcal{J}^0 = i\,e\,\bar{v}(p')\left[(F_1 + \kappa\,F_2)\,\gamma^0 - \frac{E_{pB}}{M_p}\,\kappa F_2\right]v(p) \tag{1.23}$$

$$\vec{\mathcal{J}} = i\,e\,(F_1 + \kappa\,F_2)\,\bar{v}(p')\,\vec{\gamma}\,v(p) \tag{1.24}$$

where $\vec{\gamma} = (\gamma^1, \gamma^2, \gamma^3)$ and E_{pB} is the proton energy. Using the expression $\bar{v}(p') = v^\dagger(p')\,\gamma^0$ results in a time component $\mathcal{J}^0$ having the following form:

$$\mathcal{J}^0 = i\,e\,\left[(F_1 + \kappa\,F_2)\,v^\dagger(p')\,v(p) - \kappa\,F_2\frac{E_{pB}}{M_p}\,v^\dagger(p')\,\gamma^0\,v(p)\right] \tag{1.25}$$

[6] Variables in the Breit reference frame are denoted with a subscript B.

[7] In a Breit frame, the interaction only flips the sign of the nucleon three momentum vector.

Furthermore, using the definitions of $v(p)$ and γ^0 from (1.9) and (1.12) gives:

$$\begin{aligned}\mathcal{J}^0 = & i\,e\,(F_1+\kappa\,F_2)\,\chi'^{\dagger}\left(\sqrt{p'_\mu\cdot\sigma^\mu}\,\sqrt{p'_\mu\cdot\bar{\sigma}^\mu}\right)\begin{pmatrix}\sqrt{p_\mu\cdot\sigma^\mu}\,\chi\\ \sqrt{p_\mu\cdot\bar{\sigma}^\mu}\,\chi\end{pmatrix}\\ & -i\,e\,\kappa\,F_2\,\frac{E_{pB}}{M_p}\,\chi'\left(\sqrt{p'_\mu\cdot\sigma^\mu}\,\sqrt{p'_\mu\cdot\bar{\sigma}^\mu}\right)\begin{pmatrix}0 & 1\\ 1 & 0\end{pmatrix}\begin{pmatrix}\sqrt{p_\mu\cdot\sigma^\mu}\,\chi\\ \sqrt{p_\mu\cdot\bar{\sigma}^\mu}\,\chi\end{pmatrix}.\end{aligned} \tag{1.26}$$

Using the following identities:

$$M_p = \sqrt{p'_\mu\cdot\sigma^\mu}\cdot\sqrt{p_\mu\cdot\sigma^\mu} = \sqrt{p'_\mu\cdot\bar{\sigma}^\mu}\cdot\sqrt{p_\mu\cdot\bar{\sigma}^\mu} \tag{1.27}$$

$$2E_{pB} = \sqrt{p'_\mu\cdot\sigma^\mu}\cdot\sqrt{p_\mu\cdot\bar{\sigma}^\mu} + \sqrt{p'_\mu\cdot\bar{\sigma}^\mu}\cdot\sqrt{p_\mu\cdot\sigma^\mu} \tag{1.28}$$

$$\tau = \frac{Q^2}{4M_p^2} = \frac{\vec{q}_B^{\,2}}{4M_p^2} = \frac{E_{pB}^2 - M_p^2}{M_p^2} \tag{1.29}$$

gives the following simplified result for the time component:

$$\mathcal{J}^0 = 2\,i\,e\,M_p\,\chi'^{\dagger}\chi\,(F_1 - \tau\,\kappa\,F_2) = 2\,i\,e\,M_p\,\chi'^{\dagger}\chi\,G_E \tag{1.30}$$

The vector current $\vec{\mathcal{J}}$ can also be expressed in a similar way in this framework as:

$$\vec{\mathcal{J}} = -e\,\chi'^{\dagger}\,(\vec{\sigma}\times\vec{q}_B)\,\chi\,(F_1+\kappa\,F_2) = -e\,\chi'^{\dagger}\,(\vec{\sigma}\times\vec{q}_B)\,\chi\,G_M\,. \tag{1.31}$$

These results enable a simple interpretation of the Sachs form factors in the Breit reference frame. Specifically, the information on the electric charge and magnetic current distributions are contained in G_E and G_M, respectively. The electric and magnetic form factors can be associated with the Fourier transforms of the charge and magnetic current densities in this framework, in the non-relativistic limit. Expanding the Fourier transforms of these form factors in powers of q^2 gives the expressions:

$$G_{E,M}(Q^2) = \int \rho(\vec{r})_{E,M}\,e^{i\,\vec{q}\,.\,\vec{r}}\,d^3r = \int \rho(\vec{r})_{E,M}\,d^3r - \frac{\vec{q}^{\,2}}{6}\int \rho(\vec{r})_{E,M}\,\vec{r}^{\,2}\,d^3r + ... \tag{1.32}$$

The first term in this expansion gives the total electric or magnetic charge; the second term provides the corresponding root-mean-squared radii of the respective nucleon [4]. However, this simplified interpretation is complicated by a Lorentz contraction of the nucleon in the direction of motion. This contraction leads to non-spherical charge density distributions that complicate the Fourier transform interpretation of these form factors.

1.3 Measurement Techniques

There are several measurement techniques that are usually used to investigate the nuclear structure associated with elastic electron-proton scattering. The fundamental concepts of the Rosenbluth, the Polarization Transfer, Single Beam Asymmetries, and the Double Spin Asymmetries (DSA) techniques are discussed in this section.

1.3.1 The Rosenbluth Technique

The Rosenbluth method was the only technique used to obtain separated values for $G_E^{p,n}$ and $G_M^{p,n}$ until the 1990s [3]. To understand the principle associated with this separation technique requires an understanding of the electron-proton elastic scattering cross-section. The differential of the cross-section σ with respect to the solid angle[8] Ω is expressed in the following way:

$$\frac{d\sigma}{d\Omega} = \frac{\langle|\mathcal{M}|^2\rangle}{64\,\pi^2}\left(\frac{E'}{E}\right)\frac{1}{M_p} \tag{1.33}$$

where $\mathcal{M}$ is the scattering amplitude.

The formula for the differential cross-section for electrons scattering off nucleons for the single-photon exchange case is given by:

$$\frac{d\sigma}{d\Omega} = \left(\frac{d\sigma}{d\Omega}\right)_{Mott}\frac{E'}{E}\left[F_1^2(Q^2) + 2\,\left[F_1(Q^2) + F_2(Q^2)\right]^2\tan^2\frac{\theta}{2}\right] \tag{1.34}$$

where $(d\sigma/d\Omega)_{Mott}$ is the Mott cross-section[9], which is expressed as:

$$\left(\frac{d\sigma}{d\Omega}\right)_{Mott} = \left(\frac{\alpha}{2E}\right)^2\left(\frac{\cos^2\frac{\theta}{2}}{\sin^4\frac{\theta}{2}}\right). \tag{1.35}$$

Substituting the Sachs form factors from (1.17) and (1.18) into (1.34) gives the well known Rosenbluth formula:

$$\frac{d\sigma}{d\Omega} = \frac{\alpha^2}{Q^2}\left(\frac{E'}{E}\right)^2\left[2\,\tau\,G_M^2 + \frac{\cot^2\frac{\theta}{2}}{1+\tau}\left[G_E^2 + \tau\,G_M^2\right]\right] \tag{1.36}$$

A simple separation of the form factors is possible in this representation because there are no interference multiplicative terms.

[8] The solid angle Ω is a two-dimensional angle in three-dimensional space that an object subtends at a point. It is a measure of how large the object appears to an observer looking from that point.

[9] The Mott cross-section applies to the case of electrons scattering off spin-1/2 point-like particles.

The Rosenbluth cross-section has contributions from both the electric G_E and magnetic G_M terms. Consequently, a reduced cross-section can be defined as:

$$\sigma_{red} = (1+\tau)\,\frac{\epsilon}{\tau}\,\frac{d\sigma/d\Omega}{(d\sigma/d\Omega)_{Mott}} = G_M^2 + \frac{\epsilon}{\tau}\,G_E^2 \tag{1.37}$$

where the virtual photon polarization ϵ is given by $\epsilon = [1+2\,(1+\tau)\tan^2(\theta/2)]^{-1}$. The reduced cross-section isolates the contribution of the internal structure represented by the Sachs form factors. At a fixed Q^2, ϵ can be varied by changing the incident electron beam energy and the scattering angle. Consequently, one can measure the elastic scattering cross-section and separate the two form factors using a linear fit to the cross-section data. The slope and intercept of the fit respectively equal G_E^2/τ and G_M^2 providing a separation of the two factors. This method has been extensively used over the past 40 years to measure the elastic form factors. Although the Rosenbluth separation technique was, and still is, a successful method it has some practical limitations. A main disadvantage is the need to make a cross-section measurement. Such absolute measurements suffer systematic errors associated with inconsistent acceptance, luminosity, and detector efficiency between kinematic settings as well as requiring absolute normalization. The precision of this technique is also limited by cross-section measurements that require a broad range of kinematic settings in order to cover the required range of ϵ. Furthermore, to use such data in the same form factor extraction process requires that all of these systematics be well understood. In addition, the scaling of the contributions implies a low sensitivity for G_E and G_M for high and low Q^2, respectively.

1.3.2 Polarization Transfer Measurements

Over the past fifteen years, more form factor measurements have relied upon polarization measurement techniques. The polarization transfer process occurs when polarized electrons scatter elastically from protons. This transfer can be measured using the Recoil Polarization method (RPM) [32, 33, 34], which has been used in recent measurements to extract the proton form factor ratio [18, 20, 21, 22, 23]. In addition, Polarized Beam - Polarized Target Asymmetry measurements provide another way to extract this ratio, and will be discussed in Section 1.3.3. These alternative methods are based upon spin degrees of freedom and are focused on interference

terms of the form $G_E\,G_M$. Compared to cross-section experiments, the polarization spin-dependent experiments involve the measurement of polarization or helicity asymmetries. These quantities are independent of the cross-section normalization. Furthermore, most of the systematic uncertainties usually cancel when measuring a ratio of the polarization observables.

In particular, Akheizer and Rekalo's RPM measurements [34] suggested that the interference term $G_E\,G_M$ could be determined by measuring the transverse components of the recoil proton polarization. Instead of directly measuring the individual proton form factors, the G_E/G_M ratio can be obtained by measuring the recoil proton's transverse P_t and longitudinal P_l polarization components [3]:

$$\frac{G_E}{G_M} = -\frac{P_t}{P_l}\,\frac{E+E'}{2M_p}\,\tan\frac{\theta}{2} \tag{1.38}$$

where P_t and P_l are given by:

$$\sigma_{red}\,P_t \;=\; -2\,\sqrt{\tau\,(1+\tau)}\,\tan\left(\frac{\theta}{2}\right)\,G_E\,G_M \tag{1.39}$$

$$\sigma_{red}\,P_l \;=\; \frac{E+E'}{M_P}\,\sqrt{\tau\,(1+\tau)}\,\tan^2\left(\frac{\theta}{2}\right)\,G_M^2 \tag{1.40}$$

and σ_{red} represents the reduced cross-section. By taking the ratio of P_l and P_t the extracted ratio becomes [3]:

$$\mu_p\,\frac{G_E^p}{G_M^p} = -\mu_p\,\frac{E+E'}{2M_p}\,\tan\left(\frac{\theta}{2}\right)\,\frac{P_t}{P_l} \tag{1.41}$$

It is easy to see that this method offers several experimental advantages compared to making cross-section measurements. In particular,

- The systematic errors associated with changes in the settings of the spectrometer and beam energy are greatly reduced since only a single measurement is required at each Q^2.

- Polarization ratio measurements are not sensitive to such factors as the detector efficiency, beam polarization, and the analyzing power of the polarimeter.

- In addition, the electric form factor is more accurately characterized by making measurements of the interference term $G_E\,G_M$.

- Finally, the associated systematic uncertainties are usually much smaller because a measurement of the absolute cross-section is not required.

1.3.3 Double Spin Asymmetry Measurements

Although the recoil polarization method can in principle extract the form factor ratio at any Q^2, doing so requires a measurement of the recoil proton polarization. The proton does not acquire enough energy to reach the polarimeter at low Q^2 due to the low energy transfer, which prevents its exit from the target material [35]. An alternative method based on spin degrees of freedom is the Double Spin Asymmetry (DSA) technique. The second part of Experiment E08-007 was designed to measure the proton form factor ratio using this technique. Double polarization experiments such as this measure the asymmetry in the scattering of longitudinally polarized electrons by polarized protons or neutrons. The form factor ratio can be obtained from the beam helicity asymmetry by keeping the electron and nucleon detection angles constant while alternating the helicity of the electron beam.

Following the prescription of Donnelly and Raskin [36], the inclusive electron-proton cross-section can be expressed as a sum of an unpolarized cross-section[10], Σ, and the polarized spin-dependent cross-section[11], Δ. The differential cross-section for longitudinally polarized electrons scattering from a polarized proton target can be written as:

$$\sigma(h) = \Sigma + h\Delta\,, \tag{1.42}$$

where the helicity of the electron h is defined as the projection of the electron spin along its momentum direction, which can be either positive or negative for longitudinally polarized electron beams, i.e., $h = \pm 1$.

Donnely and Raskin showed that the spin-dependent Δ and unpolarized Σ cross-section ratio could be represented by the expression:

$$\frac{\Delta}{\Sigma} = -f_1 \frac{a\,F_T^2 + b\,F_L\,F_T}{F^2} \tag{1.43}$$

with the following definitions taken from [36] (in the ultra-relativistic approximation)[12]:

$$f_1 = \frac{1}{\sqrt{2}} \tag{1.44}$$

[10]The unpolarized cross-section is given in (1.36), i.e, $\Sigma = \frac{d\sigma}{d\Omega}$.

[11]The polarized spin-dependent cross-section component is different from zero when the beam is longitudinally polarized.

[12]When comparing with the original work by Donnely and Raskin, note that the definition of Q^2 uses opposite sign relative to the notations in this report.

$$v_L = \left(\frac{Q^2}{q^2}\right)^2 \tag{1.45}$$

$$v_T = -\frac{1}{2}\left(\frac{-Q^2}{q^2}\right) + \tan^2\frac{\theta}{2} \tag{1.46}$$

$$v_{TL} = \frac{1}{\sqrt{2}}\left(\frac{-Q^2}{q^2}\right)\sqrt{\frac{Q^2}{q^2} + \tan^2\frac{\theta}{2}} \tag{1.47}$$

$$v_{T'} = \sqrt{\frac{Q^2}{q^2} + \tan^2\frac{\theta}{2}}\tan\frac{\theta}{2} \tag{1.48}$$

$$v_{TL'} = \frac{1}{\sqrt{2}}\left(\frac{-Q^2}{q^2}\right)\tan\frac{\theta}{2} \tag{1.49}$$

$$F_L = \frac{1+\tau}{\sqrt{4\pi}}G_E \tag{1.50}$$

$$F_T = \frac{-\sqrt{2\tau(1+\tau)}}{\sqrt{4\pi}}G_M \tag{1.51}$$

$$F^2 = v_L F_L^2 + v_T F_T^2 \tag{1.52}$$

$$a = \sqrt{2}v_{T'}\cos\theta^* \tag{1.53}$$

$$b = 2\sqrt{2}v_{TL'}\sin\theta^*\cos\phi^* \tag{1.54}$$

It should be noted that both the scattering angle θ of the electron in the lab frame and the spherical coordinates (θ^*, ϕ^*)[13] of the polarization axis relative to the scattering plane are required in these relationships.

The asymmetry between the cross-sections of the different helicities states is represented by (1.43). As a result, this asymmetry can be expressed as:

$$A = \frac{\sigma_+ - \sigma_-}{\sigma_+ + \sigma_-} = \frac{\Delta}{\Sigma} \tag{1.55}$$

[13]The spherical coordinates (θ^*, ϕ^*) of the polarization axis relative to the scattering plane in the direction of the recoil momentum are illustrated in Figure 3.8 of Section 3.1.1.

where $\sigma_{\pm}$ delineates the different cross-sections associated with the two helicity states of the polarized electron beam.

The experimental asymmetry A_{raw} is related to the spin-dependent physical asymmetry by the relationship:

$$A_{raw} = P_b\, P_t\, f\, A_{phys} \tag{1.56}$$

where P_b and P_t are the respective beam and target polarization values. Here, the dilution factor f is used to account for the reduction in the amount of hydrogen seen by the beam due to the fact that the NH_3 target (used to make the polarized proton target) also contains nitrogen atoms.

In terms of the Donnely and Raskin notation, the asymmetry given by (1.55) can be rewritten as:

$$A_{phys} = f_1 \frac{a\, F_T^2 + b\, F_L\, F_T}{F^2} \;=\; f_1\, \frac{a\, F_T^2 + b\, F_L\, F_T}{v_L\, F_L^2 + v_T\, F_T^2}\,. \tag{1.57}$$

Furthermore, dividing this expression by F_T^2 gives it the following form:

$$A_{phys} = f_1\, \frac{a + b\, \left[\frac{F_L}{F_T}\right]}{v_T + v_L\, \left[\frac{F_L}{F_T}\right]^2} \tag{1.58}$$

Therefore, the beam-target asymmetry can be defined using (1.55), (1.56), and (1.58) to give the following result:

$$A_{phys} \;=\; \frac{1}{P_b\, P_t\, f}\, \frac{\sigma_+ - \sigma_-}{\sigma_+ + \sigma_-} \;=\; \frac{1}{P_b\, P_t\, f}\, \frac{\Delta}{\Sigma} \;=\; \frac{1}{P_b\, P_t\, f}\;\; f_1\, \frac{a + b\, \left[\frac{F_L}{F_T}\right]}{v_T + v_L\, \left[\frac{F_L}{F_T}\right]^2}\,. \tag{1.59}$$

Substituting the Donnely and Raskin definitions defined in (1.44) through (1.54) into this equation gives the following well known result:

$$\begin{aligned} A_{phys} \;=\; & \frac{1}{P_b\, P_t\, f}\, \left[2\, \sqrt{\frac{\tau}{1+\tau}}\, \tan\left(\frac{\theta}{2}\right)\right] \;\times \\ & \frac{\left[\sqrt{\tau\, (1 + (1+\tau)\, \tan^2\left(\frac{\theta}{2}\right)}\, \cos\left(\theta^*\right)\, G_M^2 + \sin\left(\theta^*\right)\, \cos\left(\phi^*\right)\, G_M\, G_E\right]}{\left[\frac{G_E^2 + G_M^2}{1+\tau} + 2\, \tau\, G_M^2\, \tan^2\left(\frac{\theta}{2}\right)\right]}\,. \end{aligned} \tag{1.60}$$

This expression is a function of the form factor ratio G_E/G_M[14], which the DSA technique exploits. This technique extracts the proton elastic form factor ratio using

[14]This explicit dependence on the form factor ratio can be seen by dividing the numerator and denominator by the factor G_M^2.

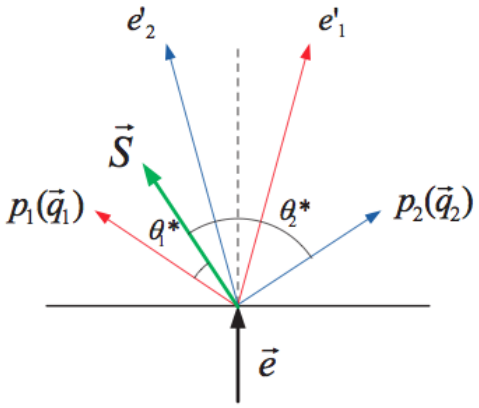

Figure 1.4: The kinematics for the two simultaneous measurements where the scattered electrons e_1 and e_2 are detected in right and left high resolution spectrometer (HRS), respectively. The recoil protons p_1 and p_2 point in the direction of the transferred momenta $\vec{q_1}$ and $\vec{q_2}$, respectively. $\vec{S}$ denotes the target spin direction where θ_1^* and θ_2^* represent the angles with respect to $\vec{q_1}$ and $\vec{q_2}$ in the coordinate frame illustrated in Figure 3.8 [27].

only measurements of scattered electrons negating the need to detect the recoil proton. As a result, this technique is able to measure the form factor ratio in much lower Q^2 regions than previously attained.

Experiment E08-007 conducted DSA measurements using two high resolution spectrometers configured to have equal scattering angles on either side of the beam and measuring the same Q^2. Measuring the asymmetries simultaneously in two spectrometers with different angles between the momentum transfer and the target spin axis can be used to extract the form factor ratio. The kinematics associated with these simultaneous measurements are illustrated in Figure 1.4. Taking the ratio of the two asymmetries defined by (1.60) can be used to derive an expression for the ratio of G_E/G_M [37]. Doing so, gives the following result for the proton form factor ratio:

$$\mu_P \frac{G_E^P}{G_M^P} = -\mu_P \frac{a(\tau_1,\theta_1)\,\cos(\theta_1^*) - \frac{f_2}{f_1}\,\Lambda\, a(\tau_2,\theta_2)\,\cos(\theta_2^*)}{\cos(\phi_1^*)\,\sin(\theta_1^*) - \frac{f_2}{f_1}\,\Lambda\,\cos(\phi_2^*)\,\sin(\theta_2^*)} \tag{1.61}$$

where $a(\tau_n,\theta_n) = \sqrt{\tau_n\,(1+(1+\tau_n)\,tan^2\,(\theta_n/2))}$ has subscripts that correspond to the respective HRS arms as defined in Figure 1.4. The angles θ_i^* and ϕ_i^* correspond to the polar and azmuthal angles of the respective target spin axis associated with each spectrometer in the scattering plane coordinate frame shown later in Figure 3.8. The

ratio of the two asymmetry measurements is represented by $\Lambda = A_1/A_2$; however, the values of target and beam polarizations, P_t and P_b, cancel when forming this ratio and therefore do not appear in the final expression [27]. This eliminates one of the larger systematic uncertainties of a single-beam target asymmetry measurement [37]. Furthermore, it is noted that the two spectrometers are essentially identical at least to first order; therefore, the dilution factors associated with each arm are approximately the same, i.e., $f_1 \approx f_2$ [27]. It is however conceivable that small differences in the two spectrometers could result in slightly different dilution factors; as a result, their ratio has been retained in the final expression[15] [37].

1.3.4 Single Arm Asymmetry Measurements

Another technique for calculating the form factor ratio from asymmetry measurements is possible using (1.60), which is quadratic in terms of the ratio of the form factors. This calculation requires a physical asymmetry measurement obtained from a single arm of the spectrometer rather than two raw asymmetries used by the DSA technique. Therefore, the single arm calculation can be used to generate an estimate of the form factor ratio albeit with greater uncertainties. The results can be compared to those obtained using the DSA method. Solving (1.60) for the ratio of the form factors gives:

$$\frac{G_E}{G_M} = -\frac{b}{2A_{phys}}\,\sin(\theta^*)\,\cos(\phi^*) + \sqrt{\frac{b^2}{4A_{phys}^2}\sin^2(\theta^*)\,\cos^2(\phi^*) - \frac{a}{A_{phys}}\,\cos(\theta^*) - c} \tag{1.62}$$

where A_{phys} is the physical asymmetry obtained from a single set of spectrometer measurements that accounts for beam and target polarization, and the dilution factor. The form factor ratio is obtained by multiplying (1.62) by μ_p. The coefficients a, b, and c are kinematic factors defined in terms of τ, and θ and are given by:

$$\begin{aligned} a &= 2\,\tau\,\tan\left(\frac{\theta}{2}\right)\sqrt{1+\tau+(1+\tau)^2\,\tan^2\left(\frac{\theta}{2}\right)} \\ b &= 2\,\tan\left(\frac{\theta}{2}\right)\,\sqrt{\tau\,(1+\tau)} \\ c &= \tau + 2\,\tau\,(1+\tau)\,\tan^2\left(\frac{\theta}{2}\right) \end{aligned}$$

[15] The factor μ_p has been included in the final result to normalize (1.61) to unity.

1.4 Motivation for Form Factor Ratio Measurements at Low Q^2

Previous studies have focused on the high Q^2 proton elastic form factors, while more recent studies have focused on the low Q^2 region primarily for the following reasons. Firstly, the electromagnetic form factors are fundamental properties of the nucleon that require a greater degree of understanding that can only be obtained by performing more accurate experimental measurements. Secondly, theory generally indicates that the proton elastic form factors are smooth functions of Q^2; however, current theoretical results and measurements suggest that the form factors may exhibit structure. Experiment E08-007 was designed to expose such structures in the form factors (or the form factor ratio).

In the high Q^2 regime, it is now generally accepted that the proton form factor ratio decreases smoothly as Q^2 increases. As previously discussed, for $Q^2 < 1$ GeV^2 the existing world data appear to be less conclusive. Analysis performed by Friedrich and Walcher [25] found deviations in the nucleon form factor fits that indicated the existence of structure at low Q^2. This has been interpreted as evidence of the virtual pion cloud surrounding the nucleon [27]. It is possible to fit all four nucleon form factors if one employs phenomenological fits [24, 25] and fits based upon the constituent quark model. These results each show evidence of the virtual pion cloud. The previous examinations of the pion cloud contributions have mainly looked at the structure relative to the dipole form factor (except G_E^n) [27]. Whereas, experiment E08-007 measurements were designed to allow for a precise model-independent comparison of the behaviour of G_M^p and G_E^p that does not depend on the dipole form factor being appropriate at low Q^2.

All of the high precision world data for the form factor ratio at low Q^2 obtained from polarization measurements, fits, and models are presented in Figure 1.5. This region has been a subject of increased interest in recent years due to high precision measurements of the proton radius by muonic hydrogen lamb shift measurements [38]. These measurements show a 7σ deviation of the proton charge radius relative to the values extracted by electron scattering and Lamb shift measurements as shown in Figure 1.6. However, there is a possibility that the source of the discrepancy with

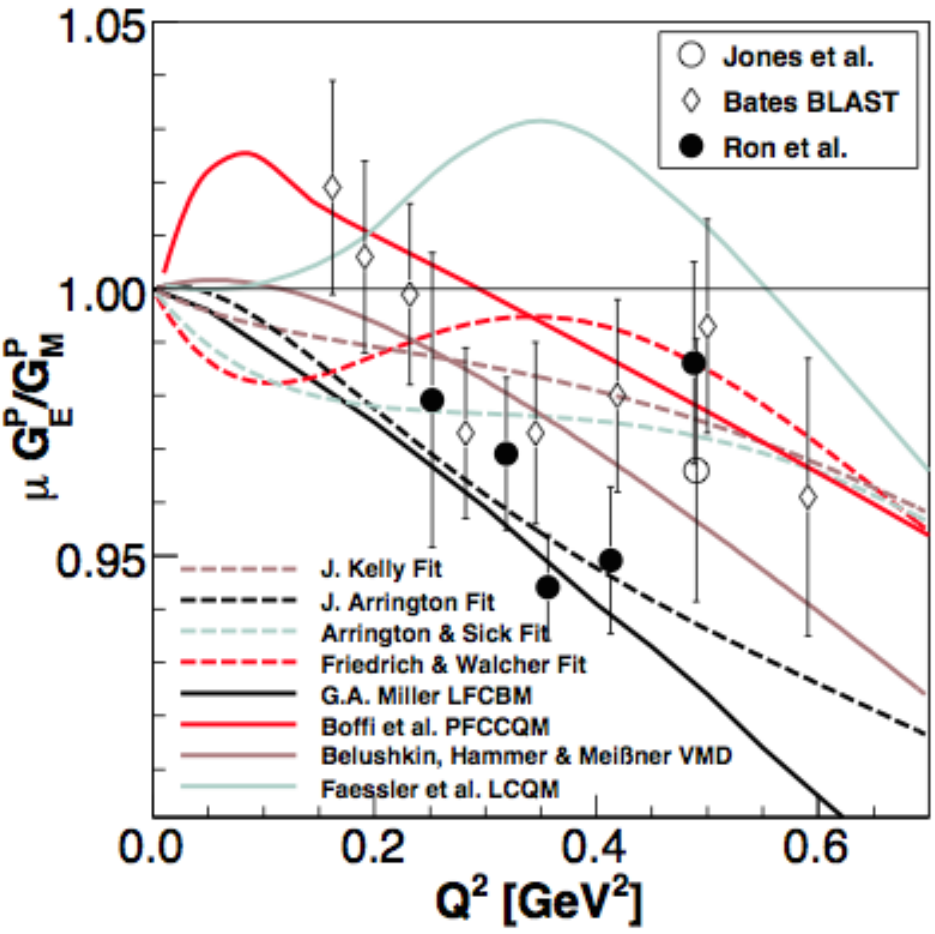

Figure 1.5: High precision results of the proton form factor ratio having a total uncertainty of $\sigma_{tot} < 3\%$ compared to several fits and parameterizations [27].

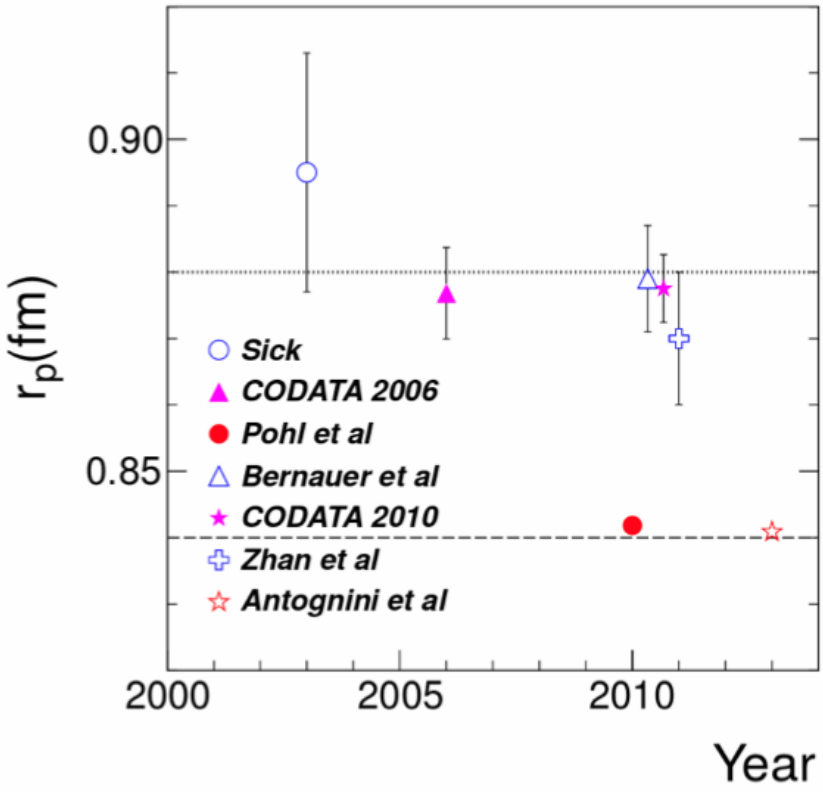

Figure 1.6: A summary of some recent proton charge radius determinations: Sick [39], CODATA 2006 [40], Bernauer *el al.* [41], CODATA 2010 [42], and Zhan *el al.* [28] represent results associated with electron-proton scattering experiments. Experiments by Pohl *el al.* [43] and Antognini *el al.* [44] used muonic hydrogen lamb shift.

the radii arises from the way that the fits are performed in the low Q^2 region. Since the proton RMS radius[16] is defined by the slope of the form factor as Q^2 tends to zero, precise knowledge of the functional behaviour at low Q^2 is required in order to make reliable comparisons between the scattering and Lamb shift data.

The form factor ratio was measured to about 2% and found to be consistent with unity in the Bates BLAST experiment[17] [2] while JLAB's LEDEX experiment [26] had uncertainties of approximately 1% over a similar Q^2 region[18]. Both of these experiments showed that the ratio clearly drops below unity in the region of Q^2

[16]The proton RMS radius is defined by the slope of the form factor as Q^2 tends to zero using an approximation of (1.32) for $qR \ll 1$.

[17]In the BLAST experiment, longitudinally polarized electrons were elastically scattered from a polarized hydrogen internal gas target in the region of $0.15 \leq Q^2 \leq 0.65$ GeV.

[18]The LEDEX experiment used the polarization transfer technique with a hydrogen target to perform its measurements in the region of $0.2 \leq Q^2 \leq 0.5$ GeV^2.

equal to 0.30 GeV^2 with the implication that the form factor ratio has some form of structure in the region of low Q^2.

In Figure 1.5, the three solid lines represent different quark model calculations. Both the Boffi *el al.* [45] and Faessler *et al.* [47] calculations show structures in the ratio although they tend to be higher than the data [27]. Nevertheless, they suggest that narrow structures might be theoretically possible. From the fits and data shown, one can conclude that the ratio is only known to within about $\pm 2\%$ over the low Q^2 range. Note that the fit by Friedrich and Walcher crosses over the data near $Q^2 = 0.25$ GeV^2. This indicates that the structures are not actually present but represent artifacts of the fitting process [27].

A series of polarization transfer measurements were conducted at the MIT-Bates facility [2, 16, 17], the MAMI facility [18, 19], and at Jefferson Lab [20, 21, 22, 23, 26, 48, 49]. Figure 1.7 shows the results obtained by these experiments relative to the Rosenbluth separation results [35]. Unlike the Rosenbluth results, a clear decline in the ratio as Q^2 increases is evident for the polarization data. This discrepancy has been the focus of much theoretical and experimental work. It is today considered most probable that the OPE approximation is not valid in this region of Q^2 and that the two-photon-exchange (TPE) corrections are in fact required at higher Q^2 [7]. The bottom plot of Figure 1.7 shows a re-analysis of the Rosenbluth results illustrated in the top plot with TPE corrections.

The aim of Experiment E08-007 was to provide a high precision survey of the proton form factor ratio in the low Q^2 regime. As a result, the hope was to confirm the existence of any deviation of the proton form factor ratio from unity and to expose any local structure in this low momentum transfer region.

1.5 Models and Global Fits

Significant theoretical progress has been made in recent years in understanding the nucleon electromagnetic structure from the underlying theory of QCD. Ideally, one should be able to calculate the nucleon electromagnetic form factors directly in the pQCD regime to confront the data[19]. Unfortunately, it is not possible to solve QCD

[19]This has been extremely well tested in the high energy region, i.e., in the perturbative QCD (pQCD) regime.

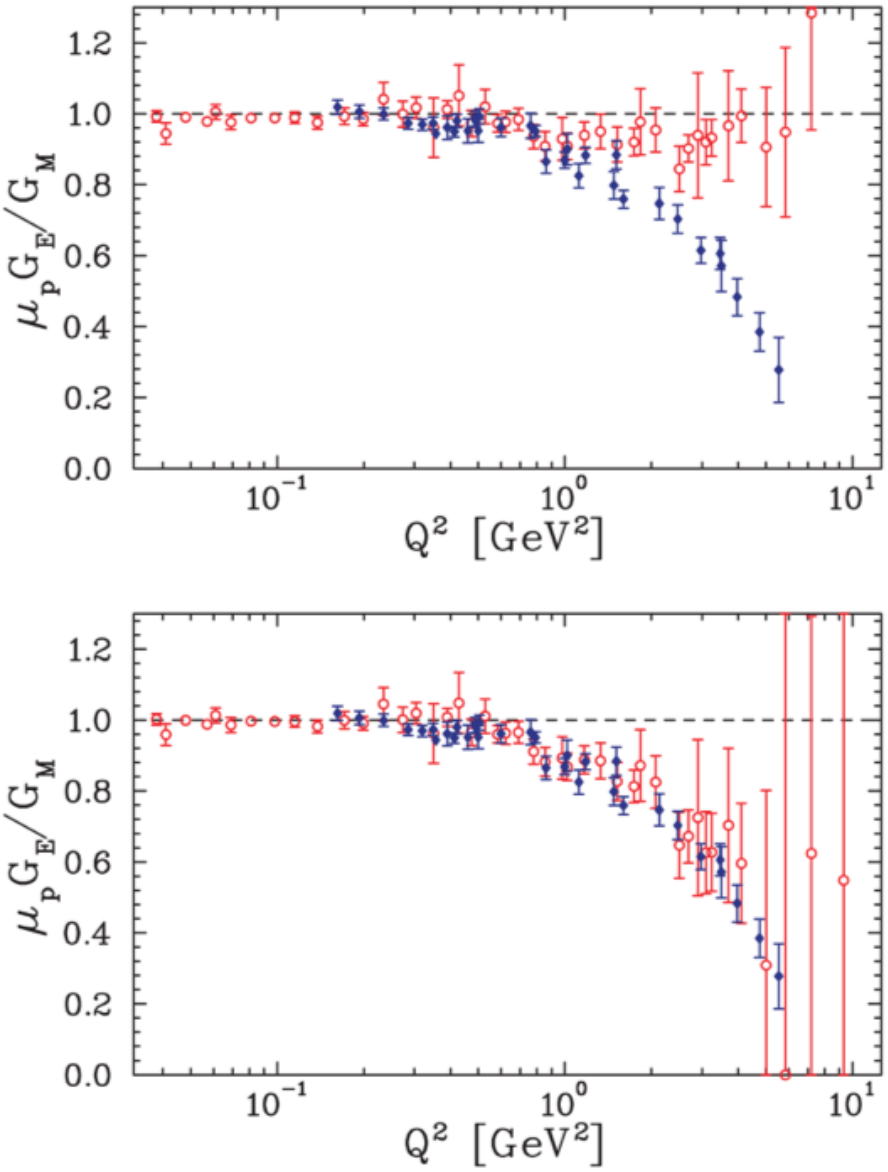

Figure 1.7: Ratio $\mu_p G_E^p/G_M^p$ extracted from the polarization transfer (filled blue diamonds) and Rosenbluth method (open red circles). The top/bottom figures show Rosenbluth method data without/with TPE corrections applied to the cross-section data. These figures were obtained from reference [35].

analytically in the confinement regime where the available world experimental data are located. Several QCD-inspired models, phenomenological models, and empirical fits have been suggested to provide predictions of the form factor behaviour in this Q^2 region [35], the details associated with these efforts are provided in References [50, 51, 52]. The following sections provide brief discussions on various models and fits used to calculate nucleon electromagnetic form factors.

Vector Meson Dominance

The vector meson dominance model (VDM) was developed before the introduction of QCD to describe the interactions between energetic photons and hadronic matter. The model was hypothesized to explain the electromagnetic interactions with hadrons through coupling with intermediate vector mesons [53]. In this model, a virtual photon will transform into a lower lying vector mesons, such as $\rho(770)$, $\omega(782)$, and $\phi(1020)$, which have the same quantum numbers as the photon, before interacting with the target hadron. The motivation for such a model is through the process $e^- e^+ \rightarrow$ hadrons, where mesons show up as prominent resonances. The contributions due to these resonances to the space-like diagram of an $e\,N$ scattering process can then be evaluated and predictions can be made.

In these models, the strength of the coupling coefficients are left as free parameters that are fit to existing form factor data [53]. Early VMD fits were developed by Iachello *et al* [54]. These fits were later improved by Gari and Krümpelmanm [55] who included pQCD effects at higher Q^2, and more recently, this model has been extended to include more mesons in a fit by Lomon [56]. A phenomenological addition including the quark structure of the hadron was added by Bijker and Iachello [57]. Such models have had great success in fitting measured data, but less so in regards to making predictions [58].

Constituent Quarks Models

Constituent quark models (CQMs) assume that the structure of nucleons are comprised of three valence quarks. In these models, the quarks are taken to have masses of about $m_N/3 \approx 300$ MeV and are placed in a confining potential. The ground state of such a system is then taken to describe the nucleon. Relativistic effects are taken

into account such that these models can be used to describe scattering at Q^2 on the order of the constituent quark masses. These models have had general success in the description of the form factors at higher Q^2, but the lower Q^2 data includes additional degrees of freedom, such as in the form of the pion cloud or local structure of the constituent quarks [53].

Recently, calculations by Miller were performed using light front dynamics and a model called the Light Front Cloudy Bag Model (LFCBM) [59]. In this model, the addition of a pion cloud allows for a virtual photon to interact with these pions, as well as the constituent quarks. This model has had success in describing all of the electromagnetic form factors with the exception of G_M^n at low Q^2.

Fits

The nucleon electromagnetic form factors are needed for various calculations in nuclear physics such as the proton radius. As a result, a simple parameterization that accurately and reasonably represents the data over a wide range of Q^2 particularly for both $Q^2 \to 0$ and $Q^2 \to \infty$ would be of convenience. For reasonable behaviour at low Q^2, the power-series representation should involve only even powers of Q. At high Q^2, dimensional scaling rules require $G_{E,M} \propto Q^{-4}$. However, at present the most common parameterizations violate one or both of these conditions. Recently, Kelly proposed a much simpler parametrization that takes the form [60]:

$$G_{E,M}\left(Q^2\right) \propto \frac{\Sigma_{k=0}^{n} a_k \, \tau^k}{1 + \Sigma_{k=1}^{n+2} b_k \, \tau^k}. \tag{1.63}$$

Both the numerator and denominator are polynomials in terms of $\tau = Q^2/4\,m_p^2$ that have orders dependent upon the parameter n and whose coefficients are a_k and b_k, respectively. Note that the degree of the denominator is chosen larger than that of the numerator to ensure the $G_{E,M} \propto Q^{-4}$ for large Q^2. Figure 1.8 shows good agreement with data using only four parameters for G_E^p, G_M^p, and G_M^p, and only two for G_E^n.

Arrington and Sick [61] performed a fit of the world data at low momentum transfers by a continued fraction expansion [28]:

$$G_{E,M}(Q^2) = \frac{1}{1 + \frac{b_1 \, Q^2}{1 + \frac{b_2 \, Q^2}{1 + \ldots}}} \tag{1.64}$$

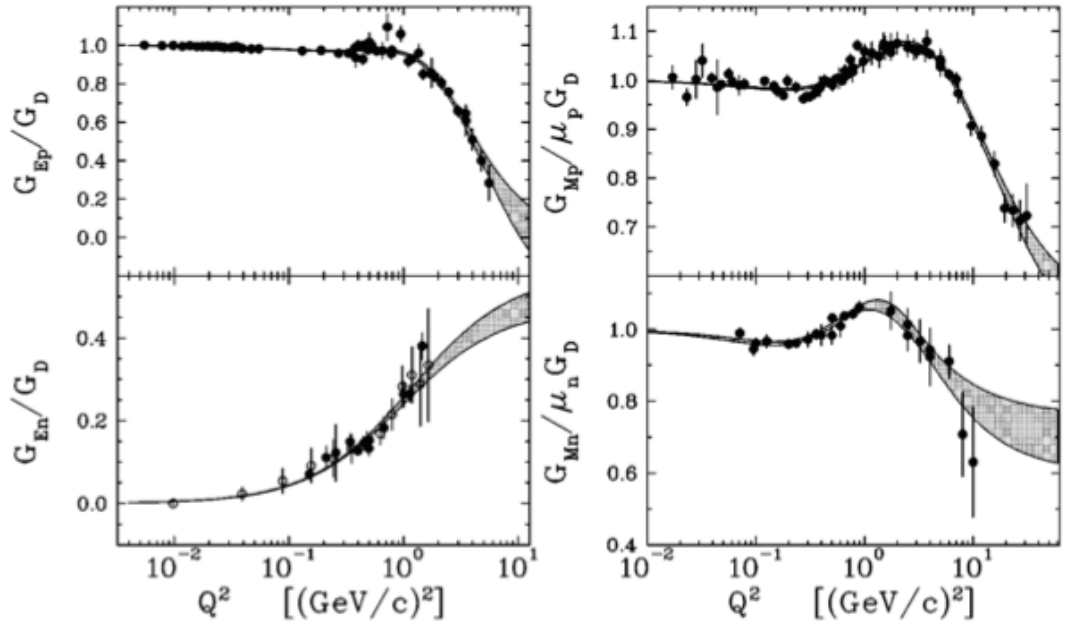

Figure 1.8: Fits to nucleon electromagnetic form factors. For G_E^n, data using recoil or target polarization [62] - [68] are shown as filled circles while data obtained from the deuteron quadrupole form factor [69] are shown as open circles. Figure obtained from reference [60].

in terms of the expansion coefficients b_i. This model was found to provide good fits for the low momentum transfer region extending upwards to $Q^2 = 0.64\,\mathrm{GeV}^2$. Their analysis included the effects of both Coulomb distortion and TPE. Later on, Arrington *et al.* [70] performed a global analysis of the world data that combined the corrected Rosenbluth cross-sections and polarized data to produce the first extraction of G_E and G_M that included an explicit TPE correction. Figure 1.9 shows this global analysis compared with the world data.

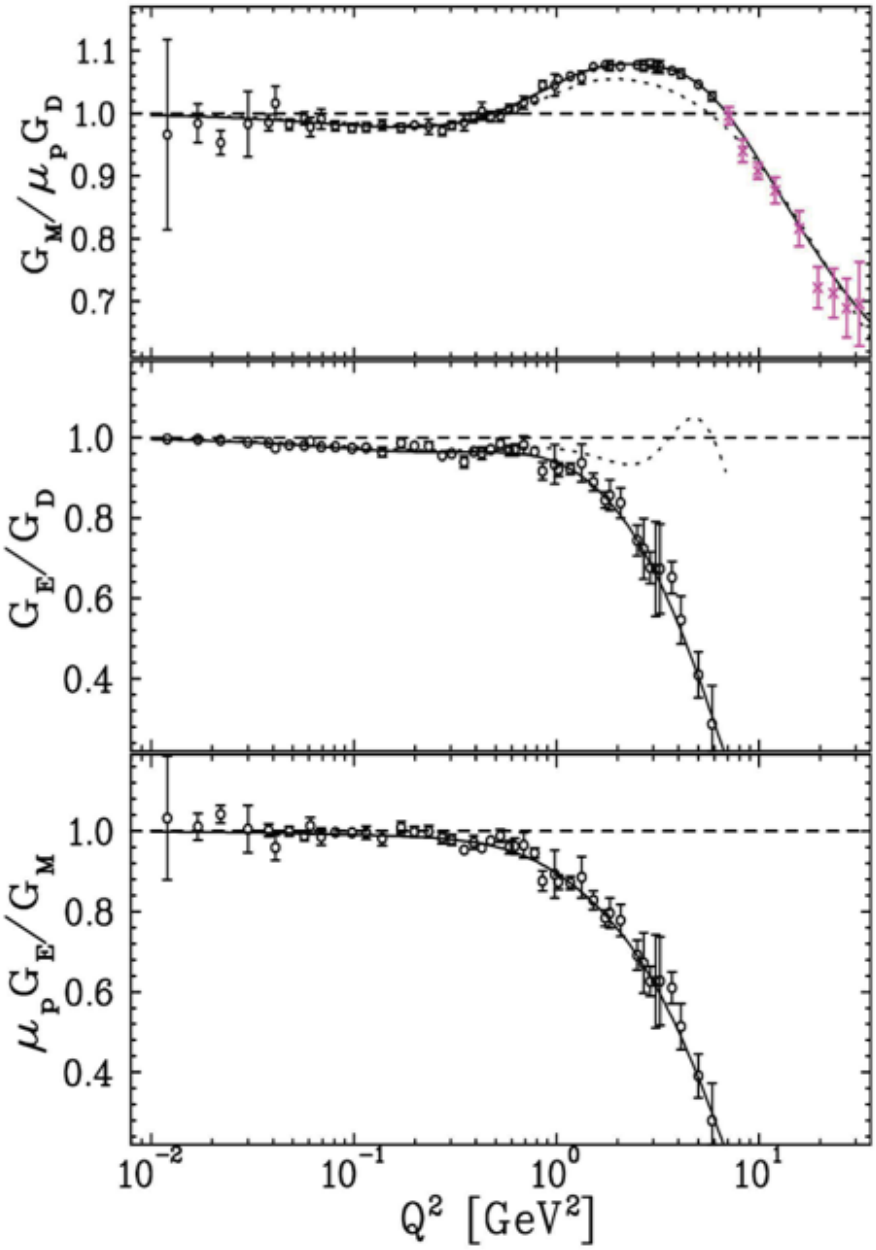

Figure 1.9: Extracted values of G_E and G_M from the global analysis. The open circles are the results of the combined analysis of the cross-section data and polarization measurements. The solid lines are the fits to TPE-corrected cross-section and polarization data. The dotted curves show the results of taking G_E and G_M from a fit to the TPE-uncorrected reduced cross-sections. Figure obtained from Reference [70].

Chapter 2

Experiment

This chapter provides a brief description of the experimental details associated with experiment E08-007 spin and double-spin asymmetry measurements. In particular, it provides a description of the experimental setup, the kinematics, the Continuous Electron Beam Accelerator Facility (CEBAF) [46], and some of the subsystems configured in Hall A for this experiment. In addition, particulars on the polarized target and the data acquisition system are also provided.

2.1 Experimental Setup

The experimental setup was designed to measure the proton elastic form factor ratio using spin and double-spin asymmetries over the kinematics range of $0.01 \leq Q^2 \leq 0.08$ GeV^2. An illustration of the experimental setup is provided in Figure 2.1 showing all of the major sub-systems and their placement in Hall A. With the exception of the chicane and septum magnets, itemized as sub-systems 7 and 10 in Figure 2.1, all of the sub-systems shown are standard instrumentation used in Hall A. A description of these components can be found in Reference [46].

In this setup, the polarized electron beam passes through a set of fast and slow rasters before entering the two chicane magnets designed to compensate for the effect of the magnetic field used to polarized NH_3 target. The scattered beam of electrons was then bent further by the two septum magnets in order to achieve the required scattering angles in line with the acceptance of two identical High Resolution Spectrometers (HRS) used for detecting scattering events.

2.2 Kinematics

This experiment used three different kinematic settings having beam energies of 1.1, 1.7, and 2.2 GeV. Furthermore, the left and right HRS were set up to symmetrically

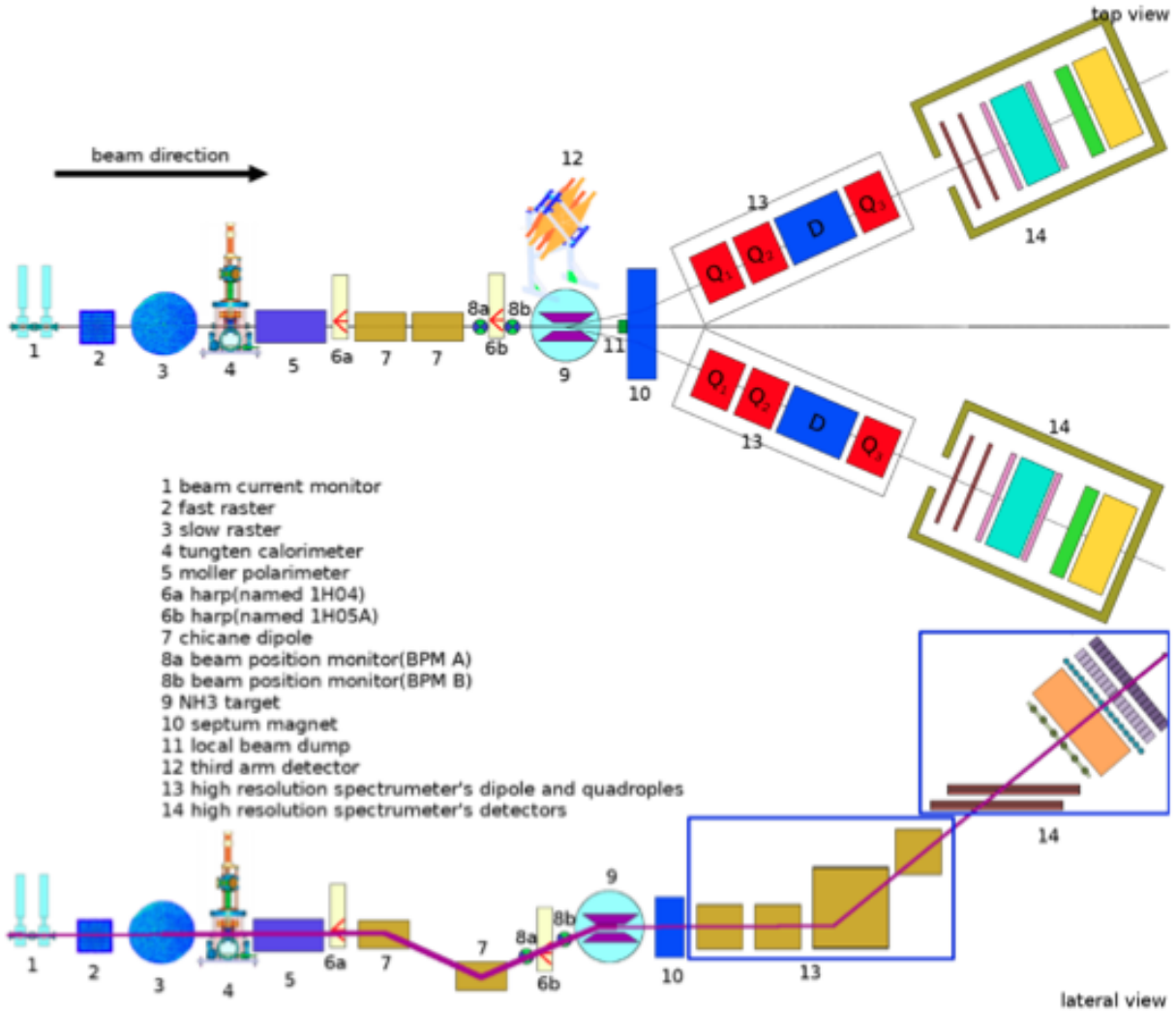

Figure 2.1: Schematic diagram of the E08-007 experimental setup [35]. The upper graphic displays a top-down view of the layout of both HRS arms while the lower graphic displays a lateral view of the same. These illustrations show the individual placement of the equipment along the beam line.

E (GeV)	ARM	θ (deg)	θ^* (deg)	ϕ^* (deg)	E' (GeV)	Q^2 (GeV^2)
2.253	left	6.0	85.5	0.0	2.224	0.054
1.712	left	6.0	87.2	0.0	1.695	0.032
1.157	left	7.5	87.3	0.0	1.145	0.023
2.253	right	6.0	74.3	0.0	2.224	0.054
1.712	right	6.0	76.0	0.0	1.695	0.032
1.157	right	7.5	76.1	0.0	1.145	0.023

Table 2.1: Central kinematics for the left and right HRS where θ is the scattering angle and the star angles are the angles associated with the polarization axis relative to the recoil direction. Note that when the target polarization field is flipped $\phi^*_{new} = 180^\circ$ and $\theta^*_{new} = 180^\circ - \theta^*$.

detect electrons on opposite sides of the beam-line. Specifically, they were configured in order to detect elastic scattering events at approximately 6° in line with these beam energies. The central kinematics are provided in Table 2.1 and correspond to scattering events that enter each HRS at their central point of acceptance. This table shows the initial beam energy E, the scattering angle θ, the central scattering plane variables θ^* and ϕ^*, the final beam energy E', and the corresponding central value of Q^2 for each kinematic setting listed in this table.

2.3 CEBAF

The high energy electron beam is produced by JLAB's CEBAF facility shown in Figure 2.2. This accelerator facility consists of four major components that include the injector site, two linear accelerators (linacs), and a series of recirculation arcs at each end of the accelerator. Its configuration is capable of redirecting the beam into one or more of the three experimental halls. Each of these components will now be discussed.

The injector system produces and injects a beam of electrons into the accelerator from either a thermionic or a polarized electron gun [46]. Experiment E08-007 made use of the facility's polarized electron gun to generate the beam by illuminating a strained GaAs cathode using a 1497 MHz gain-switched diode laser system operating at 780 nm. The degree of polarization obtained was measured at the injector using a 5 MeV Mott polarimeter while the orientation of the polarization vector was achieved using a Wien filter. As a result, the degree of polarization achieved for this experiment

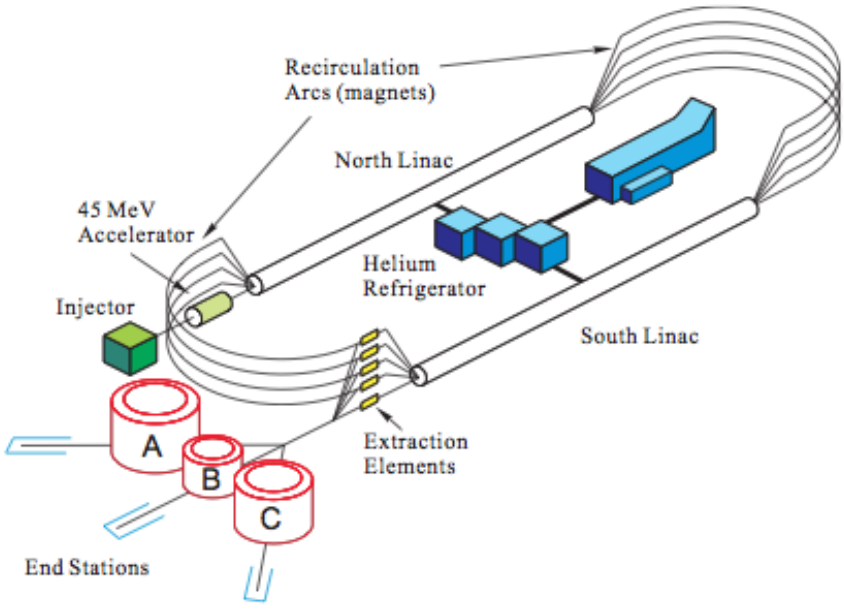

Figure 2.2: Schematic of the Jefferson Lab continuous electron beam accelerator facility (CEBAF). This system consists of two linacs that are connected by recirculation arcs (magnets) that are used to accelerate the electron beam to higher energies for experimental purposes.

was between 80% and 90%. The electron helicity was randomly generated using a right or left circularly polarized laser that was pseudo-randomly flipped at a rate of 960.015 Hz. Occasionally, a half-wave plate (HWP) was inserted into the injector to flip the helicity sign as an additional systematic check of the asymmetries obtained.

The beam current delivered to the three experimental halls can be controlled independently [46]. In Figure 2.2, the beam begins its first orbit when it enters the accelerator at the injector site into the first of two superconducting RF linacs that are connected by two 180° recirculation arcs constructed of magnets. Each linac consists of 20 cryo-modules. The beam is accelerated as it passes through each linac but travels through different bending magnets on each lap dependent upon its current energy. After the first full pass around the accelerator, the beam may then be split and directed to any of the experimental halls. The beam continues to recirculate and can achieve a total energy of about 6 GeV. A refrigeration plant provides liquid helium to remove the heat dissipated in the accelerator's components. As a side note, after this experiment CEBAF was upgraded, where the beam energy was increased to approximately 12 GeV by adding ten new high performance cryo-modules (five per

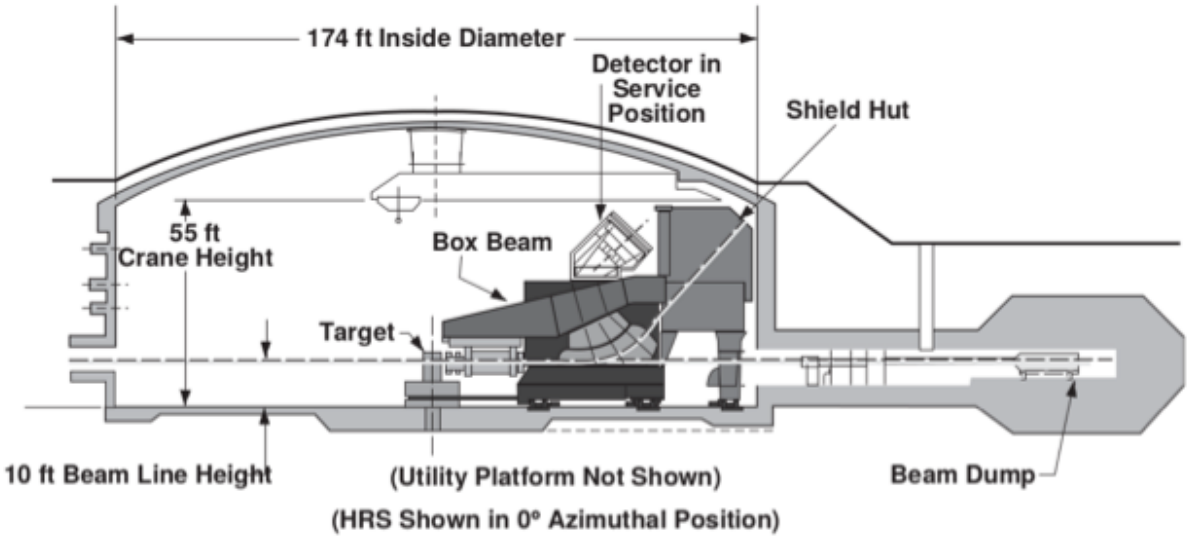

Figure 2.3: Schematic cross section of Hall A with one of the HRS spectrometers in the (fictitious) 0° position [46].

linac). In addition, a new experimental hall, Hall D, was constructed as part of this upgrade.

2.4 Experimental Hall A

Hall A is the largest experimental hall at CEBAF and its basic layout is provided in Figure 2.3. The central elements consist primarily of the target scattering chamber and the two HRS arms. These spectrometers are capable of making accurate measurements of momentum and angle at high luminosities. In the case of experiment E08-007, the presence of these spectrometers was crucial in obtaining measurements for determining the form factor ratio at a number of kinematic settings. A more detailed description of the equipment used in Hall A to support this experiment are discussed in the following sections.

2.4.1 Rasters

Fast and slow raster systems were used in E08-007 in order to decrease target damage, polarization loss, and to reduce the systematic uncertainties associated with the polarization measurements performed using Nuclear Magnetic Resonance (NMR). These uncertainties were due to the fact that the NMR coil was in contact only with the

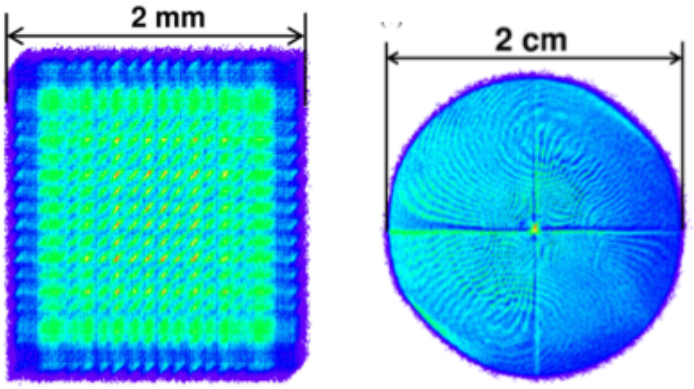

Figure 2.4: The fast and slow raster patterns are shown respectively in the left and right images. They illustrate the distribution of the beam over the surface of the target as indicated by the green and blue that respectively represent greater and lesser degrees of intensity in these images [35].

outer layer of the target [35]. Each raster was positioned 17 meters upstream of the target.

The fast raster was made up of two dipole magnets: one vertical and one horizontal. The beam position is moved with a time-varying magnetic field with a triangular waveform, allowing for a uniform intensity distribution of beam on the target [71]. The fast raster magnets used a common triangular waveform with a frequency of 25 kHz and resulted in a 2×2 mm^2 square. However, the slow raster system applied two 30 Hz sine functions with a relative phase of $\pi/2$ between the vertical and horizontal axes in order to obtain a circular pattern with a diameter of approximately 2 cm. The use of the slow raster system was necessary in order to evenly distribute the heating and ionizing effect on the target. The increase in the target temperature was minimized by linearly scanning the beam [71]. Both raster patterns are respectively shown in Figure 2.4.

2.4.2 Møller Polarimeter

The Møller polarimeter is an apparatus that exploits the process of Møller scattering of polarized electrons from polarized atomic electrons in a magnetized foil in order to measure the degree of polarization in the electron beam. For experiment E08-007,

this apparatus was used to measure the beam polarization several times throughout the experiment. Specifically, the Hall A Møller polarimeter was used to make measurements before, during, and after each production run.

The primary purpose of the polarimeter for this experiment was to provide the means to measure the longitudinal component of the beam polarization. To do this, the Møller polarimeter uses a ferromagnetic foil magnetized in a field of 24 mT along its plane as a target of polarized electrons. Furthermore, the target foil can be tilted at various angles to the beam in the horizontal plane, thus providing a target polarization that has both longitudinal and transverse components [46]. The spin of the incoming electron beam may also have transverse components due to the precession in the accelerator and in the extraction arc. In order to measure the longitudinal component of the beam polarization, the asymmetry was measured at two target angles of about $\pm 20^{\circ}$. In order to cancel the transverse asymmetries, these results were then averaged because at these angles they have opposite signs. This method also has the added benefit of reducing the impact of the uncertainty in the target angle measurements. Specifically, for a given target angle, two sets of measurements were taken for opposite target polarization directions. Averaging these results helps to cancel some of the false asymmetries including those coming from the residual helicity-driven asymmetry of the beam flux.

2.4.3 Chicane Magnet

The experimental NH_3 target used in experiment E08-007 was polarized by a 5 T magnetic field at $\sim 5.6^{\circ}$ towards the x -axis in the horizontal plane as described in the Hall Coordinate System (see Section 3.1.1). The transverse component of the magnetic field in the region of the target causes a downward deflection of the beam. To compensate for this effect, two chicane magnets shown in Figure 2.5 were placed in front of the target. The two dipole magnets were tuned based on simulations to correct the beam's initial deflection with the aim of getting it as close as possible to the center of the target in the horizontal orientation [35].

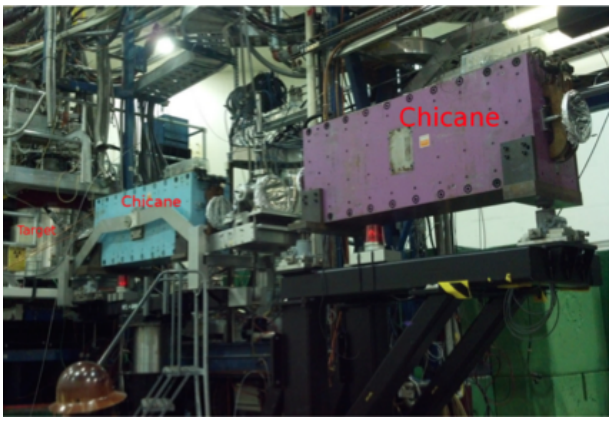

Figure 2.5: The two chicane magnets used to bend the beam.

2.4.4 Septum Magnets

Experiment E08-007 required the installation of two septum magnets in order to detect the scattered electrons at forward angles required to accommodate the spectrometers acceptance [27]. The scattering angles ranged from 4° to 7°. However, due to technical limitations the spectrometer arms could not accommodate angles below 12.5°. To compensate for this, the target was placed 88 cm upstream from the center of the Hall A coordinate system and two septum magnets were installed in front of the spectrometer. This was done to re-direct the desired scattering events into the spectrometer in order to detect these interactions [27]. However, a series of technical failures in the right septum occurred between the production runs configured at beam energies of 2.2 GeV and 1.7 GeV. As a consequence, the optics for the right arm of the spectrometer was difficult to work with, which required a different non-standard approach when analyzing this data. A schematic diagram of the septum magnet is shown in Figure 2.6.

2.4.5 High Resolution Spectrometer

The data was collected using the standard Hall A HRS configuration [46]. The spectrometers were positioned at 12.5° and the septum magnets were incorporated to achieve the smaller scattering angles required for the experiment. The detector package consisted of several components that provided information on particle trajectories,

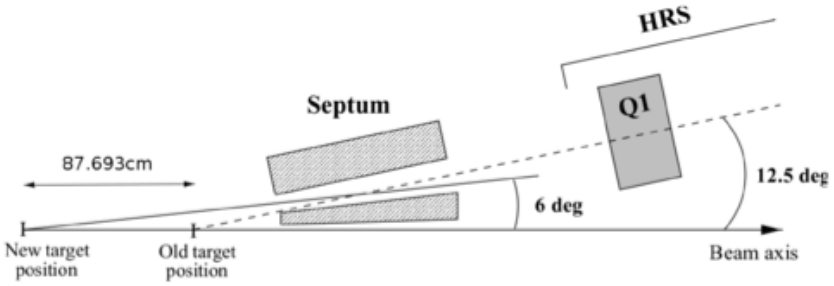

Figure 2.6: Illustration of septum magnets [35].

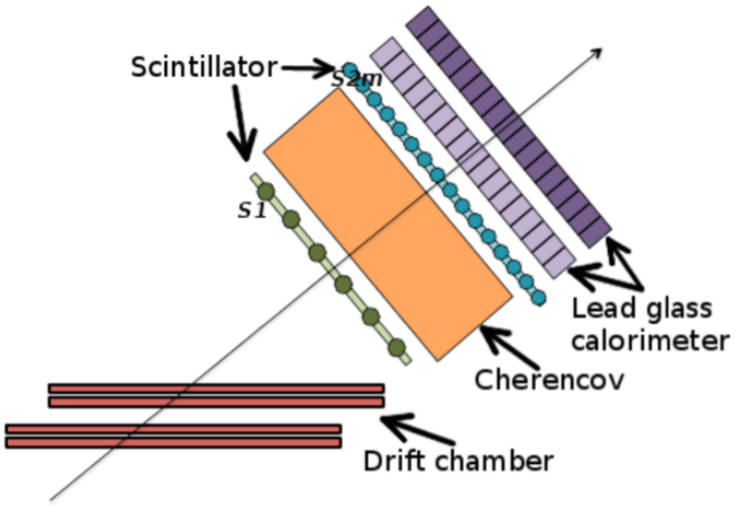

Figure 2.7: Layout of the detector package. The arrow illustrates particle trajectories.

identification, and event triggering[1]. A general layout of the HRS detector package is shown in Figure 2.7. This thesis focuses on the detector components that were relevant to experiment E08-007. In particular, the spectrometer's main magnet system directs incoming particles into the two Vertical Drift Chambers (VDCs) where the electron's momentum and trajectory information are extracted. The timing information and the main triggers are provided by two scintillator planes separated by a distance of two meters. In addition, due to the small scattering angle and energy transfer kinematics used in this experiment, particle identification was not needed. This was because the π^- momenta were emitted into the solid angle not associated with the desired elastic scattering peak.

[1]A detailed description of all detector package components can be found in Reference [46].

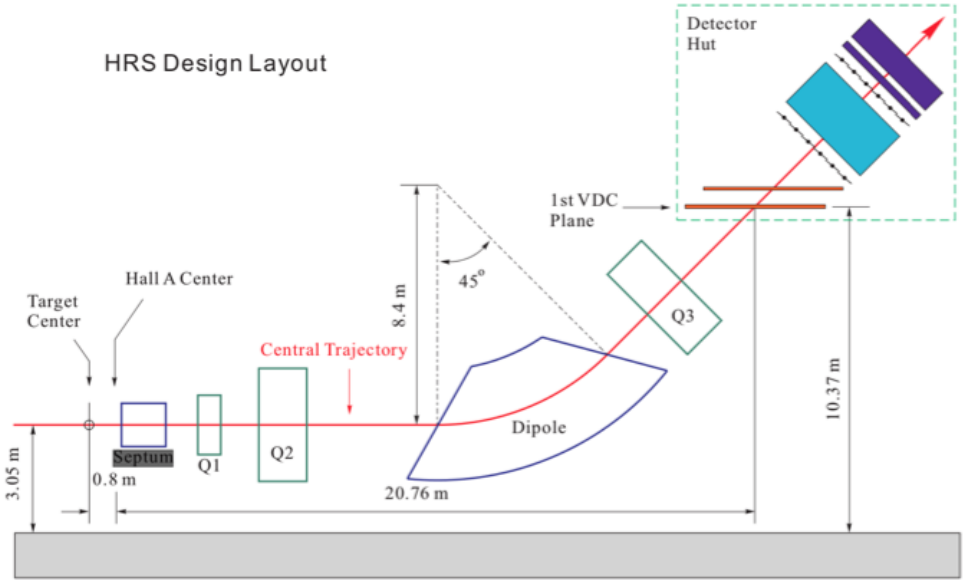

Figure 2.8: Layout of the HRS magnetic and detection systems in Hall A [35].

HRS Magnet System

The spectrometer contains four superconducting magnets in a quadrupole-quadrupole-dipole-quadrupole (QQDQ) configuration. This design directs the incoming charged particles into the detector system to optimize ability to detect their momentum and angle to very high precision. A schematic view of the HRS magnetic and detection systems are shown in Figure 2.8 while the spectrometer's main characteristics from Reference [46] are provided in Table 2.2.

The first two superconducting quadrupoles are used to focus the beam in both the vertical and transverse directions. The dipole magnet is used to bend the beam and map the momentum dispersion into a focal plane positional distribution. The remaining quadrupole makes final corrections to the deflected beam in the transverse direction. Each spectrometer has an effective vertical bend angle of 45° that deflects the beam into its HRS detector package [46].

Vertical Drift Chambers

The HRS detection packages both contain a set of VDC detectors. Each VDC chamber contains two wire planes that are separated by 335 mm and have the standard UV

Configuration	QQDQ vertical bend
Bend Angle	45°
Momentum Range	0.3 - 4.0 GeV
Momentum Acceptance	$\|\delta p/p\|<4.5\%$
Momentum Resolution (FWHM)	1×10^{-4}
Angular Range	
HRS-L	12.5 - 150°
HRS-R	12.5 - 150°
Angular Acceptance	
Horizontal	±28 mr
Vertical	±60 mr
Angular Resolution	
Horizontal	0.6 mr
Vertical	2.0 mr
Solid Angle	
(rectangular approximation)	6.7 msr
(elliptical approximation)	5.3 msr
Transverse Length Acceptance	±5 cm
Transverse Position Resolution	1 mm
Transverse Position Resolution (FWHM)	1.5 mm
Spectrometer Angle Determination Accuracy	0.1 mr

Table 2.2: Main design characteristics of the Hall A high resolution spectrometers showing their resolution and acceptance [46].

configuration as described in Reference [46]. In this configuration, the wires of each successive plane are oriented at 90° to one another and are horizontal. The VDCs are inclined at 45° with respect to the dispersive and non-dispersive directions in order to match the 45° angle that the spectrometer's magnetic system bends the scattered and recoil particles. As a result, particle trajectories cross the wire planes at an angle of 45°. There are a total of 368 wires in each plane that are spaced 4.24 mm apart. The electric field of the VDCs is shaped by gold plated Mylar planes nominally at -4.0 kV in a constantly circulated gas mixture of 62% argon and 38% ethane. When a charged particle passes through the VDC it ionizes the gas along its trajectory. The resulting ionized electrons then drift towards the wires along a well defined geodesic path[2]. The strength of those signals are related to the distance between the incoming particle and the wires associated with those signals [72].

Using the pattern of the affected wires in the four layers, a trajectory for the detected particle can be determined. If more than one possible trajectory is available, typically one is singled out. This selected trajectory is known as the "golden" track and its selection is based on a χ^2-minimization algorithm used in the software to analyze the VDC detections [72]. An illustration of the vertical drift chamber's detection planes is provided in Figure 2.9.

Scintillators

There are two scintillating planes labeled S1 and S2 in the detector package shown in Figure 2.7 that are spaced 2 m apart and are illustrated in Figure 2.10. Each plane consists of overlapping paddles made of thin plastic scintillating material to minimize hadron absorption (i.e., 5 mm BC4087) [46]. The S1 scintillator plane has 6 paddles in a 1×6 configuration while the S2 plane has 16 paddles in a 1×16 configuration that have active volumes of $0.5 \times 29.5 \times 35.5$ cm^3 and $0.5 \times 37.0 \times 54.0$ cm^3, respectively. Each scintillator paddle is connected to two photomultipliers tubes (PMT).

The purpose of incorporating scintillators was for triggering the data acquisition system. Every scintillator bar contained two PMTs, one located on each end of the bar. The PMTs send any particle detection signals to the data acquisition system. This system first looks for coincidences between the two PMTs from a single bar and

[2]The geodesic path is the path of minimum drift-time to the charged wires.

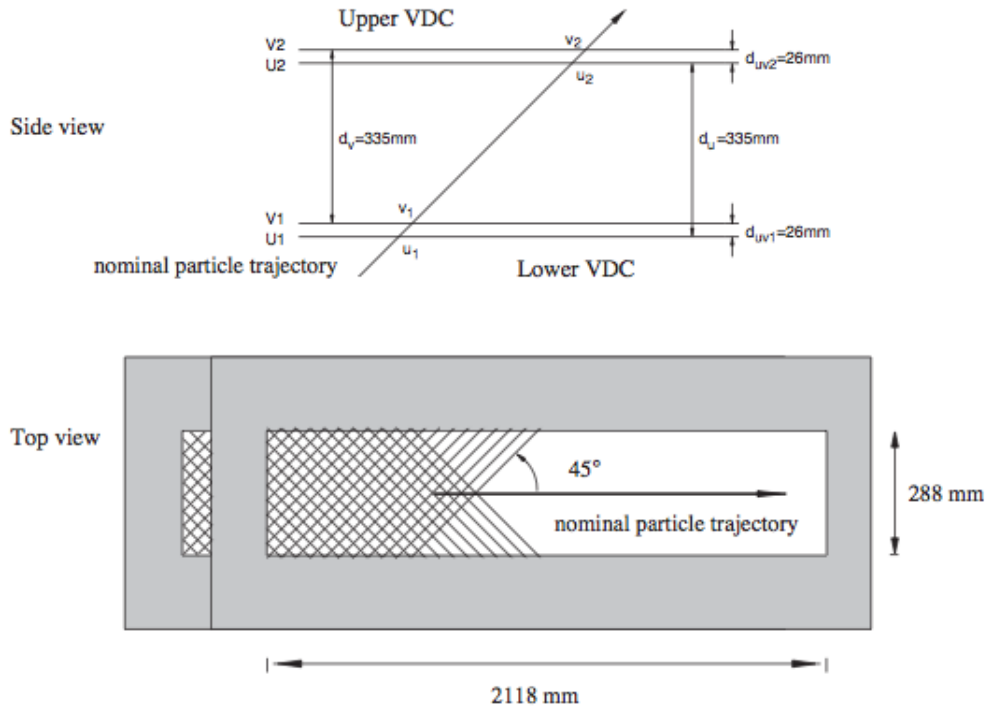

Figure 2.9: Schematic layout of a pair of Vertical Drift Chambers for one HRS. The active area of each wire plane is rectangular and has a size of 2118 mm x 288 mm. Each VDC consists of a single U and V wire plane with the lower VDC positioned as close as possible to the spectrometer's focal plane [46].

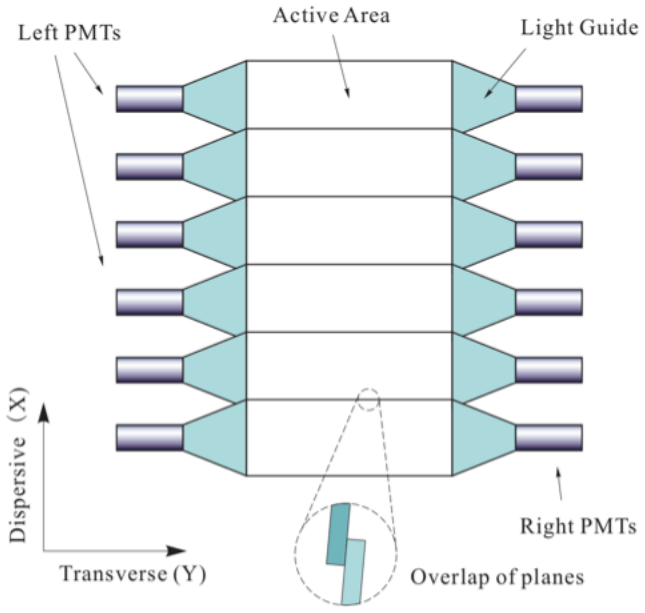

Figure 2.10: Layout of the scintillator planes used in the E08-007 experiment [35].

then looks for associated coincidences between the S1 and S2 scintillating planes. If two signals arrive within a predetermined timing window, the electronics determine that a particle has been detected and produces a pulse known as a 'trigger'. If two triggers occur within a 'coincidence window' a third signal is produced known as the 'coincidence trigger'. This indicates that a relevant experimental event may have occurred. In addition, the scintillators are also used for timing measurements. Typically, the length of the wires connecting the PMTs to the electronics is carefully exploited. This is done so that the signal from the PMTs on one side of one scintillator plane, such as the right side of the S2 plane, always arrive at the electronics last. This sets the timing of every other signal relative to that particular side. Thus allowing for a simple coincidence timing calculation between the two arms [72].

2.5 Polarized Target

A highly polarized proton target was needed for experiment E08-007 in order to extract data required to study the proton's structure using polarization asymmetries. The target used in this experiment was from the University of Virginia, which consisted of solid ammonia beads. This section discusses the processes used to: polarize the ammonia material using dynamic nuclear polarization (DNP), measure the degree of polarization using nuclear magnetic resonance (NMR), and calibrate the target using thermal equilibrium [73].

2.5.1 Dynamic Nuclear Polarization

The target polarization level P in ammonia is defined as the difference between the positive ($\uparrow$) and negative ($\downarrow$) alignment[3] of the nuclear spins relative to the polarization axis in the material divided by the total number of nuclear spin states by:

$$P = \frac{N_\uparrow - N_\downarrow}{N_\uparrow + N_\downarrow}, \tag{2.1}$$

where $N_\uparrow$ and $N_\downarrow$ correspond respectively to the number of $\pm$ nuclear spin states. The process begins with the cooling of the material to a low temperature and placing it in a strong magnetic field [71]. This process is known as thermal equilibrium polarization.

[3]The positive ($\uparrow$) and negative ($\downarrow$) nuclear spin alignments correspond to the z projection $m_z = \pm 1/2$ spin states.

For experiment E08-007, the ammonia target was cooled to a temperature of 1 K in a 5 T magnetic field [35]. The strong magnetic field causes Zeeman splitting[4] that creates two sub-levels having spin-1/2 protons. For a spin-1/2 target, the thermal equilibrium polarization process gives [35]:

$$P = \tanh\left[\frac{g\,\mu_x\,B}{K_B\,T}\right] \tag{2.2}$$

where g is the particles g-factor, B is the magnetic field, and μ_x is the magnetic moment of the particle[5]. For electrons, thermal equilibrium polarization can reach polarization levels above 90%. However, much lower polarization levels result for protons due to their lower μ_p value. For example, at a temperature of 0.5 K and a magnetic field of 5 T, the thermal equilibrium polarization for protons is ~ 0.01 whereas an electron approches ~ 1.00 [35]. Clearly, this is not practical for experimental purposes [71].

The Dynamic Nuclear Polarization (DNP) technique allows for the increase in the the nuclear polarization levels by applying microwave radiation to the target [35], which then takes advantage of electron-proton spin coupling [71]. The spin of the electron and the proton can be aligned by carefully tuning microwaves to the energy of the band gap between their two states [71]. However, the alignment of the electron and proton spins are not a permanent effect and only lasts on the order of tens of minutes. After which, the electrons relax back into their lowest energy state where they can then be reused to polarize additional protons [71]. As long as the rate of proton polarization is greater than the rate of proton relaxation, the polarization may be maintained using microwaves.

2.5.2 Target Material

When selecting the target material for an experiment a number of factors need to be considered. These requirements should include consideration of [73]:

- The degree of polarization that the material can obtain,

[4]Zeeman splitting is the effect of splitting a spectral line into several components in the presence of a static magnetic field.

[5]The proton and electron magnetic moments μ_x are represented respectively by μ_p and μ_e.

- The ratio of free polarizable nucleons to the total number of nucleons in the target as quantified by its dilution factor[6], and

- The ability of the target to resist radiation damage.

The choice of NH_3 as the proton target for experiment E08-007 was made for the following reasons. First, this target was capable of reaching polarization levels above 90% at a magnetic field strength of 5 T [71]. Second, it polarizes very quickly on the order of 30 minutes or less. An additional concern is that radiation damage is usually a main cause for reductions in the achievable levels of polarization. Therefore, this target was chosen because of its high resistance to radiation damage and the fact that it recovers from this damage via low temperature annealing at $\sim$77 K [73].

The solid NH_3 used in experiment E08-007 was formed into approximately 2 mm diameter beads. These beads were prepared by the polarized target lab at the University of Virginia by condensing ammonia gas and sealing it in a stainless steel tub coated with teflon [35]. The whole assembly was then cooled in a liquid nitrogen bath. Once frozen, the solid ammonium was forced through a mesh in order to form the beads.

2.5.3 Target Setup

The standard University of Virginia polarized target was used by experiment E08-007 [35]. Figure 2.11 shows the general setup of the target whose main components are a superconducting 5 T Target Polarization Magnet, a Target Refrigeration Unit, a Microwave System, a NMR Readout System, and the Target Insert.

Target Magnet

An extensive setup procedure is needed to maintain the low temperature and the high magnetic field required by the DNP process. Several months prior to the experiment, the target magnet was damaged beyond repair during testing prior to its installation in Hall A when it shorted during a large quench. Fortunately, an alternative magnet from Hall B was identified as a suitable replacement and the target group was able to

[6]The dilution factor is defined to be the fraction of free polarizable protons to the total number of nucleons in the target.

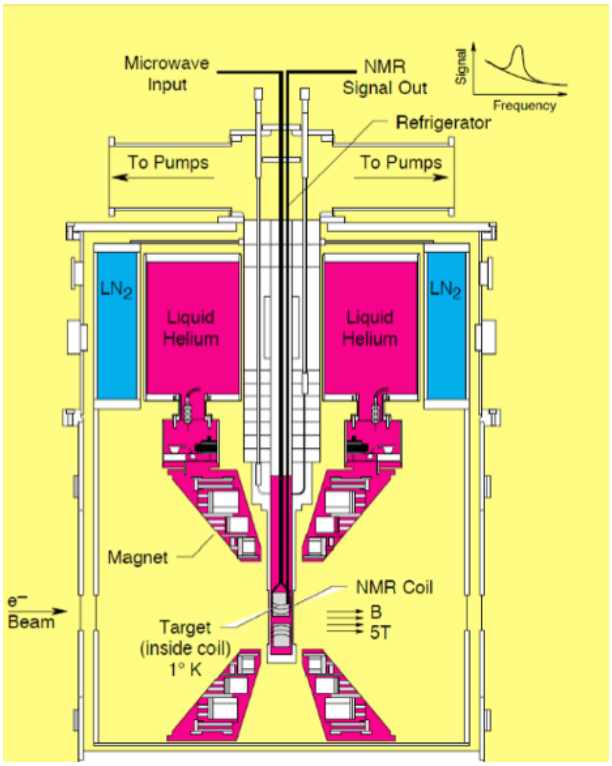

Figure 2.11: Schematic of the target assembly and its major components. This figure illustrates the location of the target, the location of the beam's input and the target polarization field orientation, as well as the NMR coil used to measure the target's polarization. Also shown, are the major refrigeration elements and the access points used to inject the microwave input and retrieve the NMR output signals from this assembly [35].

modify it quite successfully [71]. As a result, a strong uniform magnetic field over the target volume ensured an efficient DNP process. The magnet was designed with an open geometry that allowed the beam to pass through the target then on to the HRS arms. This design also permitted operations in both the parallel and perpendicular magnetic field configurations [35].

Target Refrigeration Unit

The original target refrigeration unit was damaged in a previous experiment so a new ^{4}He unit was used during this experiment to cool the target to $\sim$1 K [35]. This unit was installed vertically along the central-axis of the target magnet [73]. For further details on this unit, refer to References [74, 75].

Microwave System

The microwave system is used by the DNP process to increase the nuclear polarization levels via application of microwave radiation to the target. This system consists of a microwave chamber used to generate the microwaves, a motor control unit used by the system to change the frequency of microwaves by altering the chamber's length, a water cooling system, a high voltage power supply, a power meter used to measure the frequency, and a circular wave guide system used to transport the microwaves to the target [73].

The actual generation of the microwaves occurs at the Extended Interaction Oscillator tube (EIO)[7]. The use of a 5 T magnetic field requires microwaves at a frequency of 140 GHz.

NMR Readout System

Nuclear magnetic resonance is a physical phenomenon where nuclei in the presence of a magnetic field absorb and re-emit electromagnetic radiation. When the nuclear magnetic moment associated with a specific nuclear spin is placed in an external magnetic field the different spin states have different magnetic potential energies[8].

[7]The extended interaction oscillator tube is a linear-beam vacuum tube designed to convert direct current to RF power.

[8]The nuclear magnetic moment, also known as the magnetic dipole moment, has a potential energy that is related to its orientation with respect to the external magnetic field.

The presence of the static magnetic field produces a small amount of spin polarization and an RF signal of the proper frequency can be used to induce a transition between spin states. This results in some of the spin states transiting to higher energy states. If the RF energy is then switched off, the relaxation of the spins back to their lower energy states produce a measurable amount of RF signal at the resonant frequency associated with these transitions. This process is called NMR.

Note that the electron and proton spin magnetic moments are respectively 180° and 0° in alignment with their respective spins. These spins tend to precess around the magnetic field with the Larmor frequency[9]. As a practical technique, a sample containing protons is placed in a strong magnetic field to produce partial polarization while the application of a strong RF field is used to excite some of the nuclear spins into their higher energy states. When the strong RF signal is switched off, the spins tend to return to their lower energy states, producing a small amount of RF signal at the Larmor frequency. It is this signal that is detected in a coil and then amplified to produce a measurable NMR signal that is used to measure the polarization level of the target.

Target Insert

The target insert consists of several cells as shown in Figure 2.12. The insert contains two cells with NH_3 targets that were used during production runs, and a dummy cell that was used to calculate the dilution factor of the target[10]. In addition, the insert has a carbon cell and two holes for loading CH_2 and carbon foils used for performing optics studies [73].

[9]The frequency of precession of the magnetic moment of an object about an external magnetic field is known as the Larmor frequency.

[10]The dummy cell has the same structure as the NH_3 cells without the ammonia beads.

Figure 2.12: This figure shows the vertical orientation of the target insert shown in Figure 2.11 along with the placement of each of its target cells. In particular, it highlights the locations associated with the top and bottom NH_3 targets, the carbon and dummy targets, as well as the CH_2 target and the position of the carbon holes [73].

2.6 Data Acquisition

The standard HRS Hall A data acquisition system (DAQ) was utilized during experiment E08-007 [35]. The scintillator plates S1 and S2 used a logical 'AND' signal as a trigger. Note the trigger efficiency was not determined for the asymmetry portion of the experiment, but it was estimated to be above 99% based upon the Cherenkov analysis done during this experiment. In addition, two scaler modules were employed. The first was the SIS3800 module acting as a counter where both the charge and clock signals were used as triggers. The second module, the SIS3801 acted as a ring buffer triggered by the helicity state. When so triggered, it saved the current helicity signals stored in the SIS3800 before clearing its buffer.

The helicity of the beam was set using a helicity control board. The orientation of the laser polarization was controlled by the level of the high voltage supply. As a result, this determined the sign of the helicity. The helicity was produced pseudo randomly in either a "$-++-$" or "$+--+$" pattern. The helicity control board also generates outputs that were sent to the experimental hall to be recorded and used to set helicity values of detected events by the off-line reconstruction process [76].

The target polarization was measured with a continuous-wave NMR coil and an enclosure containing two separate Q-meters[11] and Yale gain cards[12] for the two different target cells seen in Figure 2.12. The signals from the Q-meters were passed through the Yale gain cards before digitization. To enhance the signal-to-noise ratio, signal averaging was employed during a single target event associated with a given time stamp. The integration of the averaged signal provided a NMR polarization area for that event. Each target event was then recorded. All NMR system parameters and target environmental variables needed to calculate the final polarizations were written and stored in these records.

[11] A Q-meter is a piece of equipment used in the testing of radio frequency circuits. In particular, it measures the quality factor of a circuit which expresses how much energy is stored to how much is dissipated per cycle.

[12] Yale-gain cards provide addition signal amplification prior to signal digitization.

Chapter 3

Analysis

The overall analysis for the polarized target part of experiment E08-007 will be described in this chapter. The analysis requires an understanding of the different coordinate systems that are used to analyze spectrometer measurements and to make calculations. This includes creating the standard Hall A reaction variables following the normal processes used for reconstruction, and those used to calibrate the optics of the two spectrometers. The presence of the target magnetic field deflected the beam prior to interacting with the target. In order to correct for this effect, chicane magnets were used to correct the beam deflections. The loss of beam position monitoring (BPM) data for the right arm and issues with one of the magnets in the spectrometer precluded using the normal reconstruction process typically used during the analysis phase. In order to analyze the right arm data, a novel approach was developed to overcome these short comings. This chapter will discuss how the reconstruction process was achieved using simulated data to represent the reaction components responsible for the measured events in the spectrometer. Using these simulated reaction components, a fitting process was developed to fit the measured momentum spectrum in the focal plane. The subsequent elastic hydrogen reaction components obtained for each helicity state via the fitting process were then used to extract the raw asymmetries used to estimate the form factor ratios. In the following sections, the spectrometer optics and the reconstruction processes are discussed, along with the approach taken to analyze the right arm data.

3.1 Spectrometer Optics

The spectrometer optics are used to determine the physical variables of the scattering process at the target from the measured quantities made at the detector package. The standard optics studies were performed for experiment E08-007 with modifications to account for the effect of the target and septa magnetic fields [77, 35]. A detailed

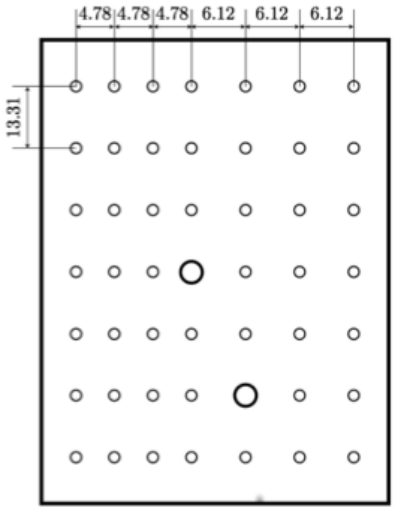

Figure 3.1: Geometric configuration of the sieve slit where dimensions are given in mm. The two large holes in the plate are used to determine the orientation of the sieve slit and have a diameter of 2.7 mm. The smaller sized holes have a diameter of 1.4 mm [78].

description of this procedure can be found in Reference [78]. The sieve slit plates shown in Figure 3.1 were placed in front of the septum magnets in order to perform the optics studies required to calibrate the spectrometers. These calibrations were required in order to reconstruct scattering events back to the target vertex. To understand this process requires an understanding of the different Hall A coordinate systems. A brief description is provided below; however, a more detailed account of these coordinate systems can be found in Reference [77].

3.1.1 Definition of Coordinate Systems used in Hall A

Hall A uses a number of different coordinate systems in order to support its description of various required vectors in data analysis. All of the coordinate systems used in Hall A are Cartesian style reference frames. In this section, brief descriptions of these different coordinate systems are provided.

Hall Coordinate System

The Hall A coordinate system (HCS) uses a Cartesian frame of reference to define the primary directions in the experimental hall. The origin of the HCS is located at

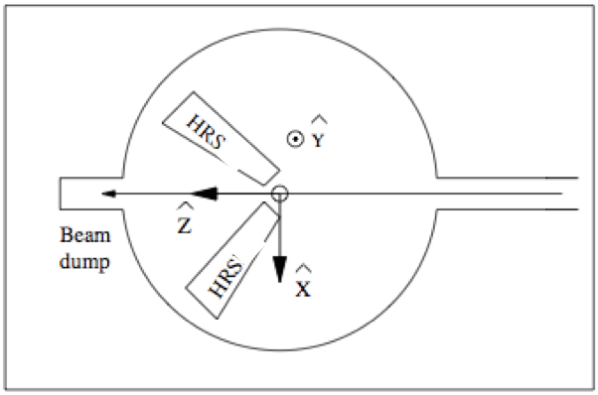

Figure 3.2: Hall A Coordinate System [77].

the center of the hall, which is defined to be the intersection of the electron beam and the vertical symmetry axis of the target system [77]. The positive z-axis ($\hat{z}$) is along the beam line and points in the direction of the beam dump. The positive y-axis ($\hat{y}$) points vertically upward and the positive x-axis ($\hat{x}$) points to the left of where the beam enters, as seen in Figure 3.2.

Target Coordinate System

Each spectrometer has its own Target Coordinate System (TCS). For a given spectrometer, the z-axis of the TCS $\hat{z}_{tg}$ is defined by the line perpendicular to the sieve slit surface that goes through the midpoint of the central hole in the plate. The corresponding $\hat{y}_{tg}$ axis points to the right facing the spectrometer while the $\hat{x}_{tg}$ axis points vertically downwards as illustrated in Figure 3.3.

The ideal case corresponds to when the spectrometer points directly at the hall's center and the sieve slit is perfectly centered on the spectrometer. When this occurs, the TCS has the same origin as the HCS. However, the TCS typically deviates from the HCS by factors D_x and D_y in the vertical and horizontal directions, respectively. These offsets are typically obtained via survey data [28].

The TCS variables are used to calculate the scattering angle θ and the reaction point z_{react} along the beam line for each event. In addition, the angles θ_{tg} and ϕ_{tg}, as well as, the reaction point at the target are determined via optics studies that use the sieve hole positions. A more detailed explanation is provided in Reference [28].

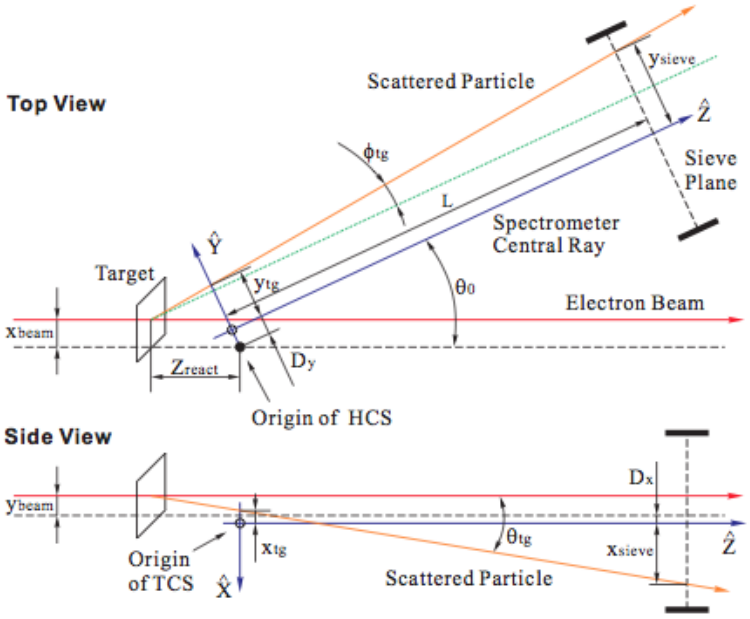

Figure 3.3: Target Coordinate System [28].

Detector Coordinate System

The Detector Coordinate System (DCS) is defined with respect to the vertical drift chambers (VDC) located in the detector packages. Specifically, the DCS origin is defined by the intersection of wire No. 184 (the middle wire) of the first plane (VDC1 U1) and the perpendicular projection of that wire onto the second plane (VDC2 V1) of the vertical drift chambers as illustrated in Figure 3.4. From this figure, the positive z-axis $\hat{z}$ is seen to be perpendicular to VDC U1 pointing vertically upward, while it is seen that the y-axis $\hat{y}$ and x-axis $\hat{x}$ are respectively parallel to the short and long symmetry axes of the VDC [77]. The coordinates of the detector vertex can be calculated using the particle trajectory intersection points with the four VDC planes illustrated in Figure 3.5. In this figure, the four planes are respectively labelled U1, V1, U2, and V2. When a particle is detected using the VDCs, the following angular and spatial coordinates θ_{det}, ϕ_{det}, x_{det}, and y_{det} are respectively calculated using this coordinate system. The details of their calculations are provided in the following References [77, 79]. These angular and spatial coordinates are then used by the Transport Coordinate System to translate VDC detections to the focal plane of the spectrometer.

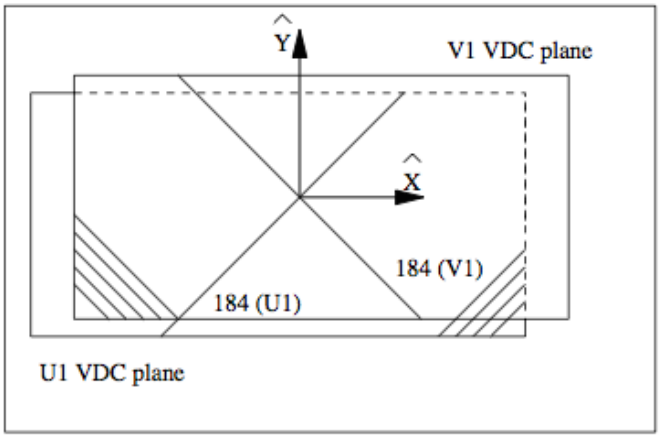

Figure 3.4: Vertical Drift Chamber Detector Coordinate System [77].

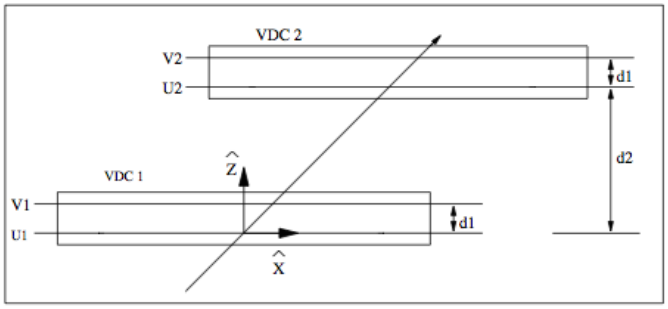

Figure 3.5: Four planes of the VDC [77].

Transport Coordinate System

The Transport Coordinate System TRCS is an intermediate reference frame used to transport DCS detections to the focal plane of the spectrometer. Transport to the focal plane is accomplished by performing a 45° clockwise rotation of the DCS coordinates around its $\hat{y}$-axis as illustrated in Figure 3.6. This rotation results in the following set of equations that represent DCS detections in transport coordinates where ρ_0 is the rotation angle (-45°) [35]:

$$\begin{aligned} \theta_{tra} &= \frac{\theta_{det} + \tan\rho_0}{1 - \theta_{det}\tan\rho_0} \\ \phi_{tra} &= \frac{\phi_{det}}{\cos\rho_0\,(1 - \theta_{det}\tan\rho_0)} \\ x_{tra} &= x_{det}\cos\rho_0\ (1 + \theta_{tra}\tan\rho_0) \\ y_{tra} &= y_{det} + \sin\rho_0\,\phi_{tra}\,x_{det} \end{aligned} \tag{3.1}$$

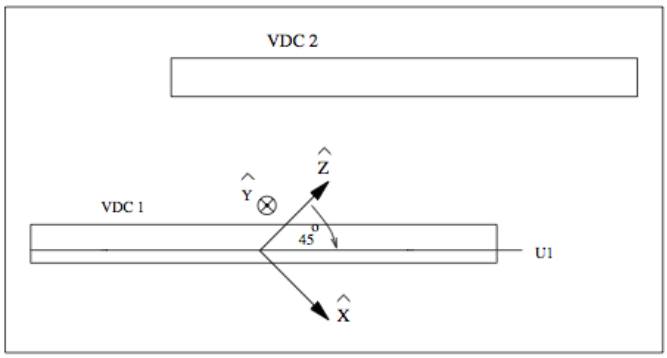

Figure 3.6: Vertical Drift Chamber Transport Coordinate System [77].

Focal Plane Coordinate System

Due to the focusing provided by the HRS magnetic system, particles from different scattering angles having the same momentum are focused in the focal plane. The Focal Plane Coordinate System (FCS) is obtained by rotating the DCS around its $\hat{y}$-axis by an angle ρ, where ρ is the angle between the local central ray[1] and the DCS $\hat{z}$-axis as seen in Figure 3.7. In this rotated system, the dispersive angle θ_{fp} is small for all points across the focal plane. As a result, the expressions for the reconstructed vertex converge faster during optics calibrations [28]. The FCS transformation also includes corrections for the offsets incurred due to misalignments in the VDC packages. The processes used to calibrate the optics of the Hall A spectrometers are more fully described in Reference [77].

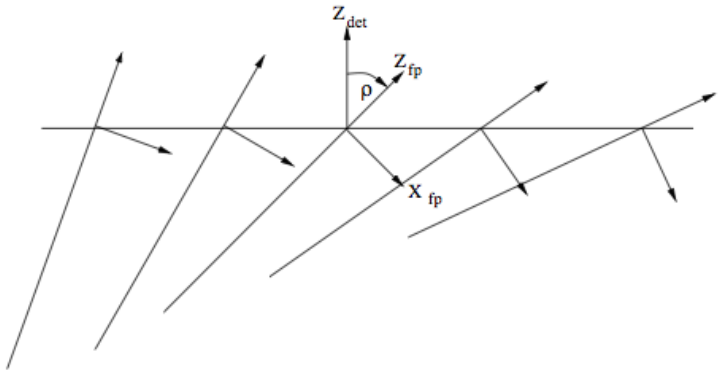

Figure 3.7: The Focal Plane Coordinate System (FCS). [77].

[1]The local central ray is the one with TCS coordinates θ_{tg}, $\phi_{tg} = 0$ with corresponding relative momentum $\frac{\Delta p}{p}$.

3.1.2 Analysis Coordinate Systems

To support the overall analysis process, two additional coordinate systems were utilized in this study. The first, was the Scattering Plane Coordinate System (SPCS), and the second, was the Starred Coordinate System (SCS). These reference frames will now be discussed.

Scattering Plane Coordinate System

The scattering plane coordinate system used in this report defines the $\hat{u}_z$-axis as the direction of the difference between the incoming and scattered electron's momentum $\vec{q} = \vec{k} - \vec{k}'$. The scattering angle θ is defined as the angle between $\vec{k}$ and its scattered momentum vector $\vec{k}'$ as illustrated in Figure 3.8. These quantities are expressed as:

$$\begin{aligned} \hat{u}_z &= \frac{\vec{q}}{|\vec{q}|} \\ \cos\theta &= \frac{\vec{k} \cdot \vec{k}'}{|\vec{k}| \cdot |\vec{k}'|} \end{aligned} \tag{3.2}$$

In this analysis, the azimuthal angle ϕ is arbitrary and plays no part in the calculation of asymmetry or the form factor ratio. However, its sole importance is that it defines the scattering plane required to calculate the starred coordinates discussed in the next section.

Starred Coordinate System

The starred coordinate system is the reference frame having coordinates θ^* and ϕ^* shown in Figure 3.8. This coordinate system is used to perform asymmetry calculations. The normal to the scattering plane is defined by $\vec{k}$ and the virtual photon's momentum $\vec{q}=\vec{k} - \vec{k}'$ in the following manner:

$$\vec{n}_1 = \vec{q} \times \vec{k}, \tag{3.3}$$

and the normal to the plane containing the virtual photon momentum and target polarization $\vec{S}$ is given by:

$$\vec{n}_2 = \vec{q} \times \vec{S} \tag{3.4}$$

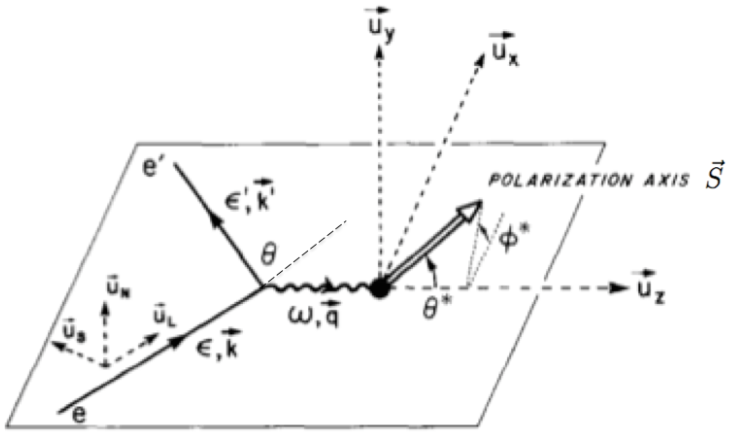

Figure 3.8: Coordinate systems for the scattering of polarized electrons from polarized target. In this figure, the vectors $\vec{u}_N$ and $\vec{u}_L$ are respectively normal to the scattering plane and parallel to $\vec{k}$ with $\vec{u}_S = \vec{u}_N \times \vec{u}_L$. The starred coordinate system is defined by vectors $\vec{u}_z = \vec{q}$, $\vec{u}_y = \vec{k} \times \vec{k}'$, and $\vec{u}_x = \vec{u}_y \times \vec{u}_z$. Illustration taken from Reference [36].

Using these two last expressions, the starred coordinates are defined as:

$$\begin{aligned} \theta^* &= \arccos\left(\frac{\vec{q}\cdot\vec{S}}{|\vec{q}|\cdot|\vec{S}|}\right) \\ \phi^* &= \arccos\left(\frac{\vec{n}_1\cdot\vec{n}_2}{|\vec{n}_1|\cdot|\vec{n}_2|}\right) \end{aligned} \tag{3.5}$$

Unlike the scattering azimuthal angle ϕ, the azimuthal angle ϕ^* is required for calculating the proton form factor ratio $\mu_p \frac{G_E^p}{G_M^p}$.

3.1.3 Reaction Variable Reconstruction

Standard Approach

The standard reconstruction process for the HRS variables is provided in [77]. The trajectories of particles are reconstructed when no target field is present to prevent any additional disturbances to the detected particles. This experiment, however, utilizes a 5 T magnet that provides a magnetic field presence around the target, complicating the reconstruction process. As a result, the optics calibration and analysis are completed separately. Trajectories between the target and the septum magnet entrance are calculated using simulations of the electron motion in the magnetic field.

The magnetic field is characterized by applying the Biot-Savart law to the current density distribution, and a cross-check is done by direct measurement of the target field. The reconstruction of the trajectories from the focal plane to the entrance of the septa is done using the optics matrix. The optics matrix correlates the focal plane variables with the TCS variables θ_{tg}, y_{tg}, ϕ_{tg}, and the delta momentum variable:

$$\delta = \frac{P - P_0}{P_0}, \tag{3.6}$$

where P is the particle momentum and P_0 is the HRS central momentum. During the calibration, x_{tg} is effectively set to zero. The optics matrix, to the first order approximation, can be expressed as:

$$\begin{pmatrix} \delta \\ \theta \\ y \\ \phi \end{pmatrix}_{tg} = \begin{pmatrix} \langle\delta|x\rangle & \langle\delta|\theta\rangle & 0 & 0 \\ \langle\theta|x\rangle & \langle\theta|\theta\rangle & 0 & 0 \\ 0 & 0 & \langle y|y\rangle & \langle y|\phi\rangle \\ 0 & 0 & \langle\phi|y\rangle & \langle\phi|\phi\rangle \end{pmatrix} \begin{pmatrix} x \\ \theta \\ y \\ \phi \end{pmatrix}_{fp} \tag{3.7}$$

The optimization of the matrix is done using the sieve slit and is based on the well known behaviour of elastic scattering and the measured survey data. The simulation of the magnetic field is required for the optics matrix optimization since linear propagation of the trajectories from the target to the sieve slit cannot be assumed [81].

Reconstruction Approach for the Right Spectrometer

In experiment E08-007, the standard reconstruction process could not be used due to magnet issues and a loss of BPM data[2]. In particular, the magnet issues in the right spectrometer seem to have distorted the measured momentum distributions observed in the focal plane. This effect, is also apparent in the target frame where it seems to manifest as a bifurcation in the observed distributions of the data. When comparing the left and right spectrometer data shown in Figures 3.9 and 3.10, this effect is clearly seen; the data distributions shown are samples using the 2.2 GeV beam energy at the settings listed in Table 3.1

[2]Details on the BPM system can be found in [46].

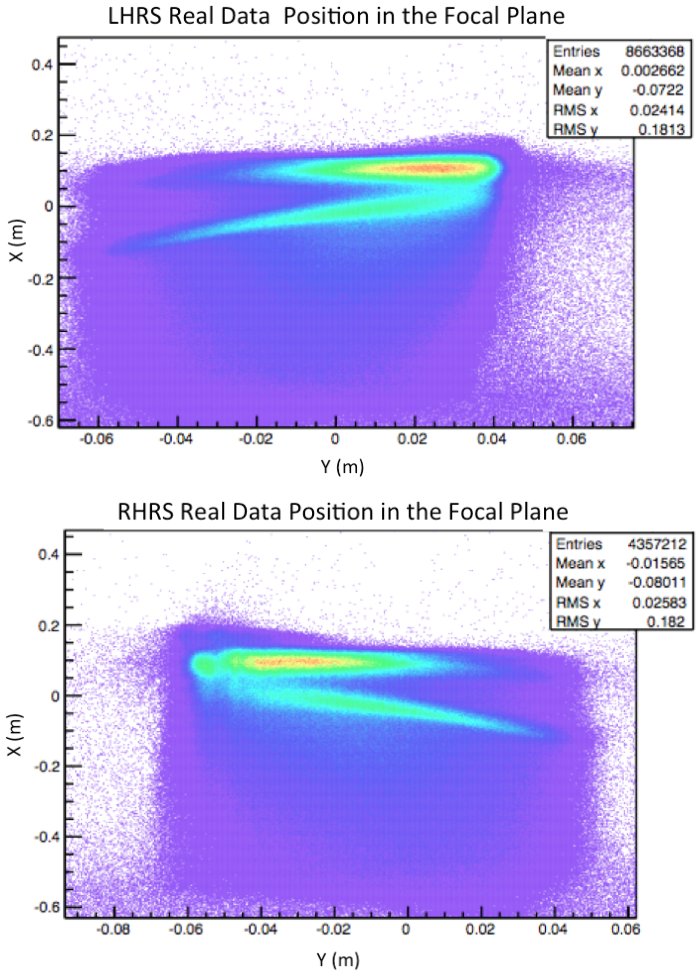

Figure 3.9: Left HRS and right HRS positional distributions of the data when observed in the focal plane coordinate system.

Figure 3.9 illustrates the distribution of the events in terms of the focal plane positional variables, x and y. The dense yellow and red events in these distributions represent mostly the heavy elastic reaction components associated with He and N, while the lower slanted less dense sweeping distribution represents the region where the elastic hydrogen events are found. When comparing the plots for the left and right arms, it is clear that the right events are being distributed differently than those of the left in the region $-0.06 \leq y \leq -0.05$ m. Furthermore, Figure 3.10 shows the same events in terms of the target plane positional variables. In this representation, a distinct difference in the distributions are apparent. The right plot shows a clear split, or bifurcation, in the right arm distributions. Such an effect suggests that

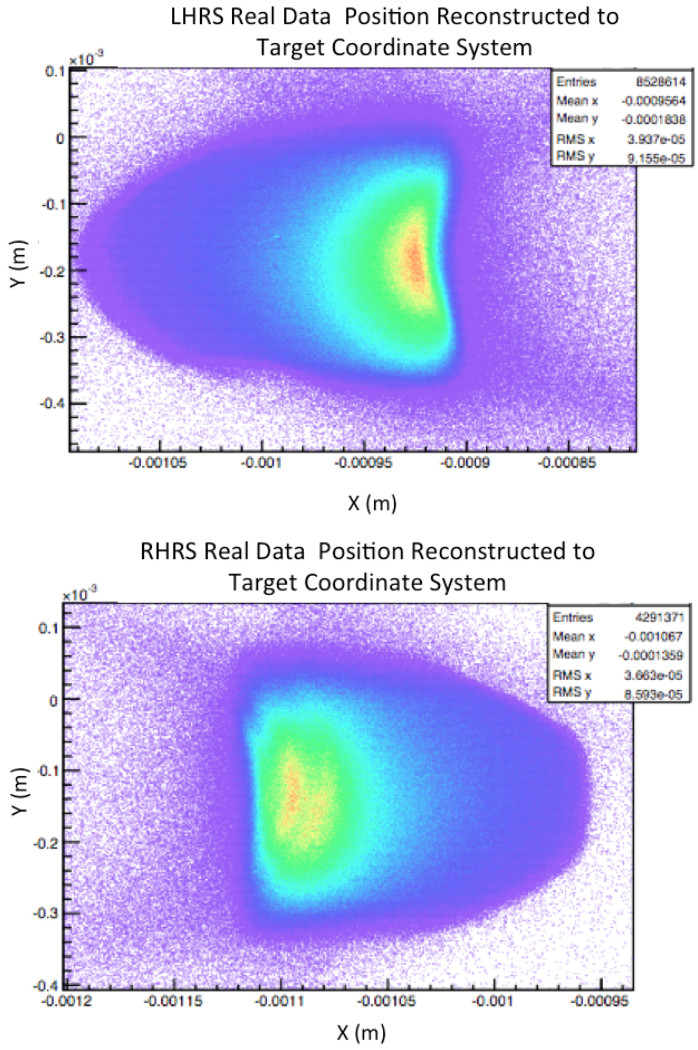

Figure 3.10: Left HRS and right HRS positional distributions of the data when observed in the target coordinate system.

the events are mapped to two different interaction points, which is not physically possible. As a result, the standard optics and reconstruction approaches cannot be used to analyze the right arm data.

The beam position information usually provides a non-invasive measurement of the position and direction of the beam at the location of the target. This information is used as part of the reconstruction of detected events back to the target in order to determine their kinematics. To complicate matters further, the beam current was reduced to ∼10 nA to improve the degradation of the target's polarization. However, this resulted in the loss of the beam position information. In order to compensate

beam energy (GeV)	Field	TCS x	TCS y	θ_b	ϕ_b
2.2	5 T	-0.19	1.00	17.93	-2.36
2.2	5 T	-0.04	-1.28	16.00	-2.15
2.2	5 T	-3.99	23.72	39.54	-24.07

Table 3.1: Mean BPM entries are in mm and mrad.

for this loss, the required information was obtained using a simulation [35] and has been provided as average quantities in Table 3.1 above. These data were then used in the analysis to support reconstruction of the interaction variables via simulation. In particular, they were used to simulate events for each reaction component first for the reconstruction of the HRS variables, and secondly, to transform from the HRS to the scattering coordinate system, where the physical reaction momentum vectors are analyzed. This simulation was developed by the g_2^p team to support experiment E08-027, which was designed to measure g_2^p for a polarized proton target over the range $0.02 \leq Q^2 \leq 0.40$ GeV^2. This range of Q^2 encompasses the values shown for the central kinematics associated with experiment E08-007 provided in Table 2.1. As such, this suggests that the g_2^p simulation may be a suitable tool for supporting the analysis of the right arm data in this analysis.

Given the aforementioned issues, an alternative method for analyzing the right arm data was developed that uses the g_2^p simulation to create and fit reaction components to the measured momentum distributions. This simulation and fitting process are discussed in the following sections.

3.2 Methodology

The methodology developed to extract asymmetries and DSA form factor ratios using the data from experiment E08-007 will now be discussed. In particular, the following sections describe the data processing performed, the g_2^p team's simulation g2psim, the fitting process that was developed, the extraction process used to generate asymmetry estimates, and the generation of both single arm and DSA form factor ratios.

3.2.1 Data Processing

In order to process the extracted data from the spectrometers, it was decided to focus on generating focal plane momentum spectra, given that the standard reconstruction process could not be used to analyze the right arm data. Since the process of interest was electron-proton elastic scattering, and the magnet issues with the right arm still allow a reasonable momentum reconstruction, elastic events remain identifiable in the basic moderate-resolution momentum spectra. These spectra then formed the basis upon which to start our analysis because, as stated, the spectrometers are known to measure the momentum sufficiently accurately even in the light of the right arm's magnet and BPM issues. For each energy setting, an initial cut in momentum was chosen that captured the overall characteristics of the spectra. Namely, the radiative tail and the peaks associated with the elastic scattering events. The approach taken here was to then simulate each "reaction component" using g2psim so that they could then be used to generate an overall model that could be fit to these spectra. For this purpose, "reaction component" refers to those physical processes that contribute to (e, e') reactions from target elements that populate the focal plane (this will be explained in detail later). Such an approach, if done properly should account for the overall background and provide an estimate of the elastic hydrogen component to support the extraction of asymmetry data. This process also negates the need to estimate a dilution factor as it is already accounted for via the estimated background. Furthermore, these simulated events would also allow for the generation of kinematic variables required to support the estimation of both single arm and DSA form factor ratios, since determination of kinematic quantities on an event-by-event basis using the data was not reliably possible with the right arm.

3.2.2 Monte Carlo Simulation

The Monte-Carlo simulation, g2psim, was developed to support optics studies and data analysis. Furthermore, it models the "reaction components" associated with the experimental conditions seen in experiment E08-007. The simulation includes the field map of the trajectory of the scattered electrons, as well as, the calibration of the optics matrix. The particle trajectories are calculated by integration of the equation

of motion in the magnetic fields using the Runge-Kutta-Nyström method[3]. Energy losses due to ionization, electron scattering, internal and external Bremsstrahlung are accounted for as described in Reference [80]. In addition, the simulation calculates and adds an average value to correct for the energy losses before $E_{loss,b}$ and after $E_{loss,a}$ the scattering interaction. The reaction energies before E and after E' the scattering events are given by:

$$\begin{aligned} E &= E_{beam} - E_{loss,b} \\ E' &= E_{detected} + E_{loss,a} \end{aligned} \tag{3.8}$$

To support the analysis role, g2psim contains elastic models for protons, ^{4}He, ^{12}C and ^{14}N, which were coded based on experimental-based form factor parameterizations [7, 82]. However, inelastic data at the relevant kinematics were not available. To compensate for this, the simulation models inelastic scattering components using the QFS[4] and PBosted[5] models [83, 84]. Reference [35] found that the two inelastic models produced different yields at the quasi-elastic region for the chosen kinematics by comparing unpublished nitrogen data at similar kinematics for these models, it was found that the PBosted model produced more accurate results at the quasi-elastic peak. For this reason, the PBosted model was chosen here over the QFS model to support the overall fitting process developed to analyze the right arm data.

3.2.3 The Fitting Process

The fitting process starts by using g2psim to generate momentum histograms for (e, e') events from each simulated reaction component at the relevant kinematics (within the spectrometer physical acceptance) for each of the spectrometer arms. This was done using the g2psim simulation discussed in the previous section. In particular, the elastic models in g2psim are used to simulate events for hydrogen, helium, and nitrogen along with quasi-elastic simulations using the PBosted model to simulate events for helium and nitrogen (noting that the Virginia polarized target, previously discussed, contains helium and nitrogen in the beam path, along with the primary hydrogen

[3]The Runge-Kutta-Nyström method includes formulae for the numerical integration of ρ-reversible second order ordinary differential equations.

[4]The QFS model covers an electron beam energy range of $0.5-5$ GeV.

[5]The PBosted model covers a Q^2 range of $0.2 < Q^2 < 1$ GeV^2.

target material). These simulated events are then used to create the reaction component momentum histograms $h_k[P_m]$ used in the fitting process, where P_m represents the measured momentum that results from g2psim transporting the simulated events to the focal plane. Each histogram $h_k[P_m]$ corresponds to the elastic (H, He, N) and quasi-elastic (He, N) reaction components that are respectively identified by the subscript $k=0\ldots4$ in the overall fit model.

For each simulated reaction component, k, the histograms $h_k[P_m]$ are transformed as a function of the measured momentum P_m to specifically create a scaled γ_k, skewed α_k, and shifted β_k version of itself using:

$$H_k\left[P_m\right] = \gamma_k\, h_k\left[\alpha_k\left(P_m - \beta_k\right)\right]. \tag{3.9}$$

This was done as a method to account for the unknown potential "shifts" in our interpretation of momentum in the spectrometer data due to the septum magnet (and BPM) problems noted in Chapter 2. The final fit model is then given by the sum of these simulated reaction components:

$$H\left[P_m\right] = \sum_k H_k\left[P_m\right] \tag{3.10}$$

and has a total of fifteen free parameters to accommodate the fitting process. The fit parameters α_k, β_k, and γ_k obtained for each reaction component via the fitting process are provided in Appendix A[6].

In order to prepare each reaction component to support the overall fit process, their histograms are smoothed and splined using ROOT [85]. The splined histograms are then used to define each of the functions $H_k\left[P_m\right]$. Once these functions have been defined, they are initially "placed" in appropriate regions under the measured momentum spectrum. The elastic H, He, and N are placed under the corresponding elastic peaks while the quasi-elastic components for He and N initially reside under the radiative tail of the spectrum being fitted. To accomplish this, momentum markers are determined and placed on each spectrum, and appear as vertical dashed lines to give a visual cue as to where the reaction components are placed prior to fitting as illustrated in Figure 3.11.

[6]Appendix A provides the 2.2 GeV kinematic fit parameters α_k, β_k, and γ_k for each reaction component obtained by Algorithm 3 for both the NI and NO run lists for each HRS and helicity state (as described in Section 3.2.4).

In order to facilitate the overall fit process, a baseline fit of a single run-pair[7] was undertaken at the relevant kinematics for each of the spectrometer arms. That is, a fit was performed on a single set of simultaneous runs taken from each spectrometer arm. These fits were then used by subsequent fitting operations to initialize the placement of each reaction component when performing fits on run lists[8], rather than process each run individually.

Fit Initialization

Three different parameter-constraint algorithms[9] were considered in order to help identify the best way to accomplish the most representative fits to the measured data. The approach taken was to perform the initial fits on the baseline run-pair. In particular, measured spectra were created for each arm that included all valid events (that is, all the ± 1 helicity events). In this way, baseline run-pair fits were obtained that were representative of all events, and which could be used to initialize the individual ± 1 helicity spectra during the fit process.

The parameter-constraint algorithms used were:

1. Algorithm 1: The baseline run-pair fits obtained for the spectra containing all helicity events were then used to fit the individual ± 1 helicity spectra. This was achieved by freezing the model parameters γ_k, α_k, and β_k for all of the reaction components. By doing this, these fits provide new models for fitting the individual helicity spectra. A scaled γ, skewed α, and shifted β version of these frozen fit models was created using (3.10); that is,

$$\hat{H}\,[P_m] = \gamma\; H\,[\,\alpha\,(P_m - \beta)\,]\,. \tag{3.11}$$

   These fits only have three free parameters to accommodate the fitting process,

[7] A run-pair is defined to be data measurements taken from both spectrometer arms during a specified time interval. Those measurements were then stored independently in binary data files that were sequentially and uniquely numbered for each arm. Those files, or runs, that occurred simultaneously in time form run-pairs. For the 2.2 GeV kinematics, runs 3100/22186 (left/right HRS) were selected as the base-line run-pair used to support the fitting process.

[8] A run list is a collection of all "runs" having a specific: kinematic setting, half-wave plate setting, target polarization orientation, and spectrometer arm. This is described in more detail in Section 3.2.4.

[9] The parameter-constraint algorithms focussed on establishing initial parameter values prior to performing the actual fits.

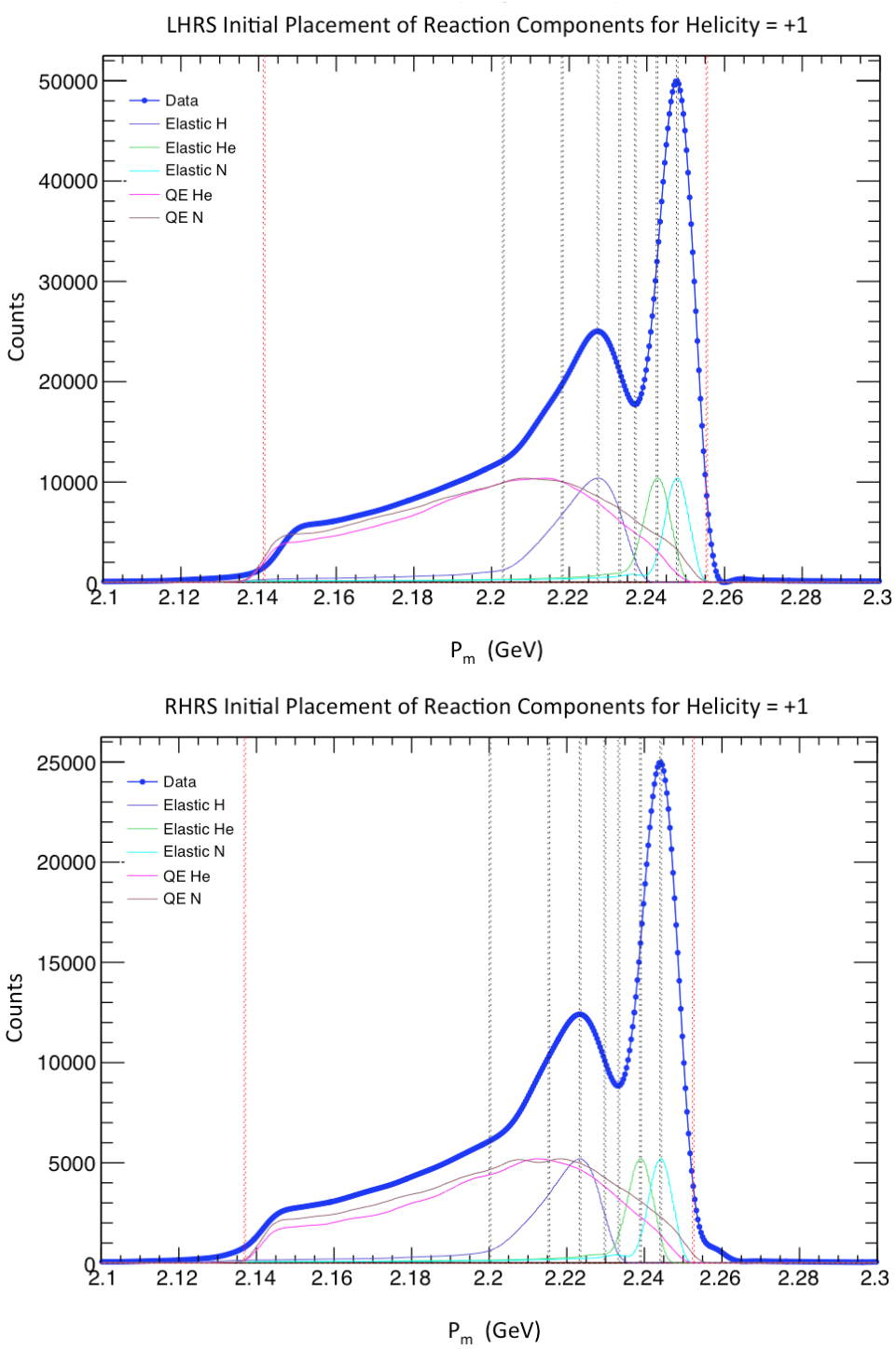

Figure 3.11: These plots illustrate the visual placement of each reaction component using vertical dashed lines (momentum markers) to support the fitting process. Each reaction component is plotted using a different colour. Elastic H, He, and N are respectively plotted as purple, dark green, and cyan. The quasi-elastic He and N show up as magenta and brown. In addition, the blue dots/curve represents the measured data.

and to initialize them, the scale and shift parameters were set to match the maximum peaks of the ± 1 helicity spectra being fitted.

2. Algorithm 2: The baseline run-pair fits obtained for the spectra containing all helicity events were then used to fit the individual ± 1 helicity spectra. This was achieved by independently skewing γ_k, scaling α_k, and shifting β_k their reaction components. These fits have fifteen free parameters to accommodate the fitting process, and to initialize them, the same overall scale and shift factors determined by Algorithm 1 were used to shift and scale each reaction component in this model prior to fitting the helicity spectra.

3. Algorithm 3: This algorithm follows the same process as algorithm 2; however, each reaction component is shifted differently according to $\hat{\beta}_i = \beta + \beta_i/\alpha$. Here the skew factor α is selected slightly different from unity while the shift factor β is selected so that the maximum peaks align as in algorithm 2. The intent was to have a slightly different initialization process in order to check the consistency of the fit solutions between this algorithm and that of algorithm 2. This is a fifteen parameter fit.

The idea behind the fit process described above was that unknowns in the inputs used in the simulations might not produce reaction components that accurately represent the measured histograms (e.g., the physics model for each reaction component may be more or less realistic). The scaling, skewing, and shifting performed by the fit process was designed to account for some of these unknowns. In effect, the fit process allows a degree of flexibility in remodelling the final forms of the simulated reaction components. This relaxes a rigid requirement that the input models be a priori "perfect" descriptions; rather, it provides a flexible method to optimize the models themselves based on comparison to the data.

To verify the fitting process, a number of systematic checks were performed to validate the approach taken. The most obvious check was to shift all of the reaction components as a single unit while allowing them to skew and scale independently resulting in a fit that uses eleven free parameters. It was also reasonable to consider the case when all reaction components are skewed and shifted as a single unit but scaled independently. In this case, the fit process uses seven free parameters. Figure

3.12 shows the overall results obtained for fits that result when using either eleven or seven free parameters during the fitting process for the left arm data.

In the top plot of Figure 3.12, the resultant eleven parameter fit clearly under and over estimates the measured spectrum in numerous regions. In the bottom plot, the seven parameter fit is clearly even worse than the results in the top plot. Given these results, it was clear that neither of these two fit processes were suitable. Consequently, it was decided to focus on the fifteen parameter fit method as the most optimal for the best description of the data. Although Algorithm 1 above is only a three parameter fit, it does incorporate a fit model based on an initial fifteen parameter fit to the spectra having all (both) helicity events. Consequently, all three algorithms described above were assessed here for their ability to generate fits that accurately represent the individual ± 1 helicity spectra.

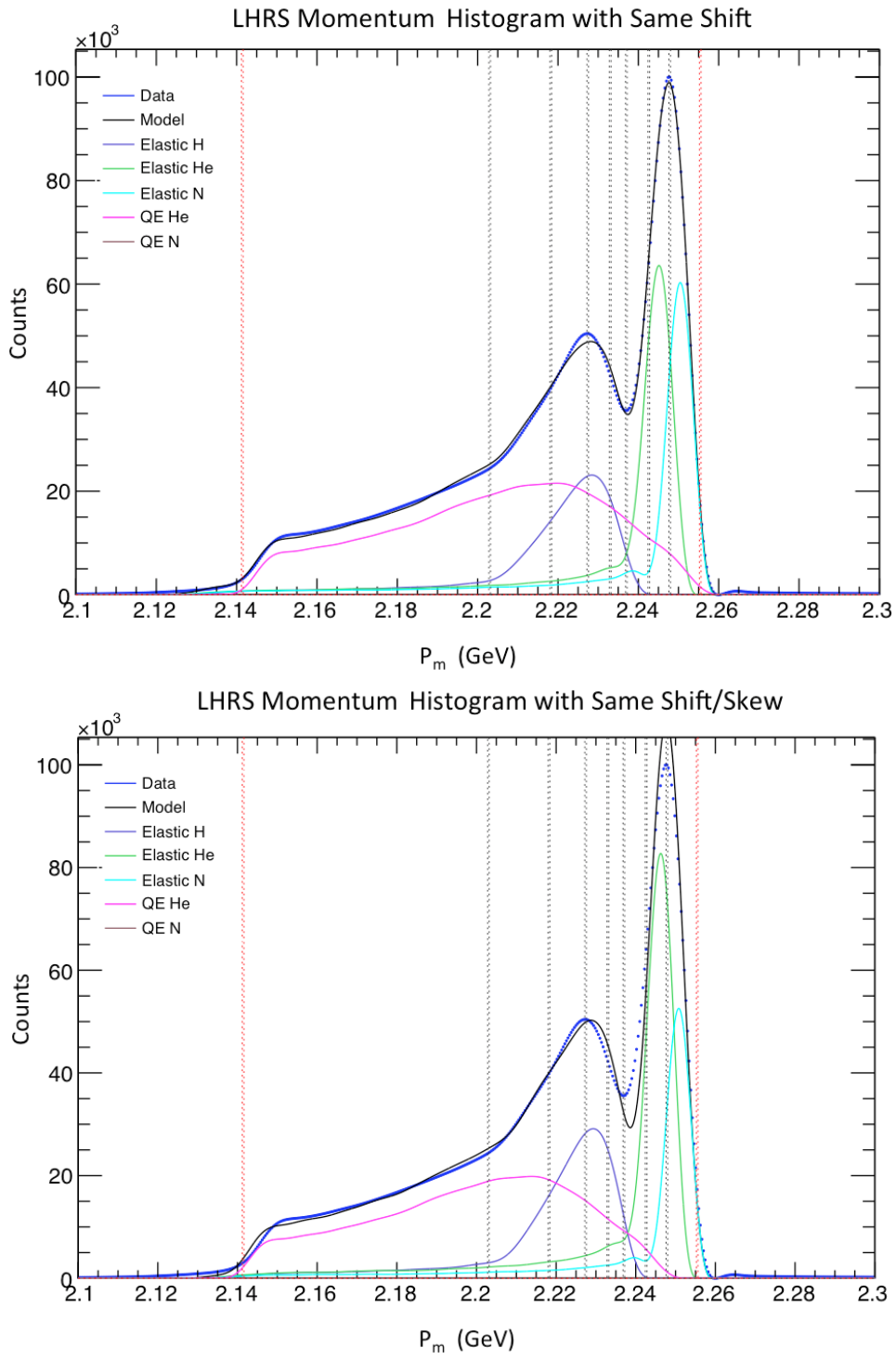

Figure 3.12: LHRS histograms showing the results for eleven and seven parameter fits. The top plot shows the fit results when all reaction components are shifted as a single unit but are free to scale and skew independently when being fit. The bottom plot shows the case when they are skewed and shifted as a single unit but scaled independently of each other. The description in Figure 3.11 provides a legend for the reaction components. The overall fit model is represented by the black curve.

beam energy (GeV)	Q^2 (GeV^2)	A (%)	ΔA_{stat} (%)	ΔA_{sys} (%)
2.2	0.053–0.080	-3.57	0.061	0.142
2.2	0.030–0.053	-2.41	0.044	0.096
1.7	0.036–0.053	-2.73	0.078	0.109
1.7	0.023–0.036	-2.02	0.019	0.081
1.1	0.020–0.030	-1.63	0.083	0.082

Table 3.2: LHRS elastic hydrogen asymmetries for experiment E08-007 reported in Reference [35].

Algorithm Selection

The selection of the best parameter-constraint algorithm to support fitting considered whether or not the resultant fits were representative of the measured spectra, and assessed the physical asymmetries that resulted as a consequence of those fits. It was found that the fits generated using the three choices provided accurate representations of the measured spectra, although the three parameter fit offered by Algorithm 1 had a tendency to slightly over and under fit the data in the regions of the elastic peaks more so than the others. The actual fit results were important only in the sense that they provided estimates of the reaction components in the region of the elastic hydrogen peak suitable for generating consistent and reliable estimates of the hydrogen elastic asymmetry. In order to assess each algorithm, the hydrogen elastic asymmetries associated with the 2.2 GeV baseline run-pair were plotted for the series of cuts used to assess the cut-sensitivity of the asymmetry estimation process. The cuts performed are described later in Section 3.2.6, and the asymmetry results are shown in Figure 3.13.

An analysis of the left arm data for this experiment was completed independent of our analysis approach by the author in Reference [35], M. Friedman. In Friedman's analysis, he extracted the elastic hydrogen physical beam asymmetries for the three kinematics. Those results are provided in Table 3.2. In particular, the results shown in this table for the 2.2 GeV kinematic are seen to be in line with the results plotted in Figure 3.13 for Algorithms 2 and 3. The results generated using these two algorithms are consistent, and essentially the same for their respective arms, across all cuts. However, Algorithm 1 results are not consistent with those reported in Reference [35]. In fact, little variation in these results suggest that three parameter fits are not sufficient for fitting the measurements. Based on these results, and given that there

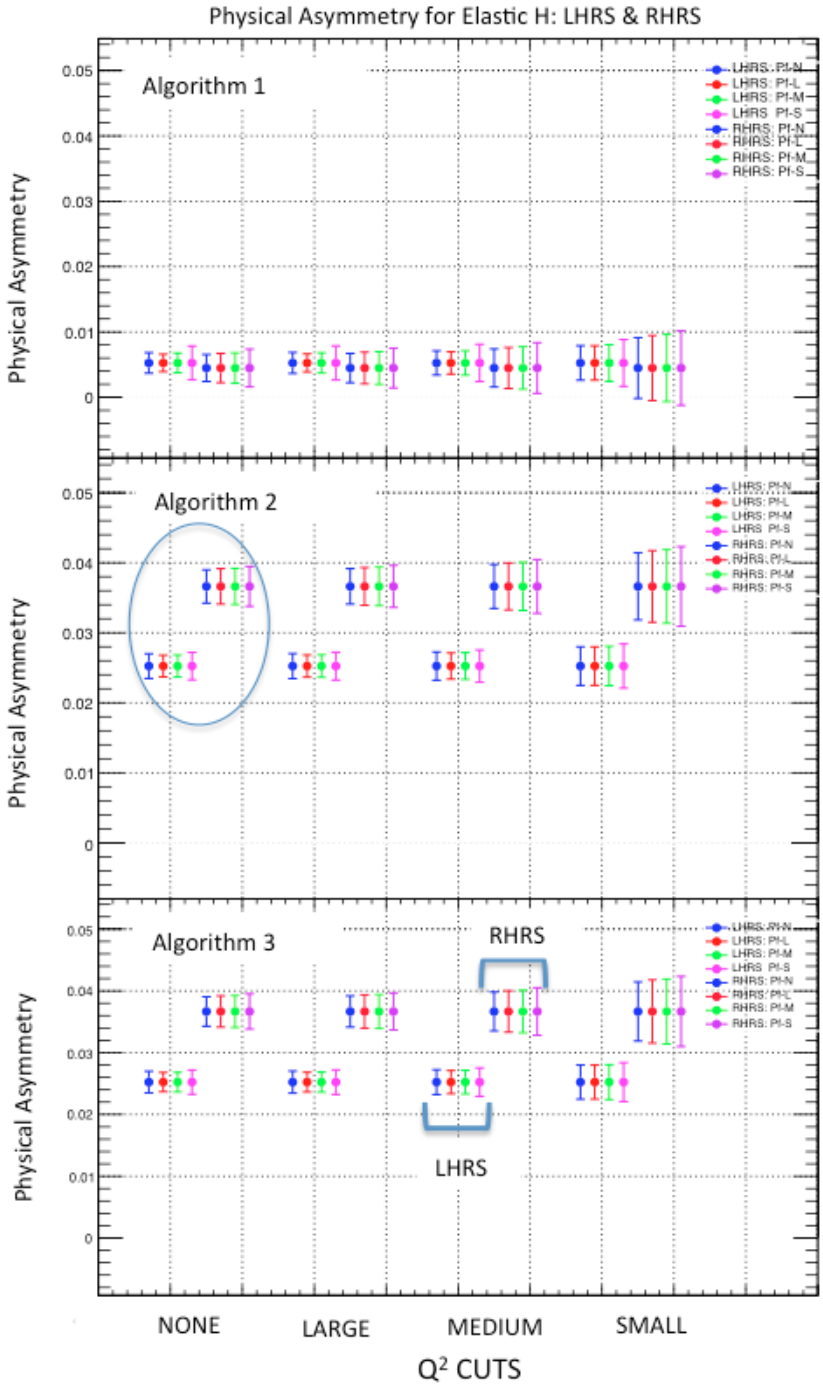

Figure 3.13: The 2.2 GeV baseline run-pair physical asymmetry results for the LHRS and RHRS are plotted for each initialization algorithm. The points encompassed in the blue circle contain two groupings with four entries. The first and second group of four entries represent the LHRS and RHRS asymmetries, respectively. Within one grouping the colours represent the cuts in momentum: None (blue), Large (red), Medium (green), and Small (pink). In addition, each grouping of the LHRS and RHRS results are associated with similar cuts in Q^2 defined along the x-axis of the plot. The definition of these cuts is described in Table 3.9 of Section 3.2.6.

was little difference in the results generated for Algorithms 2 and 3, it was decided that Algorithm 3 would be used in all subsequent analysis of the run lists described in Section 3.2.4 below.

Fit Results

Now that Algorithm 3 has been selected to initialize the fit process, the next step is to provide results that are representative of that process. To that end, the baseline fits discussed above in Section 3.2.3 are provided in Figures 3.14 and 3.15 for the run-pair used to represent the 2.2 GeV measurements. These figures show the fits for both spectrometer arms, and the individual fits associated with the ± 1 helicity measurements. The fitted models are represented by the black curves. Overall, the fitted models provide a realistic representation of the measurements even though some regions appear to have a small degree of mis-modelling[10].

These figures show how each of the individual reaction components are fit to their respective momentum distributions. However, for the RHRS the QE reaction component shown in magenta is stretched in order to fit the extended tail on the right of the distribution past the red vertical line. As a result of this, the fitting process minimizes the brown QE component in order to achieve an excellent overall fit to the data. In order to assess how this affects the overall results of the fitting process, the 2.2 GeV fits for the NI run list (described in the next subsection) are shown in Figures 3.16 and 3.17. The estimated elastic hydrogen components, total backgrounds, and the fitted models are respectively plotted in these figures as purple, magenta, and black curves along with the measurements (data) shown in blue.

The NI results shown in these figures provide an accurate representation of the data; however, the fit process for the RHRS clearly show that the elastic hydrogen and background contributions to the spectra seem to be respectively under and over estimated when compared to the LHRS results. Furthermore, these results are typical for all of the run lists processed, analyzed, and reported herein.

This issue was investigated to see if fits could be generated that mirrored the results shown in the LHRS, with our understanding that the two arms were measuring nearly identical kinematic regimes, and that the LHRS was properly functioning

[10]In the end, for this analysis only the fitting in the region of the hydrogen elastic peak is relevant.

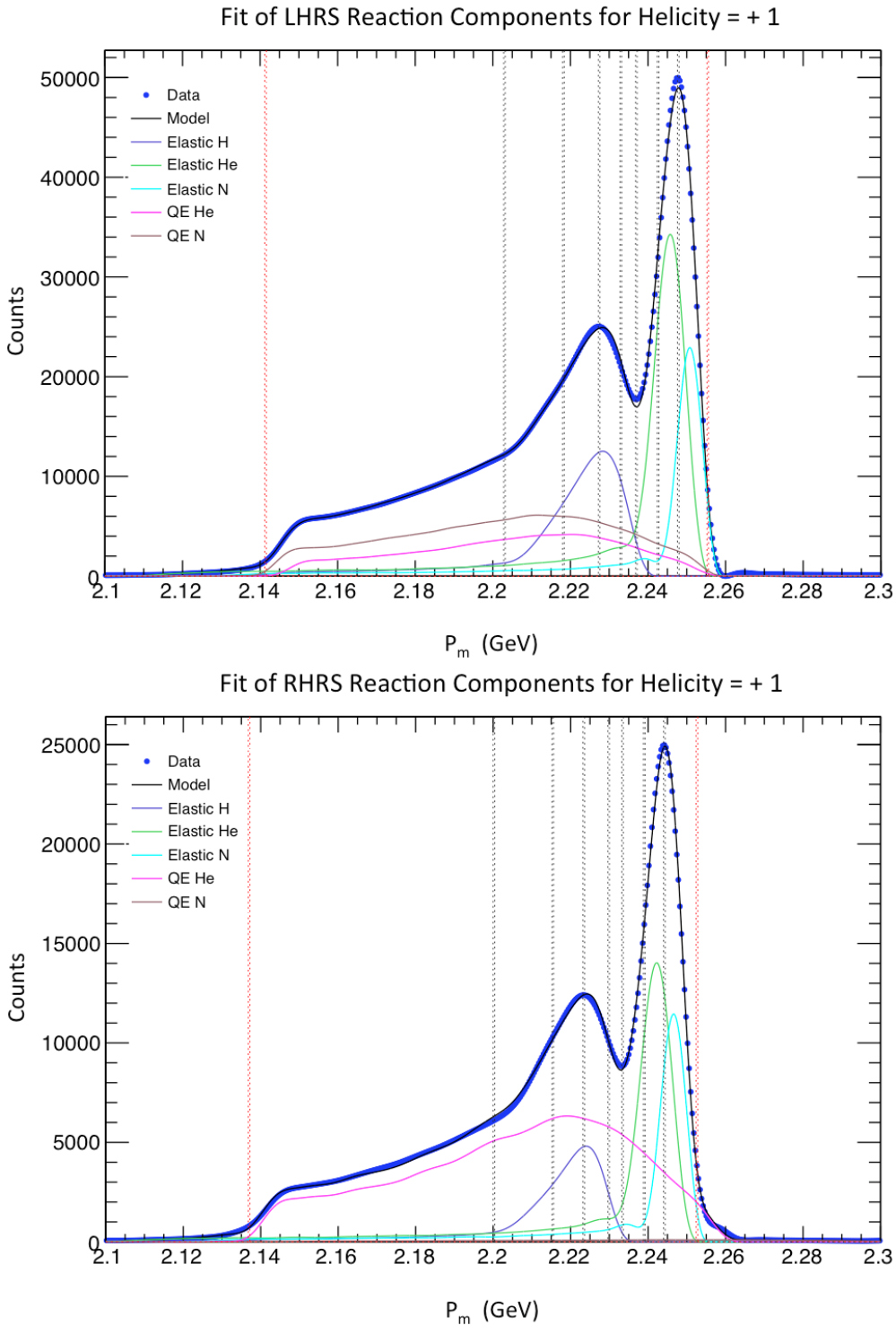

Figure 3.14: The 2.2 GeV baseline run-pair fits for the +1 helicity spectra associated with each arm of the spectrometer. The black curves in the plots represent the fitted model, the blue curve represents the measured data, while the colour of each reaction component is provided in the caption of Figure 3.11.

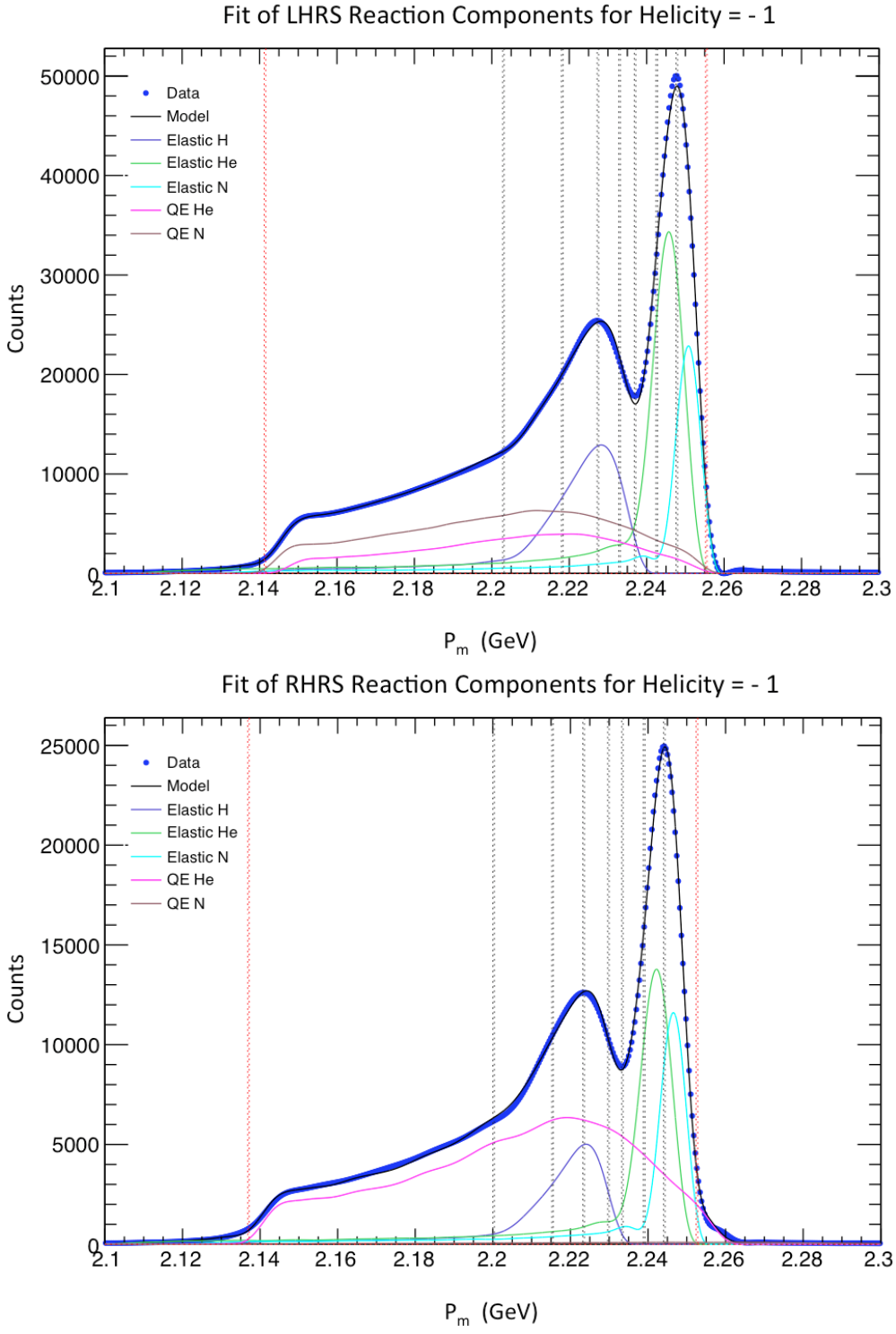

Figure 3.15: The 2.2 GeV baseline run-pair fits for the -1 helicity spectra associated with each arm of the spectrometer. The black curves in the plots represent the fitted model, the blue curve represents the measured data, while the colour of each reaction component is provided in the caption of Figure 3.11.

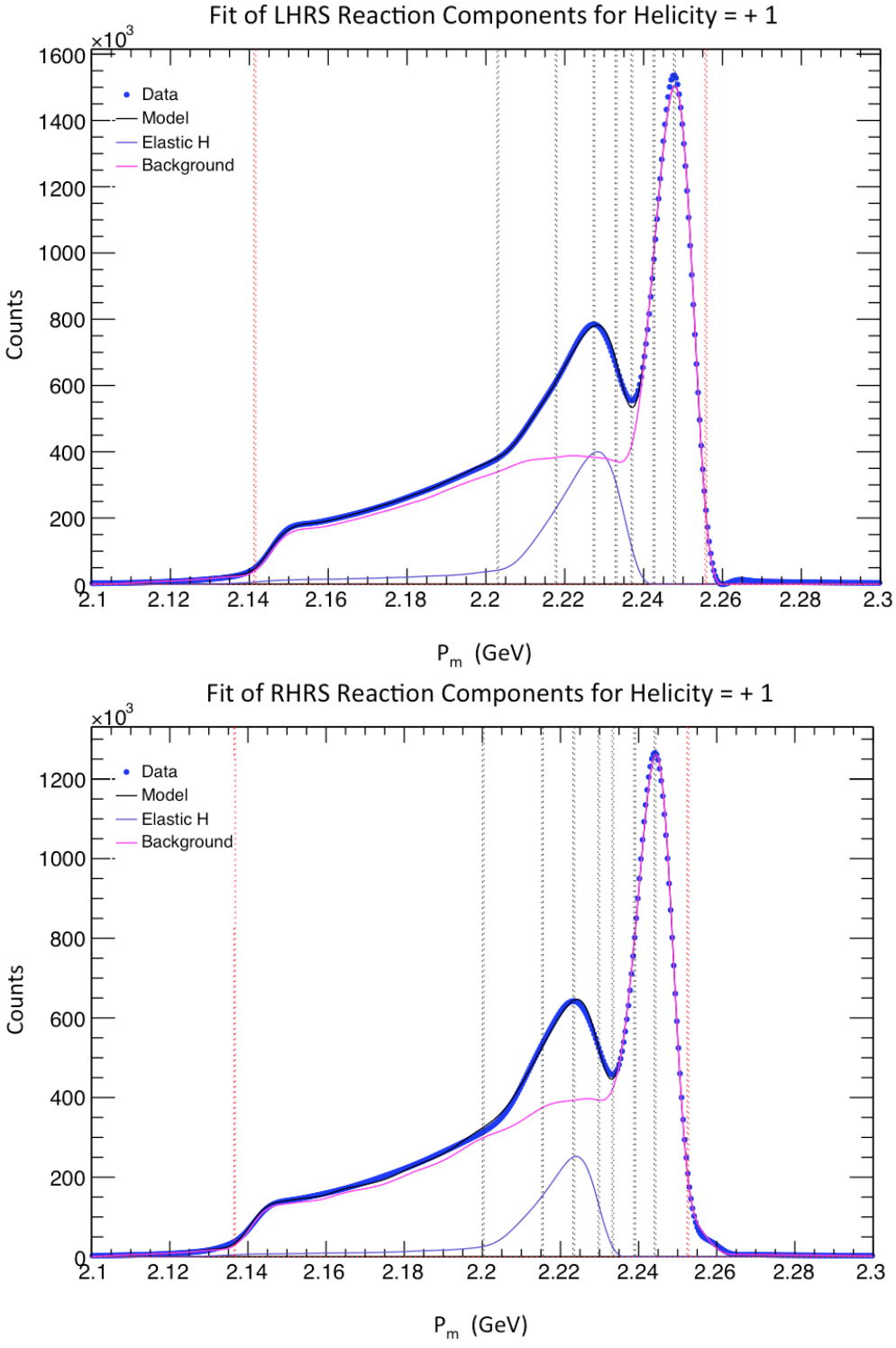

Figure 3.16: The 2.2 GeV fits for the +1 helicity measurements for each arm of the spectrometer for run list NI. The blue curves represent the measured data, the black curves in the plots represent the fitted model while the magenta and purple curves represent the estimated background and elastic hydrogen reaction component associated with each fit, respectively.

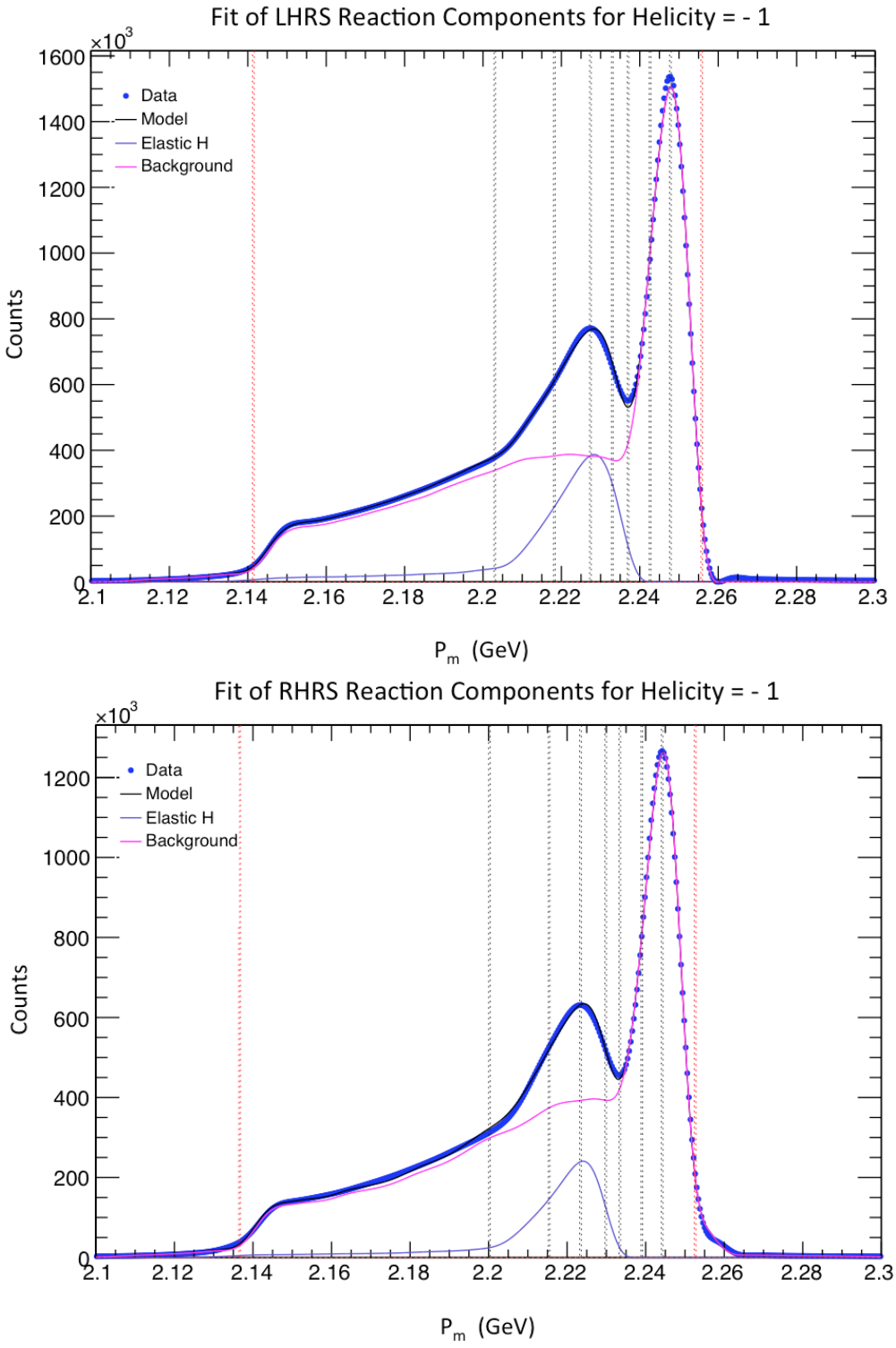

Figure 3.17: The 2.2 GeV fits for the -1 helicity measurements for each arm of the spectrometer for run list NI. The blue curves represent the measured data, the black curves in the plots represent the fitted model while the magenta and purple curves represent the estimated background and elastic hydrogen reaction component associated with each fit, respectively.

Run List	Target Polarization	HWP Status
NI	Negative	In
NO	Negative	Out
PI	Positive	In
PO	Positive	Out
S	Negative	Out

Table 3.3: Convention used for identifying run lists.

throughout the experiment. The LHRS fits showed no suppression of reaction components used to fit anomalous extensions or tails on the right hand side of the spectra. Initially, fits for the RHRS were constrained to the region between the red vertical lines. However, there was little to no change in the subsequent results. Next, the tail on the right hand side of the spectrum was modified to roll-off in a manner similar to that of the LHRS measurements. This did produce fits and placements of reaction components similar to the LHRS results shown in the top plots of Figures 3.14 and 3.15. However, the asymmetries and form factor ratios obtained using this data were problematic (clearly unphysical). Consequently, all run lists were processed using fits without any modifications to the RHRS spectra given that there was no credible rationale to change the prescribed fitting process and their subsequent results.

3.2.4 Run Lists

In order to process groups of runs performed under identical conditions, the runs were organized into a series of run lists. A master list of runs for each kinematic setting and arm of the spectrometer was compiled. This was done by reviewing all of the Hall A electronic logs for experiment E08-007. The information contained in these files was then used to compile the individual run lists. The resultant lists were sorted based upon spectrometer arm, the kinematic setting, whether the half-wave plate HWP was in or out, and the sign of the target polarization. This resulted in twenty-four run lists identified using the first four entries shown in Table 3.3. The process for choosing which runs were included in the individual lists took into account: the run energy, the spectrometer arm, the HWP status, the target polarization was at least 40% and its signage, the target type had to be NH_3, the run was designated a production run and that it actually contained events, and that the logs did not identify any major

issues with the run being considered.

When these run lists were processed, the convention shown in this table was used to identify the subsequent results being reported. This table also contains an additional identifier S, which refers to the single run-pair used as the baseline fits in the fit process described above.

3.2.5 Uncertainty Analysis

The approach taken here to estimate uncertainty values follows the standard differential analysis process [86]. This includes all uncertainty estimates whether they were generated using measurements or derived from mathematical expressions.

Target and Beam Polarization

All measurement variables usually have uncertainty estimates, and where appropriate, they were combined using the standard differential analysis methodology [86]. For example, the choice to process lists of runs for each arm of the spectrometer required that the individual values of the target polarization be combined to produce a single result for each run list. This was accomplished by performing a narrow cut in the measured momentum around the elastic hydrogen peak in order to determine the number of events for each run[11]. These data, and the individual run target polarization values, were then used to produce a weighted average[12] of the target polarization for each run list. A differential uncertainty analysis of this averaging process was then used to combine the uncertainties for each run in order to generate the uncertainty for that run list.

For the beam polarization data, Møller measurements were conducted for experiments E08-027 and E08-007, from February 16 through May 17, 2012. The individual values used for the run lists were selected based upon the dates associated with the runs contained in the list. An average value was then generated and used in the subsequent asymmetry calculations.

Table 3.4 provides the target and beam polarization used to generate asymmetry and form factor ratios for the 2.2 GeV series of runs. This table also lists the number

[11]The number of events measured in the momentum cut provided an estimate (or, a proxy) for the total charge required for generating a weighted target polarization result for each run list.

[12]The target polarization is weighted with respect to charge.

List	LHRS			RHRS		
	Runs	P_t	P_b	Runs	P_t	P_b
NI	34	-0.7625 ± 0.0044	-0.8008 ± 0.0083	35	-0.7806 ± 0.0047	-0.8008 ± 0.0083
NO	20	-0.7528 ± 0.0056	0.8008 ± 0.0083	22	-0.7721 ± 0.0059	0.8008 ± 0.0083
PI	4	0.6726 ± 0.0090	-0.8008 ± 0.0083	4	0.6173 ± 0.0110	-0.8008 ± 0.0083
PO	6	0.5641 ± 0.0076	0.8008 ± 0.0083	7	0.5608 ± 0.0071	0.8008 ± 0.0083
S	1	-0.8520 ± 0.0260	0.8008 ± 0.0083	1	-0.8543 ± 0.0260	0.8008 ± 0.0083

Table 3.4: Target and beam polarization data for each run list processed for the 2.2 GeV series of runs.

of runs contained in each of the lists using the convention shown in Table 3.3.

Asymmetry

The fit process provides estimates of the elastic hydrogen "reaction components" that can then be used to perform asymmetry calculations. Note that this method utilizes these best-fits to the hydrogen elastic component to become the proxy for the actual data in the remaining part of the analysis process. This is because the problems with the RHRS prevented any ability to reliably perform kinematic interpretation beyond the momentum spectrum, and therefore the now properly scaled hydrogen elastic fit results can be fully utilized in replacement of the data to make kinematic cuts, and determine the helicity asymmetries.

The number of events in the fitted hydrogen elastic components are represented by $N^{\pm}$, where the counts for a specific helicity state are indicated by the noted superscript. The raw asymmetry was then calculated using:

$$A_{raw} = \frac{N^+ - N^-}{N^+ + N^-} \,. \tag{3.12}$$

and its uncertainty was expressed as

$$\Delta A_{raw} = \left[\frac{2N^+N^-}{(N^+ + N^-)^2}\right] \sqrt{\left[\frac{\Delta N^+}{N^+}\right]^2 + \left[\frac{\Delta N^-}{N^-}\right]^2} \tag{3.13}$$

The relative terms $\left[\frac{\Delta N^+}{N^+}\right]$ and $\left[\frac{\Delta N^-}{N^-}\right]$ in (3.13) contain two types of uncertainty. The first being statistical based upon the fit to the number of raw counts, while the other is the uncertainty associated with the model fitting process. This second model uncertainty provides a direct comparison between how well the fitted model represents the measurements. The relative model uncertainty $M^{\pm}_{rel}$ for each of the

helicity histograms was defined in the following manner:

$$\Delta M_{rel}^{\pm} = \frac{|data^{\pm} - model^{\pm}|}{data^{\pm}} \tag{3.14}$$

where $data^{\pm}$ and $model^{\pm}$ represent respectively the helicity states associated with the measurement and model spectra, where this comparison is done between the full fit (sum of the reaction components) and the data. The statistical and model uncertainties were then added in quadrature as relative quantities to arrive at a total uncertainty in the number of counts for each of the helicity states. That is,

$$\left[\frac{\Delta N^{\pm}}{N^{\pm}}\right]^2_{Total} = \left[\frac{\sqrt{N^{\pm}}}{N^{\pm}}\right]^2_{Statistical} + \left[\Delta M_{rel}^{\pm}\right]^2_{Model} \tag{3.15}$$

These total relative uncertainties were then substituted into their respective terms in (3.13). This then provides an uncertainty estimate for the raw asymmetry that accounts for both statistical uncertainty and an estimate of the systematic uncertainty associated with the modelling errors. The physical asymmetry is then obtained by dividing the raw hydrogen elastic component asymmetry by the their respective target and beam polarizations, i.e., $A_{phys} = A_{raw}/P_T\,P_B$. The uncertainty in A_{phys} due to the target and beam polarizations are then incorporated using the standard differential uncertainty analysis approach.

Form Factor Ratio

Equations 1.61 and 1.62 express the form factor ratios (FFR) in terms of their kinematic variables for DSA (FFR_{DSA}) and the single arm (FFR_{SA}) calculations, respectively. It is clear that these expressions can be written in the following form to expressly show their dependent variables:

$$\left.\begin{array}{rcl} FFR_{_{DSA}} & = & FFR_{_{DSA}}\,[\,\mu_p,\,\tau,\,\theta_1,\,\theta_1^*,\,\phi_1^*,\,\theta_2,\,\theta_2^*,\,\phi_2^*,\,\Gamma_{12}\,] \\ FFR_{_{SA}} & = & FFR_{_{SA}}\,[\,\mu_p,\,\tau,\,\theta,\,\theta^*,\,\phi^*,\,A_p\,] \\ \Gamma_{12} & = & \frac{A_{r1}}{A_{r2}} \\ \tau & = & \tau\,[\,Q^2,\,M_p\,] \end{array}\right\} \tag{3.16}$$

where Γ_{12} is the ratio of the raw asymmetries respectively for the right and left spectrometer arms as denoted by their subscripts. The subscripts on the FFR functions indicate that they are either for the DSA or single arm calculations. The uncertainties

associated with these expressions were derived via direct application of the standard differential uncertainty analysis technique discussed above. The resulting expressions were then used to calculate the uncertainties using the kinematic variables associated with the elastic hydrogen events estimated via simulation and the fitting process.

Kinematic Variables

The best fit simulation of the hydrogen elastic scattering process produced by g2psim provides a sufficient framework to calculate the kinematic variables required to support the overall analysis. On an event-by-event basis in the simulation, the kinematic variables Q^2, θ, θ^*, and ϕ^* are generated for each arm and kinematic setting, along with error estimates $\Delta\theta^*[\vec{S}]$ and $\Delta\phi^*[\vec{S}]$ for the uncertainties in the target polarization orientation $\vec{S}$. In the analysis, histograms of these kinematic variables are used to provide estimates and uncertainties suitable for calculating the single arm and DSA form factor ratios[13]. The variable τ and its uncertainty is calculated using $\tau = Q^2/4M_p^2$. The error estimates for θ^* and ϕ^* due to the orientation of $\vec{S}$ are produced using the standard differential uncertainty analysis based on the mathematical relationship between these variables and $\vec{S}$ [14]. The resulting estimates were then added in quadrature with the standard uncertainties obtained via the histograms for these variables.

Example form factor ratio calculations using these kinematic variables are provided in Tables 3.5, 3.6, and 3.7. The first two tables show single arm calculations respectively for the 2.2 GeV kinematic for the NI run list for the LHRS and RHRS. These results were obtained using a medium momentum cut, as described in Section 3.2.6. The third table shows the corresponding DSA results for the same conditions.

[13]Histograms of the kinematic variables provide means and standard deviations. The means are used to estimate the variables while their standard deviations σ_{std} determine associated uncertainties using equation $\sigma_u = \sigma_{std}/\sqrt{N}$ for a histogram containing N events [86].

[14]Vector $\vec{S}$ has a orientation defined by angles $\theta_{\vec{S}}$ and $\phi_{\vec{S}}$; therefore, it is a function of these variables. Equation 3.5 defines θ^* and ϕ^* in terms of $\vec{S}$; therefore, these angles are also functions of $\theta_{\vec{S}}$ and $\phi_{\vec{S}}$. As a result, uncertainties in $\theta_{\vec{S}}$ and $\phi_{\vec{S}}$ can be accounted for in the angles θ^* and ϕ^* using standard differential uncertainty analysis [86].

Variable	Value and Error	Units
μ	$2.793 \pm 8.5\times10^{-13}$	μ_N
M_p	$0.938 \pm 5.8\times10^{-13}$	GeV
Q^2	$0.051 \pm 2.3\times10^{-5}$	GeV^2
τ	$0.015 \pm 6.6\times10^{-6}$	-
θ_2	$0.103 \pm 3.3\times10^{-5}$	rad
θ_2^*	$1.645 \pm 4.8\times10^{-4}$	rad
ϕ_2^*	$3.140 \pm 1.5\times10^{-4}$	rad
A_2	$0.029 \pm 4.9\times10^{-4}$	-
FFR	1.142 ± 0.023	μ_N

Table 3.5: Single arm FFR results for the LHRS and the 2.2 GeV NI run list. Values for μ and M_p are obtained from Reference [87].

Variable	Value and Error	Units
μ	$2.793 \pm 8.5\times10^{-13}$	μ_N
M_p	$0.938 \pm 5.8\times10^{-13}$	GeV
Q^2	$0.051 \pm 2.3\times10^{-5}$	GeV^2
τ	$0.015 \pm 6.6\times10^{-6}$	-
θ_1	$0.098 \pm 3.3\times10^{-5}$	rad
θ_1^*	$1.833 \pm 4.8\times10^{-4}$	rad
ϕ_1^*	$3.163 \pm 1.5\times10^{-4}$	rad
A_1	$0.038 \pm 8.2\times10^{-4}$	-
FFR	0.802 ± 0.022	μ_N

Table 3.6: Single arm FFR Results for the RHRS and the 2.2 GeV NI run list. Values for μ and M_p are obtained from Reference [87].

Variable	Value and Error	Units
μ	$2.793 \pm 8.5\times10^{-13}$	μ_N
M_p	$0.938 \pm 5.8\times10^{-13}$	GeV
Q^2	$0.051 \pm 2.3\times10^{-5}$	GeV^2
τ	$0.015 \pm 6.6\times10^{-6}$	-
θ_1	$0.098 \pm 3.3\times10^{-5}$	rad
θ_2	$0.103 \pm 3.3\times10^{-5}$	rad
θ_1^*	$1.833 \pm 4.8\times10^{-4}$	rad
θ_2^*	$1.645 \pm 4.8\times10^{-4}$	rad
ϕ_1^*	$3.163 \pm 1.5\times10^{-4}$	rad
ϕ_2^*	$3.140 \pm 1.5\times10^{-4}$	rad
A_1	$0.024 \pm 4.3\times10^{-4}$	-
A_2	$0.018 \pm 2.2\times10^{-4}$	-
A_1/A_2	$1.357 \pm 2.9\times10^{-2}$	-
FFR	0.138 ± 0.012	μ_N

Table 3.7: DSA FFR Results where RHRS and LHRS are denoted by subscripts 1 and 2, respectively. This is for the 2.2 GeV NI run list. Values for μ and M_p are obtained from Reference [87].

Energy [GeV]	Lower Momentum Cut [GeV]	Upper Momentum Cut [GeV]
2.2	2.10	2.30
1.7	1.60	1.74
1.1	1.08	1.18

Table 3.8: The initial focal plane momentum cuts for each of the kinematic settings.

3.2.6 Measurement Cuts

The conventional approach to processing spectrometer measurements requires a proper selection of cuts in order to ensure that the selection process correctly captures the targeted scattering events for further analysis. For experiment E08-007, the primary events of interest were the elastic hydrogen events. To achieve this, as was previously outlined, an initial momentum range was selected for each kinematic setting in order to generate focal plane spectra suitable for fitting. These initial cuts are provided in Table 3.8 for each kinematic setting.

In addition to making these initial cuts to create spectra for fitting, it was also important to assess the sensitivity of the asymmetry estimation process—that is, to understand how the asymmetry changes when normal cuts are applied to the elastic hydrogen reaction component that were estimated during the fitting process. Typically, further cuts in the measured momentum P_m and in other relevant kinematic variables such as Q^2 are performed. In the end, cut sensitivity was assessed by performing four cuts in both P_m and Q^2.

These cuts were performed using a data centric approach that perform symmetric cuts using each variable's mean and standard deviation. The algorithm creates cuts in both P_m and Q^2 by using their distributions to define a range as a percentage of a two standard deviation spread about their means. Table 3.9 describes these cuts while Figures 3.18 and 3.19 provide an illustration of the generated results.

Cuts	Defined in terms of the variable's mean and standard deviation
None	Includes all events no cuts
Large	Includes 85% of the events in the 2σ range about the mean
Medium	Includes 50% of the events in the 2σ range about the mean
Small	Includes 20% of the events in the 2σ range about the mean

Table 3.9: P_m and Q^2 cuts algorithm used to investigate the cut-sensitivity of the extracted hydrogen elastic asymmetry.

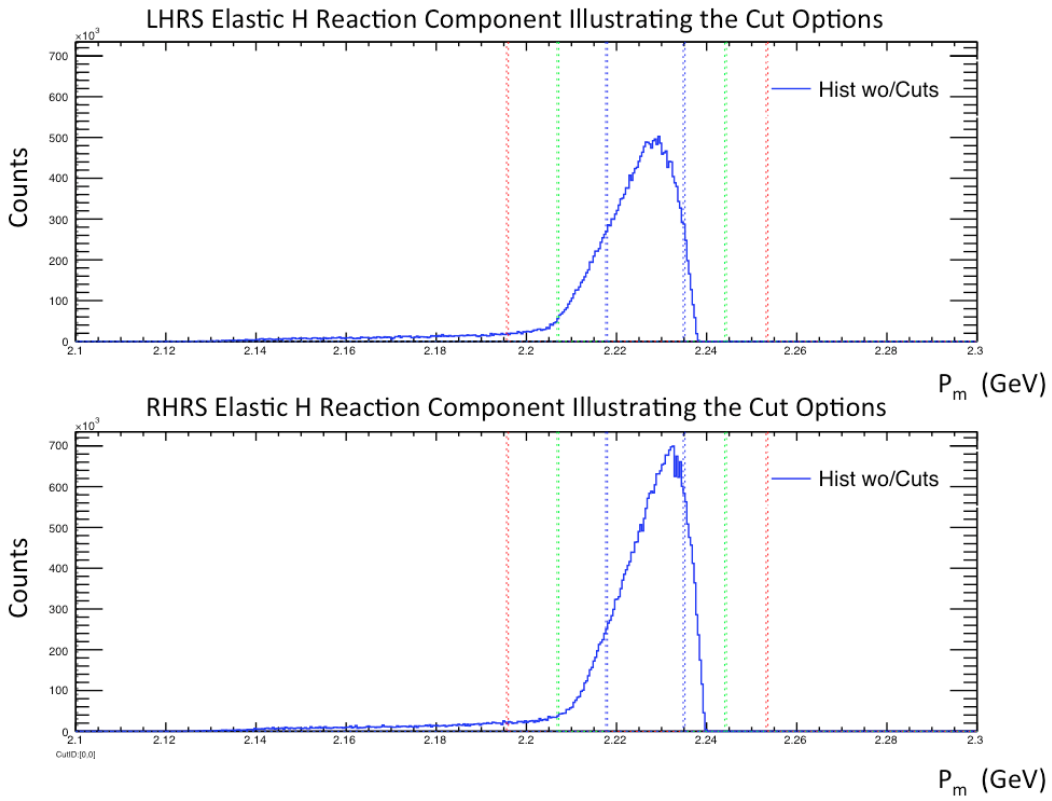

Figure 3.18: This figure shows the cuts made in P_m for the left and right arms of the spectrometer. These cuts are identified as being None, Large, Medium, and Small delineated respectively by vertical lines that are black, red, green, and blue. The horizontal axis units are in GeV for P_m. These plots are for the 2.2 GeV NI run list.

Tables 3.10 through 3.17 provide the 2.2 GeV physical hydrogen elastic asymmetry results for both spectrometers, and for each run list identified in Table 3.3. The results shown are for all cut combinations in P_m and Q^2 using Algorithm 3 applied to the fitted elastic hydrogen reaction component. What stands out in these tables is the fact that the results are consistent for all cuts with only their uncertainties showing any growth due to the increased degree of cuts performed. Given these results, the question to be answered was: what is the optimal selection of cuts in P_m and Q^2 for best estimating the hydrogen elastic asymmetry from each run list?

In order to answer this question, there are two factors that need to be considered. Firstly, Reference [35] has processed the left spectrometer data generating estimates of physical asymmetry for the elastic hydrogen component using the normal/standard Hall A reconstruction process. As such, those data can be used to perform a direct comparison with results obtained here, even though there are differences in how these

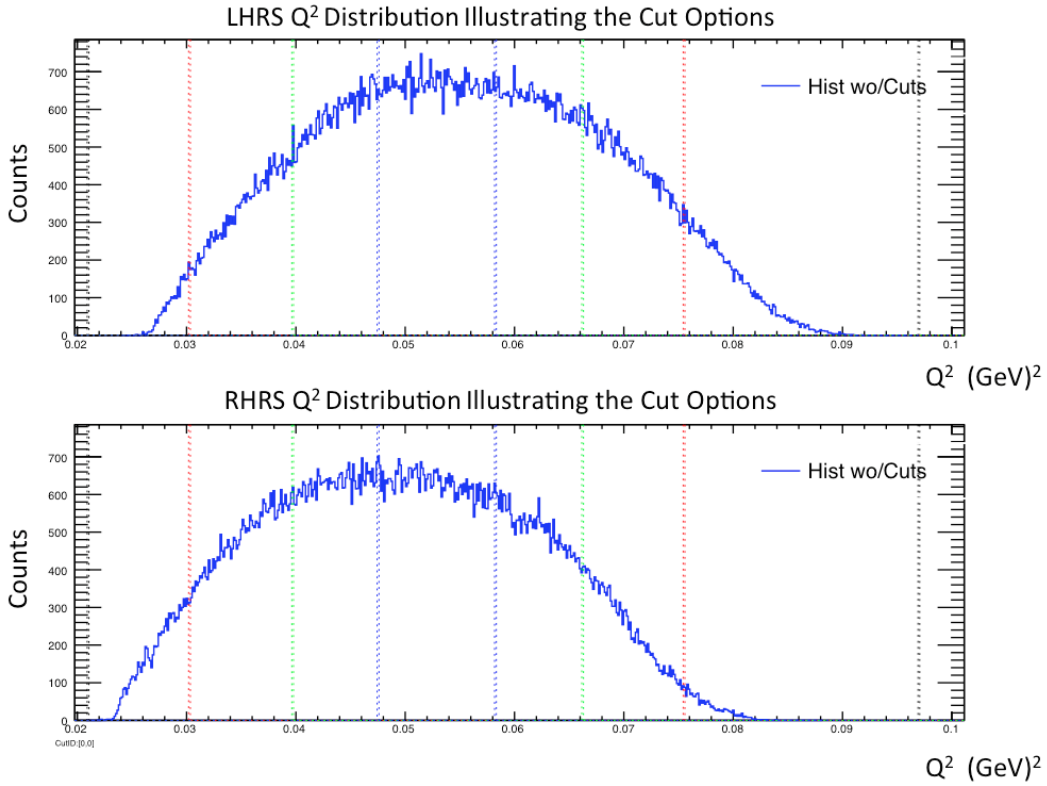

Figure 3.19: This figure shows the cuts made in Q^2 for the left and right arms of the spectrometer. These cuts are identified as being None, Large, Medium, and Small delineated respectively by vertical lines that are black, red, green, and blue. The horizontal axis units are in GeV^2 for Q^2. These plots are for the 2.2 GeV NI run list.

results were generated. For example, the author of that report uses a beam polarization of 89% for all calculations, and processes each run individually before producing an average result for each kinematic. Furthermore, a dilution factor of $f = 0.75 \pm 0.25$ was used, which our analysis accounts for implicitly by the nature of "fitting out" the background contributions. The physical asymmetries reported in [35] are provided in Table 3.2, and were for two different Q^2 regions on either side of the central kinematics value of Q^2 shown in Table 2.1.

A_{phys} ($\times 10^{-2}$)		Q^2			
		None	Large	Medium	Small
P_m	None	2.869 ± 0.140	2.869 ± 0.140	2.869 ± 0.140	2.869 ± 0.140
	Large	2.869 ± 0.049	2.869 ± 0.049	2.869 ± 0.053	2.869 ± 0.067
	Medium	2.869 ± 0.049	2.869 ± 0.049	2.869 ± 0.054	2.869 ± 0.068
	Small	2.869 ± 0.077	2.869 ± 0.077	2.869 ± 0.081	2.869 ± 0.091

Table 3.10: Physical asymmetry results obtained for the cuts made in Q^2 and P_m on the LHRS Elastic Hydrogen reaction component for Algorithm 3 and run list NI, for the 2.2 GeV setting.

A_{phys} ($\times 10^{-2}$)		Q^2			
		None	Large	Medium	Small
P_m	None	3.803 ± 0.060	3.803 ± 0.061	3.803 ± 0.067	3.803 ± 0.087
	Large	3.803 ± 0.084	3.803 ± 0.085	3.803 ± 0.091	3.803 ± 0.110
	Medium	3.803 ± 0.082	3.803 ± 0.083	3.803 ± 0.089	3.803 ± 0.110
	Small	3.803 ± 0.076	3.803 ± 0.077	3.803 ± 0.086	3.803 ± 0.110

Table 3.11: Physical asymmetry results obtained for the cuts made in Q^2 and P_m on the RHRS Elastic Hydrogen reaction component for Algorithm 3 and run list NI, for the 2.2 GeV setting.

A_{phys} ($\times 10^{-2}$)		Q^2			
		None	Large	Medium	Small
P_m	None	2.851 ± 0.120	2.851 ± 0.120	2.851 ± 0.130	2.851 ± 0.130
	Large	2.851 ± 0.056	2.851 ± 0.057	2.851 ± 0.063	2.851 ± 0.081
	Medium	2.851 ± 0.053	2.851 ± 0.054	2.851 ± 0.060	2.851 ± 0.080
	Small	2.851 ± 0.099	2.851 ± 0.099	2.851 ± 0.100	2.851 ± 0.120

Table 3.12: Physical asymmetry results obtained for the cuts made in Q^2 and P_m on the LHRS Elastic Hydrogen reaction component for Algorithm 3 and run list NO, for the 2.2 GeV setting.

A_{phys} ($\times 10^{-2}$)		Q^2			
		None	Large	Medium	Small
P_m	None	3.597 ± 0.065	3.597 ± 0.067	3.597 ± 0.076	3.597 ± 0.100
	Large	3.597 ± 0.084	3.597 ± 0.086	3.597 ± 0.090	3.597 ± 0.120
	Medium	3.597 ± 0.088	3.597 ± 0.090	3.597 ± 0.098	3.597 ± 0.120
	Small	3.597 ± 0.084	3.597 ± 0.086	3.597 ± 0.097	3.597 ± 0.120

Table 3.13: Physical asymmetry results obtained for the cuts made in Q^2 and P_m on the RHRS Elastic Hydrogen reaction component for Algorithm 3 and run list NO, for the 2.2 GeV setting.

A_{phys} ($\times 10^{-2}$)		Q^2			
		None	Large	Medium	Small
P_m	None	3.007 ± 0.110	3.007 ± 0.110	3.007 ± 0.130	3.007 ± 0.200
	Large	3.007 ± 0.170	3.007 ± 0.170	3.007 ± 0.180	3.007 ± 0.240
	Medium	3.007 ± 0.130	3.007 ± 0.140	3.007 ± 0.160	3.007 ± 0.220
	Small	3.007 ± 0.130	3.007 ± 0.140	3.007 ± 0.160	3.007 ± 0.230

Table 3.14: Physical asymmetry results obtained for the cuts made in Q^2 and P_m on the LHRS Elastic Hydrogen reaction component for Algorithm 3 and run list PI, for the 2.2 GeV setting.

A_{phys} ($\times 10^{-2}$)		Q^2			
		None	Large	Medium	Small
P_m	None	3.302 ± 0.150	3.302 ± 0.160	3.302 ± 0.200	3.302 ± 0.300
	Large	3.302 ± 0.170	3.302 ± 0.180	3.302 ± 0.200	3.302 ± 0.330
	Medium	3.302 ± 0.160	3.302 ± 0.170	3.302 ± 0.200	3.302 ± 0.330
	Small	3.302 ± 0.210	3.302 ± 0.210	3.302 ± 0.260	3.302 ± 0.370

Table 3.15: Physical asymmetry results obtained for the cuts made in Q^2 and P_m on the RHRS Elastic Hydrogen reaction component for Algorithm 3 and run list PI, for the 2.2 GeV setting.

A_{phys} ($\times 10^{-2}$)		Q^2			
		None	Large	Medium	Small
P_m	None	2.754 ± 0.910	2.754 ± 0.093	2.754 ± 0.110	2.754 ± 0.160
	Large	2.754 ± 0.110	2.754 ± 0.110	2.754 ± 0.130	2.754 ± 0.180
	Medium	2.754 ± 0.190	2.754 ± 0.190	2.754 ± 0.200	2.754 ± 0.240
	Small	2.754 ± 0.170	2.754 ± 0.170	2.754 ± 0.190	2.754 ± 0.230

Table 3.16: Physical asymmetry results obtained for the cuts made in Q^2 and P_m on the LHRS Elastic Hydrogen reaction component for Algorithm 3 and run list PO, for the 2.2 GeV setting.

A_{phys} ($\times 10^{-2}$)		Q^2			
		None	Large	Medium	Small
P_m	None	3.703 ± 0.140	3.703 ± 0.150	3.703 ± 0.190	3.703 ± 0.290
	Large	3.703 ± 0.180	3.703 ± 0.190	3.703 ± 0.220	3.703 ± 0.330
	Medium	3.703 ± 0.150	3.703 ± 0.160	3.703 ± 0.210	3.703 ± 0.320
	Small	3.703 ± 0.200	3.703 ± 0.210	3.703 ± 0.250	3.703 ± 0.360

Table 3.17: Physical asymmetry results obtained for the cuts made in Q^2 and P_m on the RHRS Elastic Hydrogen reaction component for Algorithm 3 and run list PO, for the 2.2 GeV setting.

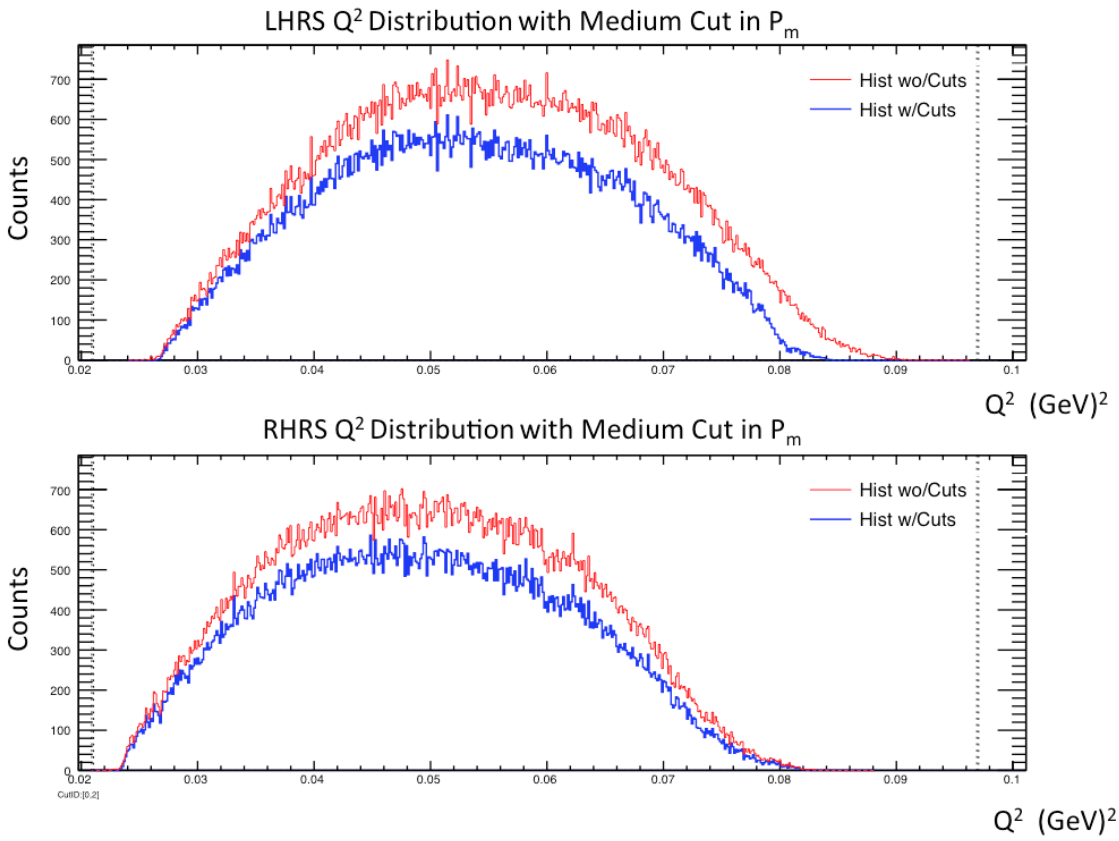

Figure 3.20: The LHRS and RHRS Q^2 simulated distributions for the elastic hydrogen events using a medium cut in P_m. The distribution having no cuts is indicated in red while the one in blue shows the effect of the cut for the 2.2 GeV setting.

The other factor to consider was that the standard reconstruction process cannot be performed on the right arm of the spectrometer. Thus, kinematic variables (like Q^2) cannot be determined directly from measured data and therefore cuts cannot be made on the data itself. In fact, as stated previously, the only quantity reliably available from the RHRS data is the measured momentum detected by the spectrometer. It was therefore important to assess how cuts in P_m affect the simulated distributions of Q^2 in the approach taken here. To this end, Figure 3.20 shows the simulated Q^2 distributions for both spectrometers for the elastic hydrogen events as a result of only using a medium cut in P_m. The distributions in this figure are largely confined to the overall cut range utilized in Reference [35], i.e., $0.030 \leq Q^2 \leq 0.080$ GeV^2. As such, this should allow us to perform a relative comparison of results.

Given these factors, it was decided to analyze the data using only medium cuts in

P_m. Furthermore, the plots in Figure 3.20 clearly show that the medium cut covers the most significant portion of the simulated elastic hydrogen distributions. Thus, this should ensure that an accurate representation of these distributions remains to support asymmetry calculations that have a range of Q^2 similar to what was used in Reference [35].

3.2.7 Asymmetries

As previously indicated, the LHRS measurements from experiment E08-007 were previously analyzed and reported in Reference [35]. Those results, shown in Table 3.2, provide estimates of the proton physical asymmetry for lower and upper cut regions of Q^2 for each kinematic setting. The 2.2 GeV results shown in this table are used here as a basis of comparison for the fit-based results generated for the five 2.2 GeV run lists shown in Table 3.3. The physical and raw asymmetries extracted via the fit process are provided in Tables 3.18 and 3.19.

Figure 3.21 shows the physical asymmetry measurements extracted for each run list. For each spectrometer arm, this figure shows an average asymmetry indicated by the coloured dashed lines. In Figure 3.22, these results are plotted along side the asymmetries obtained for the lower and upper Q^2 cut regions from Reference [35]. The mean physical asymmetries extracted for the LHRS are found to lie between the two results in Reference [35] while the RHRS values are somewhat higher. Given that the medium Q^2 cut covers both ranges used in [35], suggests that the extracted results for the LHRS are in fact reasonable and in agreement with those results.

Energy (GeV)	HRS	Run List	A_{phys} ($\times 10^{-2}$)	$\Delta A_{sys+stat}$ ($\times 10^{-2}$)
2.2	LHRS	NI	2.866	0.049
2.2		NO	2.851	0.053
2.2		PI	3.010	0.130
2.2		PO	2.750	0.190
2.2		S	2.520	0.160
2.2	RHRS	NI	3.800	0.082
2.2		NO	3.597	0.088
2.2		PI	3.300	0.160
2.2		PO	3.700	0.150
2.2		S	3.670	0.260

Table 3.18: The 2.2 GeV physical proton elastic asymmetries extracted via the fit process.

Energy (GeV)	HRS	Run List	A_{raw} ($\times 10^{-2}$)	$\Delta A_{sys+stat}$ ($\times 10^{-2}$)
2.2	LHRS	NI	1.752	0.022
2.2		NO	- 1.719	0.023
2.2		PI	- 1.619	0.066
2.2		PO	1.244	0.083
2.2		S	- 1.722	0.092
2.2	RHRS	NI	2.377	0.043
2.2		NO	- 2.224	0.046
2.2		PI	- 1.632	0.073
2.2		PO	1.663	0.063
2.2		S	- 2.510	0.160

Table 3.19: The 2.2 GeV raw proton elastic asymmetries extracted via the fit process.

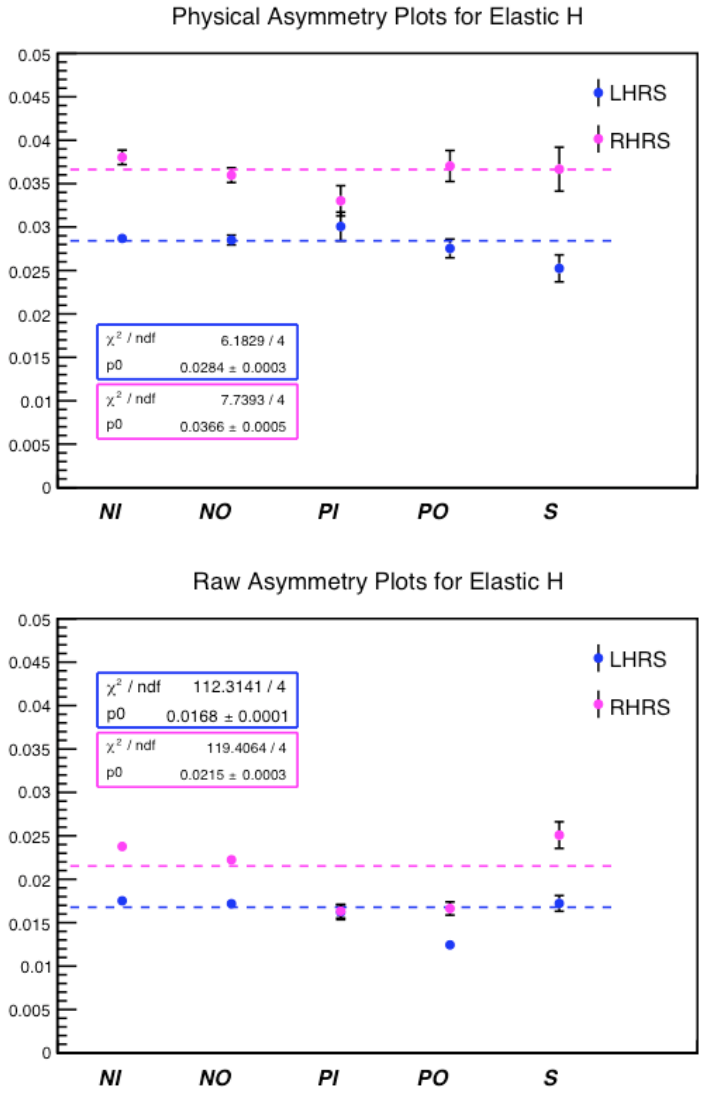

Figure 3.21: The 2.2 GeV physical asymmetries extracted via the fit process for each run list and spectrometer arm. Estimated means and standard deviations for each arm of the spectrometer are provided on the plot. The mean asymmetries are plotted and indicated by the coloured dashed curves.

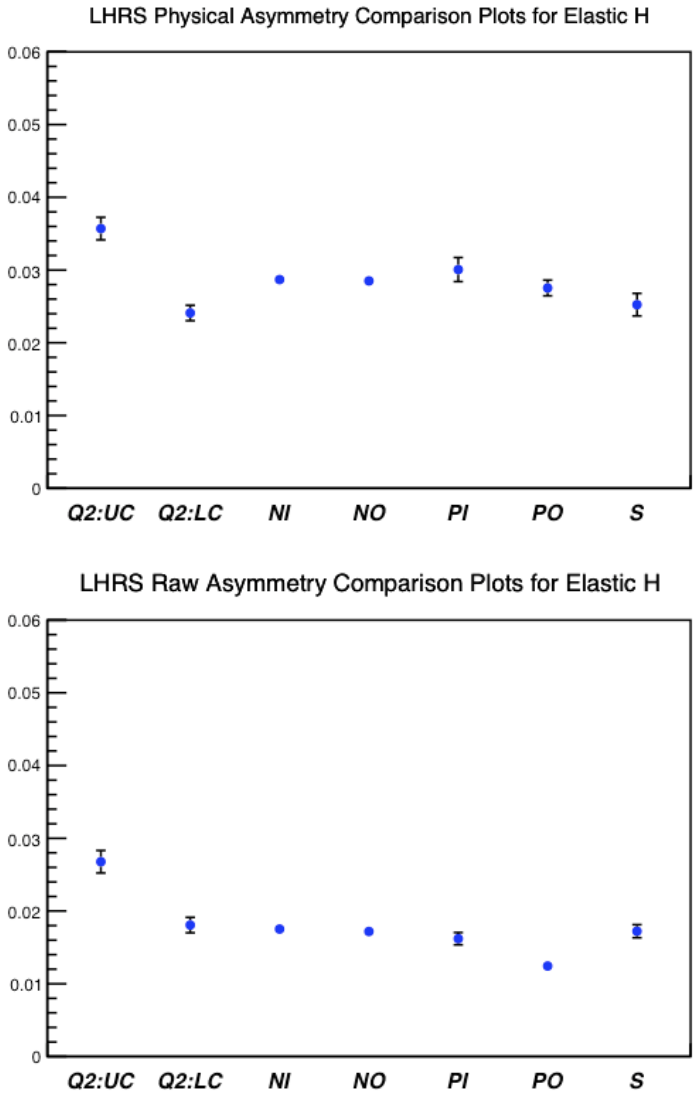

Figure 3.22: The 2.2 GeV physical asymmetries extracted for each run list via the fit process for the LHRS are replotted from Figure 3.21. Also plotted are the asymmetries obtained for the lower and upper Q^2 cut regions from Reference [35]. These regions are delineated by ($Q2$:LC) and ($Q2$:UC), respectively. The mean run list asymmetry lies between the Reference [35] results as indicated by the blue dashed line.

3.2.8 Experimental Issues

During the review of the Hall A logs for experiments E08-027 and E08-007[15], a number of issues with the 1.7 and 1.1 GeV cases surfaced. After processing the 2.2 GeV run lists for PO and PI, some additional issues were noted. These issues are discussed in the following sections.

Run Lists for 2.2 GeV

For the 2.2 GeV kinematics, a review of the experimental logs brought to light a number of issues that occurred during the production PI and PO runs. These lists consisted of four, and up to seven, individual runs which had a wide range of target polarization values recorded, between 0.43 and 0.80. A consequence of this, was that the average target polarization calculated for these lists were not necessarily the most representative for the measured overall data. From reviewing the logs, it was noted that the target magnet's current would spontaneously drop, in addition to a series of unidentified high voltage alarms that occurred. Even though the asymmetries for these lists shown in Tables 3.18 and 3.19 were in agreement with the other run lists, the subsequent form factor ratio calculations would be affected by these issues since it was unclear what the mean target polarization value actually was. As a result, the PI and PO lists are omitted from further analysis because of the uncertainty associated with these issues. Note, that since these represented only a small number of runs, the overall statistical precision was not greatly affected by these omissions.

Run Lists for 1.7 GeV

It was found that the 1.7 GeV fitting process produced fits that were less representative of the overall measurements, as shown in Figures 3.23 and 3.24. The elastic hydrogen reaction component was shifted somewhat towards the heavy elastic peak. In addition, one of the quasi-elastic components was suppressed in order to obtain the best overall fits. There was also a noticeable degree of mis-fit along the radiative tail, and more so in the region of the hydrogen elastic peak. The identical fit process used to optimize the 2.2 GeV run list fits discussed previously was applied to the 1.7

[15]These experiments acquired data during the same time period.

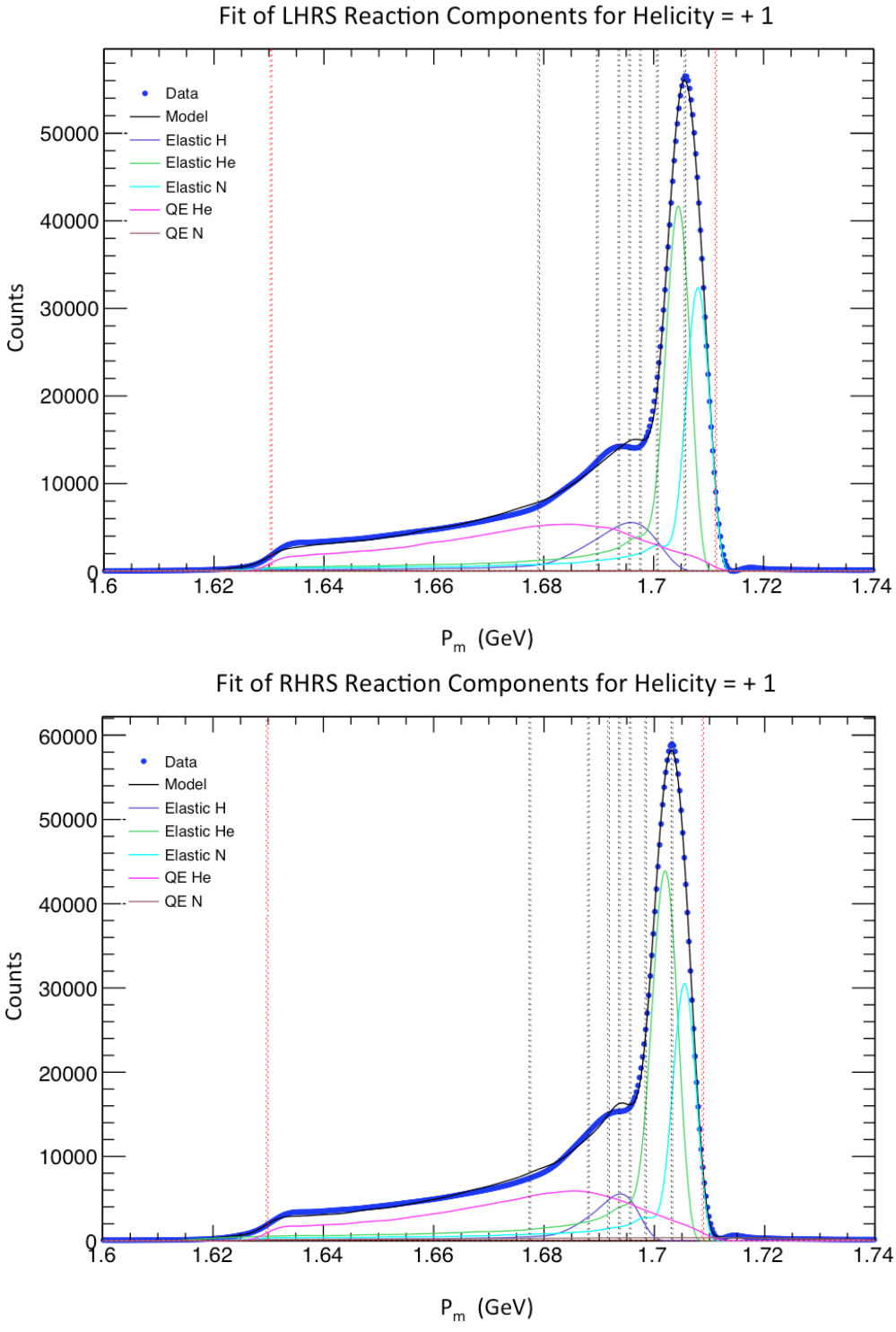

Figure 3.23: The 1.7 GeV baseline run-pair fits for the +1 helicity spectra associated with each spectrometer. The black curves in the plots represent the fitted model while the colour of each reaction component is provided in the caption of Figure 3.11.

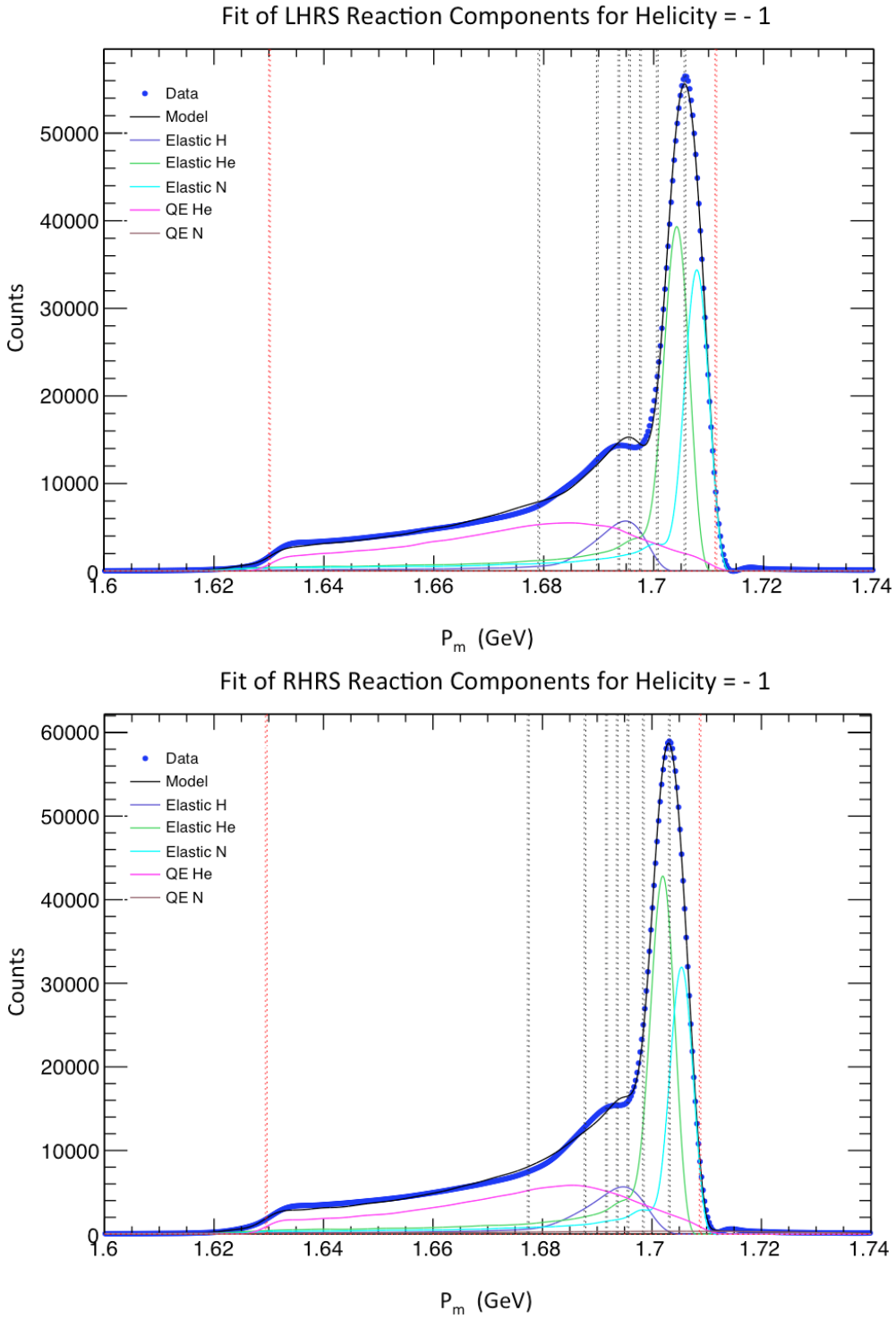

Figure 3.24: The 1.7 GeV baseline run-pair fits for the -1 helicity spectra associated with each spectrometer. The black curves in the plots represent the fitted model while the colour of each reaction component is provided in the caption of Figure 3.11.

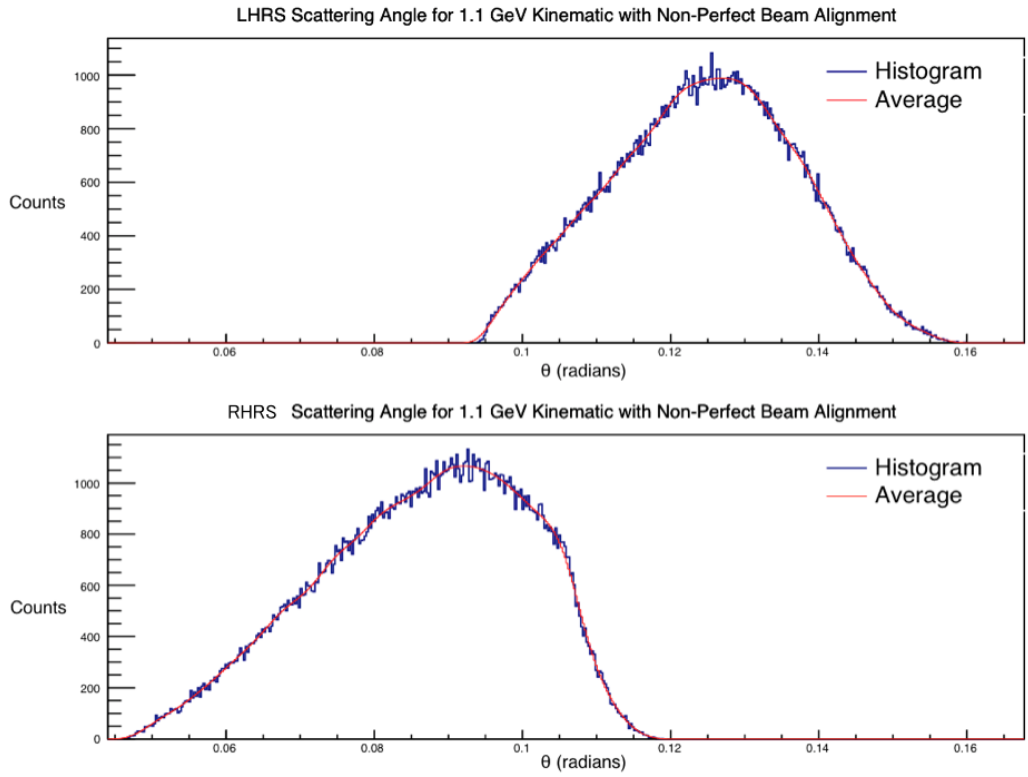

Figure 3.25: The simulated LHRS and RHRS scattering angle distributions for the 1.1 GeV kinematic created using the mean beam data provided in Table 3.1.

GeV run lists. Unfortunately, this fit process failed to generate representative fits as illustrated in these figures. The asymmetries produced from the fits resulted in small negative DSA form factor ratios, and non-realistic results for the single arm calculations. A significant issue was also noted in the logs with the septum magnets tripping off and not being at the proper current. For these reasons, the 1.7 GeV run lists were omitted from further analysis for this thesis.

Run Lists for 1.1 GeV

When attempting to analyze the 1.1 GeV data, evidence of a beam misalignment arose. To illustrate, the simulated scattering angle distributions for this kinematic were generated for each arm of the spectrometer using the mean beam data provided in Table 3.1. Those results are shown in Figure 3.25. These distributions are significantly different in their overall shape, degree of overlap, and their angular placement. This suggests that there was a beam misalignment issue. To investigate this further, the Q^2

distributions associated with the 2.2, 1.7 and 1.1 GeV kinematics were also generated. In addition, new Q^2 distributions were generated assuming perfect beam alignment rather than using the data from Table 3.1. These results are provided in Figures 3.26 through 3.28. Each figure has four plots. The top two plots show the Q^2 distributions generated using the data from Table 3.1 while the bottom two plots show perfect beam alignment results. The LHRS distributions are shown in the first and third plots while the RHRS distributions are provided in the second and fourth plots of these figures, respectively. The 2.2 and 1.7 GeV distributions are very similar for both cases; however, that is not the case for the 1.1 GeV distributions shown in Figure 3.28. The most noticeable trait in the top two plots of this figure is the lack of sufficient overlap in the Q^2 distributions required to support the DSA form factor ratio calculations. The 1.1 GeV beam orientation data in Table 3.1 are as much as 2.4 cm off the optimal beam position in Y and -4 mm in X. The mean beam angles θ_b and ϕ_b in this table are seen to be more than twice and ten times larger than the data associated with the other two kinematics, respectively. This shows that the beam was in fact misaligned for these runs and that the issue was not with the spectrometer. As a result, the 1.1 GeV data were omitted from further analysis in this thesis due to this issue.

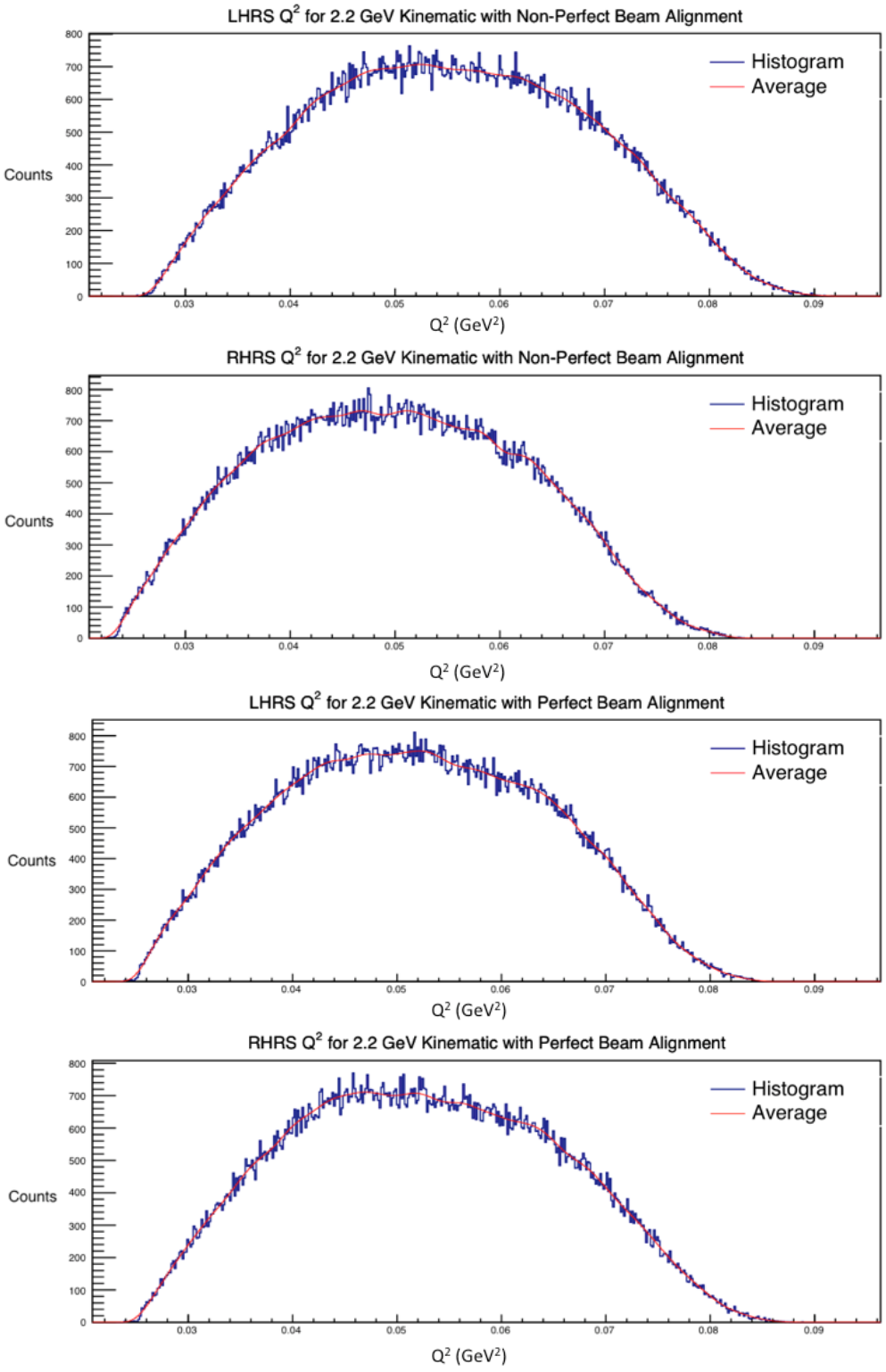

Figure 3.26: The 2.2 GeV simulated Q^2 distributions for LHRS and RHRS created using the mean beam data provided in Table 3.1 are shown in the top two plots of this figure. The perfect beam alignment results are shown in the bottom two plots.

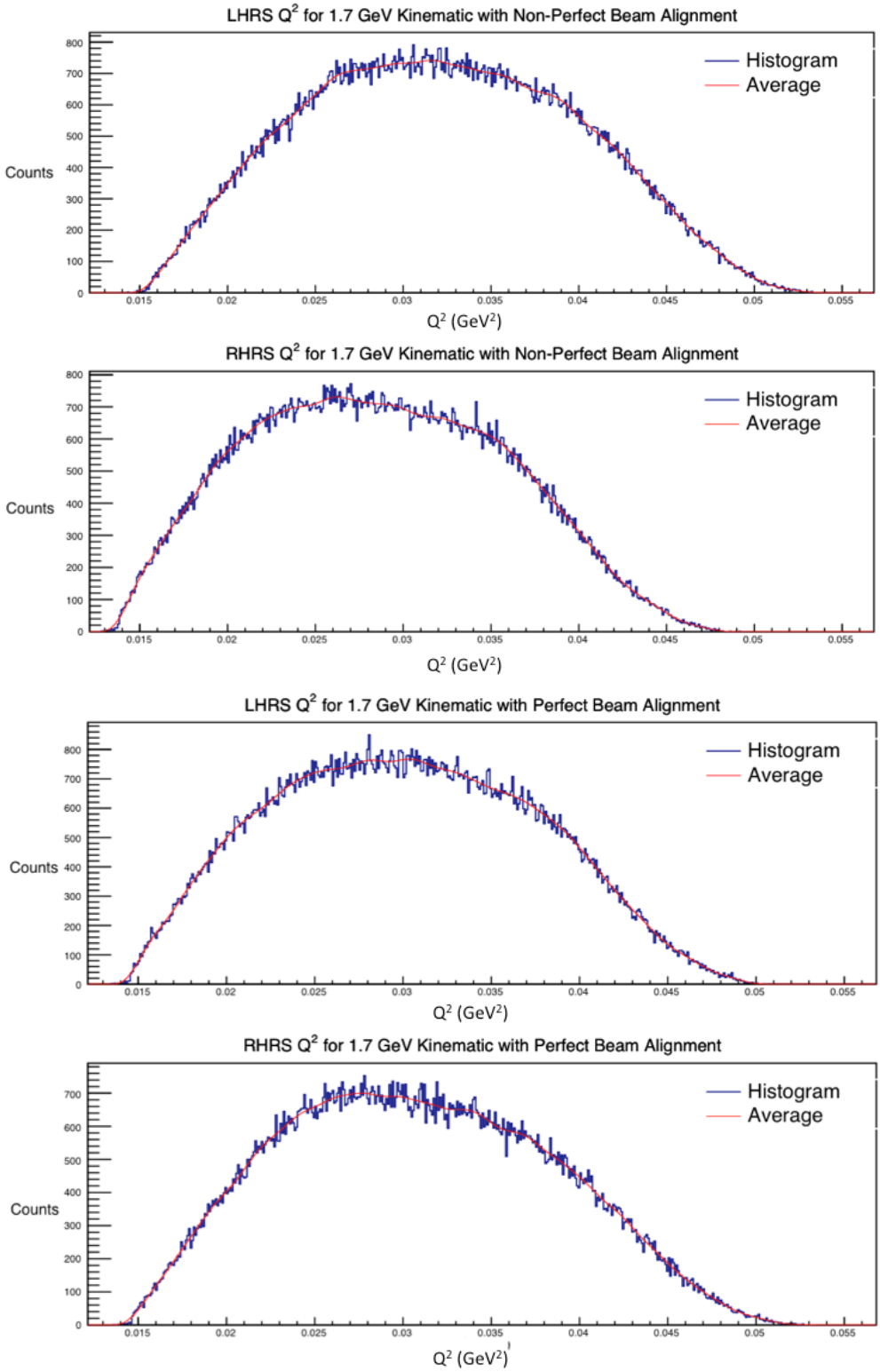

Figure 3.27: The 1.7 GeV simulated Q^2 distributions for LHRS and RHRS created using the mean beam data provided in Table 3.1 are shown in the top two plots of this figure. The perfect beam alignment results are shown in the bottom two plots.

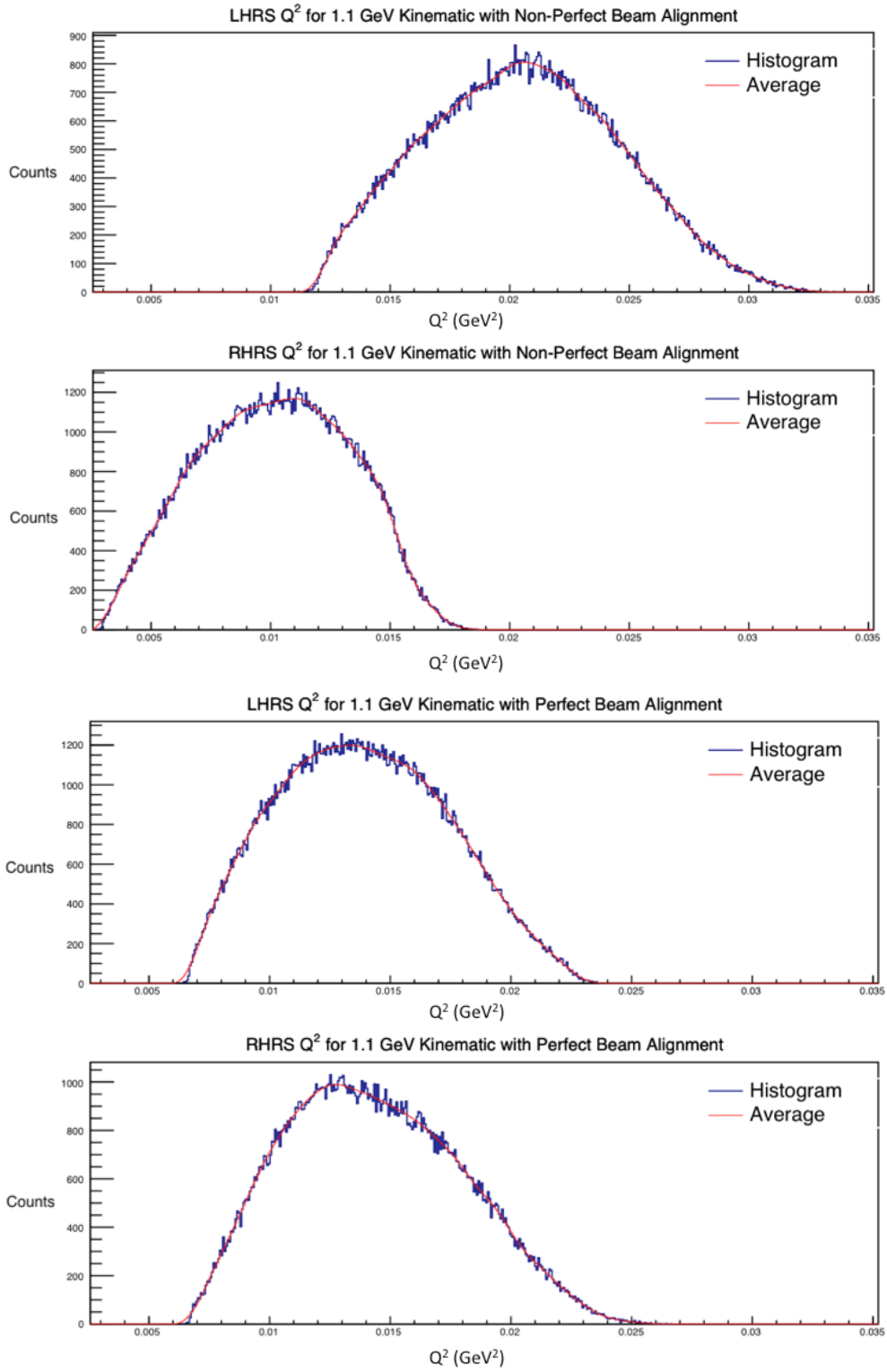

Figure 3.28: The 1.1 GeV simulated Q^2 distributions for LHRS and RHRS created using the mean beam data provided in Table 3.1 are shown in the top two plots of this figure. The perfect beam alignment results are shown in the bottom two plots.

Chapter 4

Discussion and Conclusions

This chapter will discuss and present the main results of this investigation. In particular, the fitting process's ability to support the extraction of proton elastic scattering asymmetry results from the momentum spectra will be addressed. Furthermore, the ability to use Monte Carlo simulations to support the calculation of proton elastic form factor ratios using the asymmetries provided by the fit process will be explored. The proton elastic form factor ratios that were able to be determined from the data will be shown in comparison to existing world data, and to theoretical predictions.

Asymmetry Extraction

The fact that the RHRS had a number of issues during the data taking period (as discussed), precluded using the standard reconstruction process. Therefore, the approach taken here was to fit simulated reaction components (hydrogen elastic, plus background contributions) to support the extraction of proton elastic asymmetry results. To that end, it was found that this approach has merit. In particular, the independent analysis results from Reference [35] support this conclusion specifically for the 2.2 GeV results associated with the left arm spectrometer. With respect to the right arm results, Figure 3.22 indicates that higher asymmetry values were obtained. In fact, even though the fitted models were found to clearly represent the measured momentum spectra, some issues were noted. When the spectra had background tail structures at its higher momentum range, the fit process tended to enhance the quasi-elastic background reaction components to fit these structures. An examination of Figures 3.14 through 3.17 in Section 3.2.3, shows a marked difference in the fitted contributions associated with the modelled backgrounds and the elastic hydrogen components associated with the LHRS and RHRS. The consequence of the fit process modelling these extended structures at the high momentum ranges appears to be that higher backgrounds are estimated for these RHRS spectra with respect to

Energy (GeV)	Method	Run List	Q^2 (GeV^2)	FFR	Δ FFR
2.2	DSA	NI	0.0513	0.138	0.012
		NO	0.0514	0.169	0.019
	LHRS	NI	0.0513	1.142	0.023
		NO	0.0514	1.153	0.025
		Avg	0.0513	1.147	0.017
	RHRS	NI	0.0513	0.802	0.022
		NO	0.0514	0.860	0.025
		Avg	0.0518	0.831	0.017

Table 4.1: The 2.2 GeV form factor ratios obtained for the NI and NO run lists generated using DSA and single arm calculations. In addition, an error of 2.3×10^{-5} GeV^2 is associated with the values of Q^2 in the table.

their elastic hydrogen contributions.

Even with this issue, the quality of the fits obtained suggests that a model based extraction of asymmetry data shows promise and has the potential to be an effective tool to support experimental analysis.

Form Factor Ratios

The previous section confirmed that the fit process was able to extract realistic proton elastic asymmetry results for the LHRS. Given that the RHRS data could not be reconstructed in the normal fashion, a Monte Carlo simulation was used to estimate the kinematic variables associated with the simulated events. In particular, the elastic hydrogen reaction events used in the fitting process were used to generate estimates of the variables required to support form factor ratio calculations. Histograms of these variables provided estimated means and uncertainties used in these calculations.

The form factor ratio was calculated using the asymmetries provided in Section 3.2.7 using both the DSA technique and the single arm method described in Sections 1.3.3 and 1.3.4, respectively. Table 4.1 summarizes the form factor ratio results for the 2.2 GeV run lists for each calculation method. The single arm results for the LHRS run lists are self-consistent to within experimental uncertainty. How this result compares to the unpolarized and polarized world data are illustrated in Figure 1.1 and the theoretical predictions/models along with the world's data shown in Figure 1.5 will now be explored. The data in Table 4.1 are plotted in Figures 4.1 and 4.2 along with the average result for the left and right arms of the spectrometer

(labelled as "Avg" in Table 4.1). The left and top graphics in these figures show the individual run list results plotted along with the established world's data. The right and bottom graphics show the averaged results clearly contribute a single reliable measurement of the form factor ratio; however, its magnitude does little to resolve the discrepancies and the question regarding structures in the proton form factor ratio, unfortunately. The unusual/discrepant result observed in the DSA form factor ratios stem in part from the overall issues associated with the right arm data and its subsequent spectra. It was noted that the fit process over estimates the background while under estimating the elastic hydrogen contribution when it accounts for tail structures in the higher momentum range. This results in higher estimated proton elastic asymmetries for the right arm. Consequently, the ratio of the asymmetries is quite high. Figure 4.3 uses the data in Table 3.7 to plot the DSA form factor ratio as a function of the asymmetry ratio (A_1/A_2). This figure shows that an asymptote exists at $A_1/A_2 = 0.9683$. In addition, it illustrates that the NI run list form factor ratio is 0.138 when $A_1/A_2 = 1.357$. For the NO run list, the the form factor ratio jumps to 0.169 at $A_1/A_2 = 1.294$. This figure illustrates how the form factor ratio behaves with respect to the ratio of the asymmetries. It is clear that larger values of A_1/A_2, such as in the NO and NI cases, result in the small form factor ratios. Ultimately, this shows that the DSA approach is quite sensitive to the asymmetry ratio afforded by the fit process used here.

Even though the LHRS single arm asymmetry results were in agreement with the independent analysis [35], the uncertainties in subsequent form factor ratios determined here using that data need to be understood and assessed. Table 4.2 shows the overall contributors to the form factor ratio uncertainties for the DSA and single arm calculations. This table shows the % errors associated with each partial derivative of the form factor ratios given by the expressions in Equation 3.16. Using differential uncertainty analysis, these partials are multiplied by the uncertainty in their associated kinematic variable and added in quadrature. What these values highlight are that the dominant contributor to the overall uncertainty in the estimated form factor ratios comes from the uncertainty in the estimated asymmetries.

It is important to understand that any number of issues with the equipment, as well as, any mistakes in calibrations can affect subsequent results calculated using

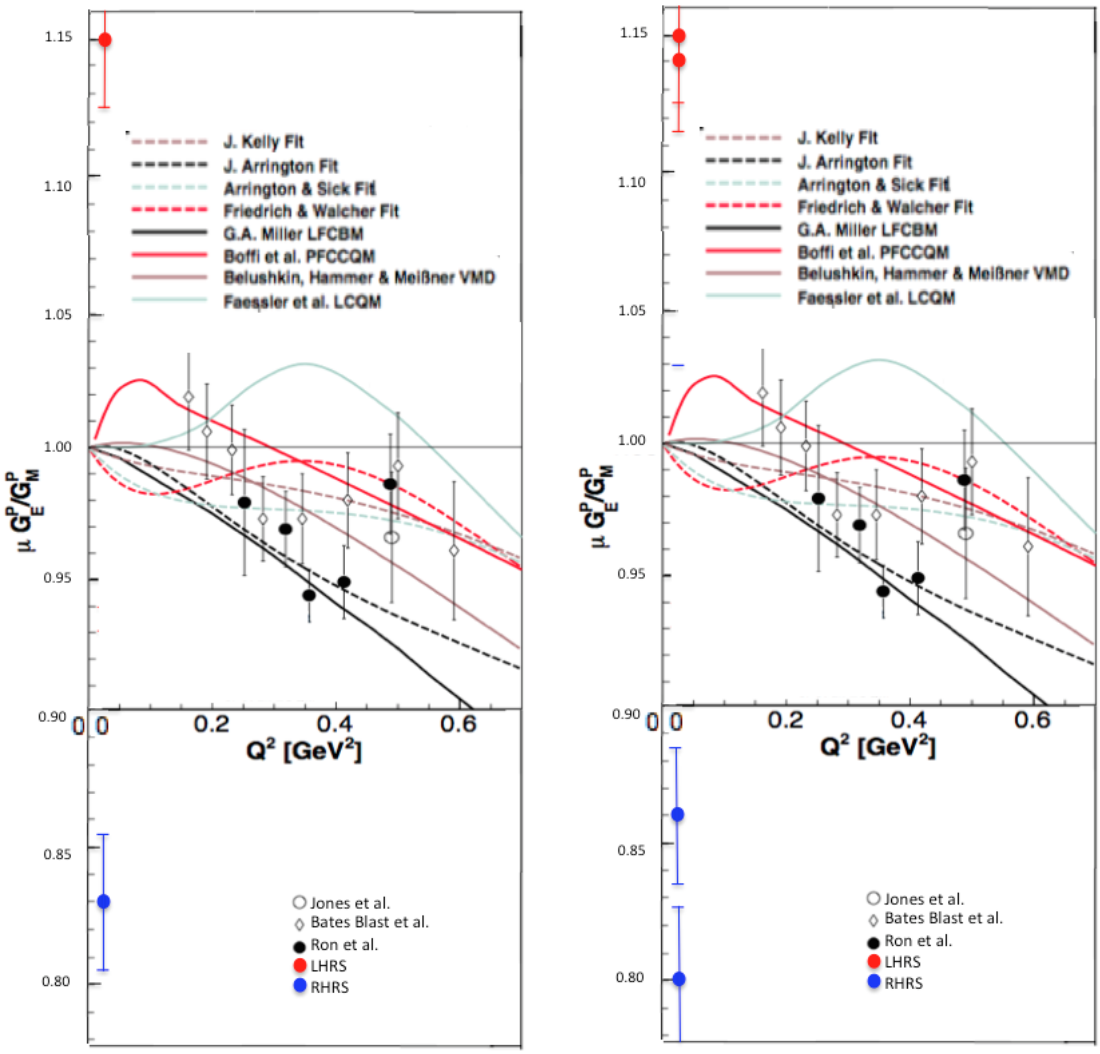

Figure 4.1: The 2.2 GeV single arm form factor ratios from Table 4.1 are plotted along with the established body of data. The left graphic contains the individual run list results while the right graphic shows the averaged results for the LHRS and the RHRS.

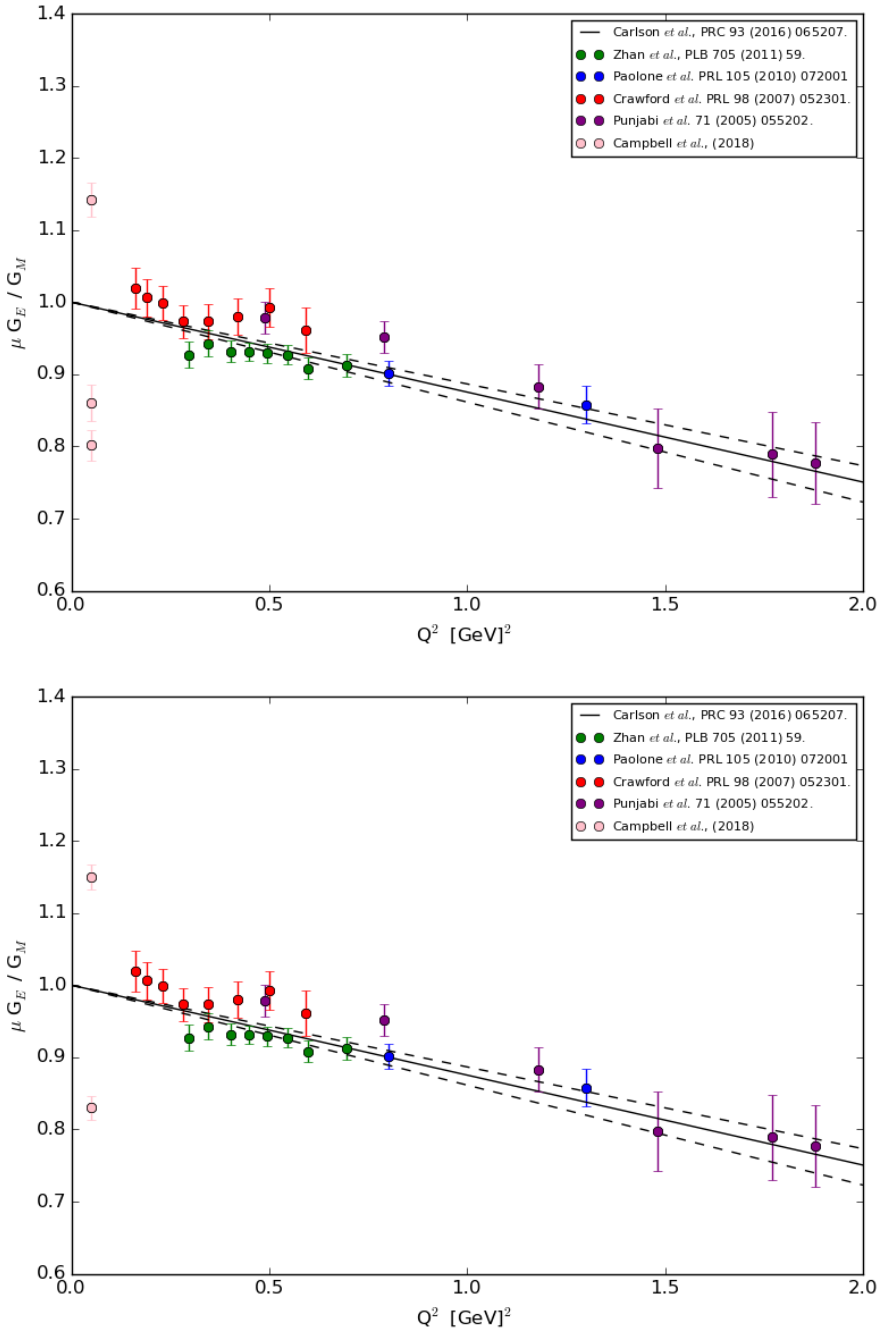

Figure 4.2: The 2.2 GeV single arm form factor ratios from Table 4.1 are plotted with recent world data [2, 23, 28, 88] and the Carlson Model results [38]. The top graphic contains the individual run list results while the bottom graphic shows the averaged results for the LHRS and the RHRS.

FFR Method	FFR Partials	Run List: NI Errors (%)	Run List: NO Errors (%)
DSA	∂_{μ}	3.00×10^{-11}	3.00×10^{-11}
	∂_{θ_1}	1.35×10^{-4}	1.32×10^{-4}
	∂_{θ_2}	5.41×10^{-5}	5.04×10^{-5}
	$\partial_{\theta_1^*}$	0.26	0.25
	$\partial_{\theta_2^*}$	0.39	0.36
	$\partial_{\phi_1^*}$	7.79×10^{-4}	9.29×10^{-4}
	$\partial_{\phi_2^*}$	1.00×10^{-4}	1.11×10^{-4}
	$\partial_{\Gamma_{12}}$	8.96	11.32
	∂_{τ}	0.02	0.02
	ΔFFR	8.97	11.33
LHRS	∂_{μ}	3.00×10^{-11}	3.00×10^{-11}
	∂_{θ_2}	0.04	0.04
	$\partial_{\theta_2^*}$	0.01	0.01
	$\partial_{\phi_2^*}$	3.20×10^{-5}	3.17×10^{-5}
	∂_{A_s}	1.99	2.15
	∂_{τ}	0.02	0.02
	ΔFFR	1.98	2.15
RHRS	∂_{μ}	3.00×10^{-11}	3.00×10^{-11}
	∂_{θ_1}	0.04	0.04
	$\partial_{\theta_1^*}$	8.22×10^{-3}	6.53×10^{-3}
	$\partial_{\phi_1^*}$	3.51×10^{-4}	3.42×10^{-4}
	∂_{A_s}	2.69	2.95
	∂_{τ}	0.02	0.02
	ΔFFR	2.69	2.95

Table 4.2: Contribution sources from the differential uncertainty analysis to the overall form factor ratio errors for the 2.2 GeV NI and NO run lists. The form factor ratio partials with respect to a variable 'x' are denoted by "∂_x" and represents the error term $|\partial_x FFR \times \Delta x|$. The percent error is determined by dividing this term by the FFR value and multiply by 100%. Therefore, if these % errors are added in quadrature they result in the ΔFFR values shown in this table.

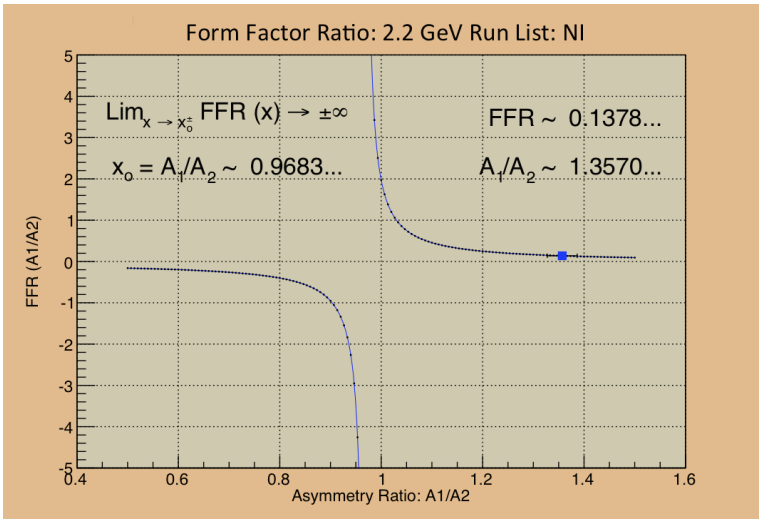

Figure 4.3: The 2.2 GeV form factor ratio as a function of the asymmetry ratio A_1/A_2 using the data found in Table 3.7 and Equation 1.61. An asymptote exists at x_o and the form factor ratio is plotted as the blue square.

those data. Any misalignment of the chicane magnets, errors in the field map, or problems with the spectrometer magnets are problematic. These kinds of issues are clearly evident in the distortions noted in the distributions of the RHRS plots shown in Figures 3.9 and 3.10. The Monte Carlo simulation uses both the field map and optics calibrations to generate events. Therefore, any errors would manifest in the simulated reaction component events. However, the fit process's ability to generate representative spectra models suggest that the simulation is an effective tool for supporting this kind of analysis.

The analysis performed here has shown several things of note. First, it seems that a model based approach for extracting asymmetries can generate realistic results given that the measured momentum spectra are well behaved and representative of the underlying physics. Second, the fit process for the case when the data are not well behaved suggests that the modelling process is missing something because it seems that the background is not being correctly estimated. Possibly adding duplicate reaction components to the fit process might provide a better estimate while still accounting for the tail structures observed in the higher momentum range. However, this would require a much better understanding of how the right arm issues resulted in the measured distributions observed in the plots shown in Figures 3.9 and 3.10.

In addition, Figure 4.2 clearly illustrates that the attempt to provide new information on the electromagnetic form-factor ratio for elastic electron scattering from the proton at the lowest-ever attempted value of momentum-transfer resulted in a highly intriguing result. If correct, it indicates that there is a trend at Q^2 tends to zero that is unexpected based on other existing data at low Q^2 (although these measurements are for larger values of Q^2 compared to this new result). This result would suggest that further studies in this Q^2 region demands a follow up measurement to check the validity.

Furthermore, this result is related intimately with the extraction of the proton radius. In order to determine the proton radius, the individual form factors are required. Unfortunately, this thesis measured the ratio of the form factors not the individual form factors themselves. Therefore, it cannot be definitively stated that the proton radius is larger than previously measured but it does indicate that something may be happening with the form factors as Q^2 tends to zero. This however, will require further investigation to understand what is driving the low Q^2 form factor ratio behaviour (either G_E or G_M).

Finally, the analysis method employed here generated independent results for the form factor ratios for each of the left and right arms, each having an estimated uncertainty of roughly the same magnitude as the previous measurements done at the lowest-to-date Q^2 values (i.e, the LEDEX and BLAST data). However, the fact that the left and right arm results do not agree to within their uncertainty, points to a problem somewhere in these results. The problem could either be that: (1) the uncertainties are underestimated, or (2) the right arm results simply are not reliable. It seems less likely that option (1) is the culprit since our method for estimating the model uncertainty and folding it into the quoted errors was very conservative. Thus, making option (2) the more plausible choice since the extracted left arm asymmetry does not disagree with the independent analysis performed by Friedman [35], and that is coupled with all of the stated issues with the right arm. Clearly, the method used here was unable to salvage the right arm data, nor was it able to provide the sought after DSA form factor ratios. However, it was able to confirm Friedman's asymmetry extraction with an independent approach plus provide a now-proven technique for extracting the form factor ratios using the left arm asymmetry data.

Appendix A

Reaction Component Parameter Values

The tables provided in this appendix include the values for the fit parameters α_k, β_k, and γ_k that were obtained from the fitting process for Algorithm 3. Specifically, it includes the fit results for the 2.2 GeV kinematic for both the NI and NO run lists for each HRS and helicity state.

Table A.1: Fit parameters for the left HRS NI run list for the −1 helicity events.

Models		γ_i	α_i	β_i
Elastic	H	$9.2678\times10^{-1} \pm 4.9746\times10^{-4}$	$1.0411\times10^{+0} \pm 1.6835\times10^{-4}$	$9.0420\times10^{-2} \pm 3.4589\times10^{-4}$
	He	$7.0516\times10^{+1} \pm 5.0418\times10^{-1}$	$1.0030\times10^{+0} \pm 1.5086\times10^{-4}$	$1.6909\times10^{-2} \pm 3.3384\times10^{-4}$
	N	$5.1645\times10^{+1} \pm 1.6174\times10^{-1}$	$1.0016\times10^{+0} \pm 7.3076\times10^{-5}$	$9.9922\times10^{-3} \pm 1.6507\times10^{-4}$
QE	He	$7.1544\times10^{-1} \pm 3.8637\times10^{-4}$	$8.2814\times10^{-1} \pm 8.1209\times10^{-5}$	$-4.6291\times10^{-1} \pm 2.6599\times10^{-4}$
	N	$1.7192\times10^{-1} \pm 1.4376\times10^{-4}$	$9.6067\times10^{-1} \pm 1.7673\times10^{-4}$	$-8.8982\times10^{-2} \pm 4.3192\times10^{-4}$

Table A.2: Fit parameters for the left HRS NI run list for the +1 helicity events.

Models		γ_i	α_i	β_i
Elastic	H	$9.5708\times10^{-1} \pm 4.6747\times10^{-4}$	$1.0381\times10^{+0} \pm 1.2864\times10^{-5}$	$8.4208\times10^{-2} \pm 2.7341\times10^{-5}$
	He	$7.0422\times10^{+1} \pm 2.6474\times10^{-1}$	$1.0024\times10^{+0} \pm 3.0745\times10^{-5}$	$1.5594\times10^{-2} \pm 6.6421\times10^{-5}$
	N	$5.1755\times10^{+1} \pm 8.5704\times10^{-2}$	$1.0018\times10^{+0} \pm 2.0948\times10^{-5}$	$1.0426\times10^{-2} \pm 4.3589\times10^{-5}$
QE	He	$7.1439\times10^{-1} \pm 5.5772\times10^{-4}$	$8.2770\times10^{-1} \pm 2.1761\times10^{-6}$	$-4.6435\times10^{-1} \pm 6.9108\times10^{-6}$
	N	$1.7199\times10^{-1} \pm 2.2488\times10^{-4}$	$9.6020\times10^{+1} \pm 2.5614\times10^{-4}$	$-9.0147\times10^{-2} \pm 6.2710\times10^{-4}$

Table A.3: Fit parameters for the right HRS NI run list for the −1 helicity events.

Models		γ_i	α_i	β_i
Elastic	H	$4.1393\times10^{-1} \pm 3.3031\times10^{-4}$	$1.0488\times10^{+0} \pm 4.4984\times10^{-4}$	$9.8819\times10^{-2} \pm 9.1183\times10^{-4}$
	He	$1.7190\times10^{+2} \pm 4.9064\times10^{-2}$	$9.0845\times10^{-1} \pm 5.3891\times10^{-5}$	$-2.1232\times10^{-1} \pm 1.4358\times10^{-4}$
	N	$1.1908\times10^{+0} \pm 3.2200\times10^{-3}$	$7.0730\times10^{-1} \pm 8.6904\times10^{-4}$	$-8.7217\times10^{-1} \pm 3.8475\times10^{-3}$
QE	He	$3.3242\times10^{-1} \pm 4.4007\times10^{-4}$	$8.1807\times10^{-1} \pm 1.2468\times10^{-4}$	$-5.0054\times10^{-1} \pm 4.1677\times10^{-4}$
	N	$8.1839\times10^{-2} \pm 1.7130\times10^{-4}$	$9.3654\times10^{-1} \pm 3.1827\times10^{-5}$	$-1.5349\times10^{-1} \pm 8.2131\times10^{-5}$

Table A.4: Fit parameters for the right HRS NI run list for the +1 helicity events.

Models		γ_i	α_i	β_i
Elastic	H	$4.3393\times10^{-1} \pm 3.3243\times10^{-4}$	$1.0484\times10^{+0} \pm 4.1737\times10^{-4}$	$9.7987\times10^{-2} \pm 8.4662\times10^{-4}$
	He	$1.7229\times10^{+2} \pm 4.9224\times10^{-2}$	$9.0882\times10^{-1} \pm 5.3841\times10^{-5}$	$-2.1132\times10^{-1} \pm 1.4332\times10^{-4}$
	N	$1.1951\times10^{+0} \pm 3.2288\times10^{-3}$	$7.0754\times10^{-1} \pm 8.7848\times10^{-4}$	$-8.7112\times10^{-1} \pm 3.8882\times10^{-3}$
QE	He	$3.3130\times10^{-1} \pm 4.4145\times10^{-4}$	$8.1805\times10^{-1} \pm 1.2762\times10^{-4}$	$-5.0063\times10^{-1} \pm 4.2663\times10^{-4}$
	N	$8.2027\times10^{-2} \pm 1.7193\times10^{-4}$	$9.3649\times10^{-1} \pm 3.1841\times10^{-5}$	$-1.5363\times10^{-1} \pm 8.2177\times10^{-5}$

Table A.5: Fit parameters for the left HRS NO run list for the −1 helicity events.

Models		γ_i	α_i	β_i
Elastic	H	$5.9557\times10^{-1} \pm 5.0430\times10^{-4}$	$1.0474\times10^{+0} \pm 4.8319\times10^{-4}$	$1.0311\times10^{-1} \pm 9.8105\times10^{-4}$
	He	$5.2707\times10^{+1} \pm 7.2138\times10^{-1}$	$9.9459\times10^{-1} \pm 4.4196\times10^{-4}$	$-1.5834\times10^{-3} \pm 9.9521\times10^{-4}$
	N	$2.9948\times10^{+1} \pm 2.3503\times10^{-1}$	$9.9794\times10^{-1} \pm 1.5623\times10^{-4}$	$2.0755\times10^{-3} \pm 3.4774\times10^{-4}$
QE	He	$4.5629\times10^{-1} \pm 3.9387\times10^{-4}$	$8.4708\times10^{-1} \pm 1.0027\times10^{-4}$	$-4.0243\times10^{-1} \pm 3.1275\times10^{-4}$
	N	$1.0889\times10^{-1} \pm 1.8746\times10^{-4}$	$9.7845\times10^{-1} \pm 2.2366\times10^{-5}$	$-4.6573\times10^{-2} \pm 5.2918\times10^{-5}$

Table A.6: Fit parameters for the left HRS NO run list for the +1 helicity events.

Models		γ_i	α_i	β_i
Elastic	H	$5.7633\times10^{-1} \pm 4.9884\times10^{-4}$	$1.0490\times10^{+0} \pm 5.0321\times10^{-4}$	$1.0644\times10^{-1} \pm 1.0185\times10^{-3}$
	He	$5.2199\times10^{+1} \pm 7.0995\times10^{-1}$	$9.9506\times10^{-1} \pm 4.4229\times10^{-4}$	$-5.1635\times10^{-4} \pm 9.9454\times10^{-4}$
	N	$3.0101\times10^{+1} \pm 2.3121\times10^{-1}$	$9.9777\times10^{-1} \pm 1.5733\times10^{-4}$	$1.6795\times10^{-3} \pm 3.5030\times10^{-4}$
QE	He	$4.5704\times10^{-1} \pm 3.9341\times10^{-4}$	$8.4754\times10^{-1} \pm 1.0123\times10^{-4}$	$-4.0098\times10^{-1} \pm 3.1537\times10^{-4}$
	N	$1.0901\times10^{-1} \pm 1.8730\times10^{-4}$	$9.7878\times10^{-1} \pm 2.2248\times10^{-5}$	$-4.5808\times10^{-2} \pm 5.2604\times10^{-5}$

Table A.7: Fit parameters for the right HRS NO run list for the −1 helicity events.

Models		γ_i	α_i	β_i
Elastic	H	$2.9568\times10^{-1} \pm 2.7356\times10^{-4}$	$1.0534\times10^{+0} \pm 5.2063\times10^{-4}$	$1.0798\times10^{-1} \pm 1.0462\times10^{-3}$
	He	$1.1594\times10^{+2} \pm 4.0029\times10^{-2}$	$9.1136\times10^{-1} \pm 6.6315\times10^{-5}$	$-2.0476\times10^{-1} \pm 1.7557\times10^{-4}$
	N	$7.0059\times10^{-1} \pm 2.3756\times10^{-3}$	$7.0512\times10^{-1} \pm 1.1590\times10^{-3}$	$-8.8150\times10^{-1} \pm 5.1613\times10^{-3}$
QE	He	$2.2380\times10^{-1} \pm 3.6623\times10^{-4}$	$8.2047\times10^{-1} \pm 1.6450\times10^{-4}$	$-4.9263\times10^{-1} \pm 5.4670\times10^{-4}$
	N	$5.6829\times10^{-2} \pm 1.4299\times10^{-4}$	$9.3995\times10^{-1} \pm 3.7620\times10^{-5}$	$-1.4496\times10^{-1} \pm 9.6374\times10^{-5}$

Table A.8: Fit parameters for the right HRS NO run list for the +1 helicity events.

Models		γ_i	α_i	β_i
Elastic	H	$2.8338\times10^{-1} \pm 2.7223\times10^{-4}$	$1.0555\times10^{+0} \pm 5.6525\times10^{-4}$	$1.1228\times10^{-1} \pm 1.1313\times10^{-3}$
	He	$1.1583\times10^{+2} \pm 3.9931\times10^{-2}$	$9.1108\times10^{-1} \pm 6.6362\times10^{-5}$	$-2.0550\times10^{-1} \pm 1.7582\times10^{-4}$
	N	$6.9470\times10^{-1} \pm 2.3704\times10^{-3}$	$7.0437\times10^{-1} \pm 1.1583\times10^{-3}$	$-8.8477\times10^{-1} \pm 5.1661\times10^{-3}$
QE	He	$2.2421\times10^{-1} \pm 3.6607\times10^{-4}$	$8.2065\times10^{-1} \pm 1.6750\times10^{-4}$	$-4.9204\times10^{-1} \pm 5.5642\times10^{-4}$
	N	$5.6847\times10^{-2} \pm 1.4299\times10^{-4}$	$9.3999\times10^{-1} \pm 3.7596\times10^{-5}$	$-1.4485\times10^{-1} \pm 9.6306\times10^{-5}$

Bibliography

[1] O. Stern, Nature, 132:103, 1933.

[2] C.B. Crawford et al., Phys. Rev. Lett., 98:052301, 2007.

[3] C.F Perdrisat et al., Prog. Part. Nucl. Phys., 59, 2007.

[4] H. Frauenfelder and E.M. Henley, Subatomic Physics, (Prentice-Hall Inc., New Jersey, 1974).

[5] W. Bartel et al., Phys. Lett., 33B, 245, 1970.

[6] C. Berger et al., Phys. Lett., 35B, 87, 1971.

[7] J. Arrington, I. Sick, Phys. Rev. C, 76:035201, 2007.

[8] R.G. Arnold et al., Phys. Rev. Lett., 57, 174, 1986.

[9] L. Andivahis et al., Phys. Rev D, 50, 5491, 1994.

[10] M.E. Christy et al., Phys. Rev. C, 70, 015206, 2004.

[11] I. Qattan et al., Phys. Rev. Lett., 94, 142301, 2005.

[12] F. Borkowski et al., Nucl. Phys., A222, 269, 1974.

[13] F. Borkowski et al., Nucl. Phys., B93, 461, 1975.

[14] G.G. Simon et al., Nucl. Phys., A333, 381, 1975.

[15] M.J. Alguard et al. Phys. Rev. Lett., 37:1258, 1976.

[16] D. Barkhuff et al., Phys. Lett., 470:39, 1999.

[17] B. Milbrath et al., Phys. Rev. Lett., 80:452, 1998.

[18] T. Pospischil et al., Eur. Phys. J. A, 12:125, 2001.

[19] S. Dietrich et al., Phys. Lett. B, 500:47, 1947.

[20] M.K. Jones et al., Phys. Rev. Lett., 84:1398, 2000.

[21] O. Gayou et al., Phys. Rev. C, 64, 038202, 2001.

[22] O. Gayou et al., Phys. Rev. Lett., 88, 092301, 2002.

[23] V. Punjabi, et al., Phys. Rev. C, 71, 055202, 2007.

[24] X. Zhan, Phys. Lett. B, 705, 59-64, 2011.

[25] J. Friedrich, T. Walcher, Eur. Phys. J. A, 17, 607, 2003.

[26] G. Ron et al., Phys. Rev. Lett., 99:202002, 2007.

[27] J. Arrington et al., JLAB proposal E08-007, 2007.

[28] X. Zhan, Ph.D. Thesis, Massachusetts Institute of Technology, 2010.

[29] R.A. Ricci, A. Molinari, Unfolding the Matter of Nuclei, EBSCO Publishing: eBook Collection, 1997.

[30] M. E. Peskin, D. V. Schroeder. An Introduction to Quantum Field Theory, (Addison-Wesley, USA, 1995).

[31] R. G. Sachs, Phys. Rev., 126:2256-2260, 1962.

[32] A.I. Akhiezer, M.P. Rekalo, Sov. Phys. Doklady 13, 572 (1968).

[33] N. Dombey, Rev. Mod. Phys, 41, 236,1969.

[34] A.I. Akhiezer, M.P. Rekalo, Sov. J. Part. Nucl., 3, 277, 1974.

[35] M. Friedman, Ph.D., Hebrew University of Jerusalem, 2017.

[36] T. W. Donnelly, A. S. Raskin, Annals Phys., 169, 1986.

[37] J. Jourdan et al., JLAB proposal, 2001.

[38] C. Carlson, Progress in Particle and Nuclear Physics, 82, 2015.

[39] I. Sick, Phys. Lett. B, 576(1):62-67, 2003.

[40] P.J Mohr, B.N. Taylomr, D.B. Newell, J. Phys. Chem. Ref. Data, 37(3):1187-1284, 2008.

[41] J.C. Bernauer et al., Phys. Rev. Lett., 105(24):242001, 2010.

[42] P.J. Mohr, B.N. Taylor, D.B. Newell, J. Phys. Chem. Ref. Data, 41(4):043109, 2012.

[43] R. Pohl et al., Nature, 466:213-216, 2010.

[44] A. Antognini et al., Science, 339 (6118), 2013.

[45] S. Boffi et al., arXiv:hep-ph/0108271v1.

[46] J. Alcorn et al., Nucl. Instrum. Methods A, 522, 294, 2004.

[47] A. Faessler, Phys. Rev. D, 73, 114021, 2006.

[48] S. Strauch et al., Phys. Rev. Lett., 91(5):052301, 2003.

[49] H. Bitao et al., Phys. Rev. C, 73(6):064004, 2006.

[50] CF Perdrisat, V Punjabi, M Vanderhaeghen, Nucleon electromagnetic form factors. Progs. Part. Nucl. Phys., 59(2):694-764, 2007.

[51] J Arrington, CD Roberts, JM Zanotti, Nucleon electromagnetic form factors. J. Phys. G: Nucl. Part. Phys., 34(7):S23, 2007.

[52] V Punjabi, CF Perdrisat, MK Jones, EJ Brash, CE Carlson, The structure of the nucleon: Elastic electromagnetic form factors, Eur. Phys. J. A, 51(7):1-44, 2015.

[53] S. Riordan, Ph.D., Carnegie Mellon University, 2008.

[54] F. Iachello, A. D. Jackson, A. Lande, Phys. Lett, 43 B:191 - 196, 1973.

[55] M. F. Gari, W. Krümpelmann. Phys. Lett, B 274:159 - 162, 1992

[56] E. Lomon. Phys. Rev., C 66:045501, 2002.

[57] R. Bijker, F. Iachello. Phys. Rev., C 69:068201, 2004.

[58] Hyde-Wright, de Jager, Annu. Rev. Nucl. Part. Sci, 54:217-267, 2004.

[59] G. Miller, Phys. Rev., C 66:032201, 2002.

[60] JJ Kelly. Phys. Rev. C, 70(6):068202, 2004.

[61] J. Arrington, Phys. Rev. C 69, 022201, 2004.

[62] T. Eden et al., Phys. Rev. C, 50(4):R1749, 1994.

[63] C. Herberg et al., Eur Phys. J. A., 5(2):131-135, 1999.

[64] Passchier et al., Phys. Rev. Lett., 82(25):4988, 1999.

[65] Golak et al., Phys. Rev. C, 63(3):034006, 2001.

[66] D. Rohe et al., Phys. Rev. Lett., 83(21):4257, 1999.

[67] R. Madey et al., Phys. Rev. Lett., 91(12):122002, 2003.

[68] G. Warren et al., Phys. Rev. Lett., 92(4):042301, 2004.

[69] R. Schiavilla, I. Sick, Phys. Rev. C, 64(4): 041002, 2001.

[70] W. Melnitchouk, J. Arrington, J.A. Tjon, Phys. Rev. C, 76:035205, 2007.

[71] M. Cummings, Ph.D., The College of William and Mary, 2016.

[72] D. Anez, Ph.D., Dalhousie University, 2014.

[73] P. Zhu, Ph.D., The University of Science and Technology of China, 2015.

[74] T.D. Averett et al., Nucl. Instrum. Method. A, 427(3):440 - 454, 1999.

[75] J. Pierce et al., Nucl. Instrum. Method. A, 738:54 - 60, 2014.

[76] C. Gu, Helicity Decoder for E08-027, Technical report, University of Virginia, August 2014.

[77] N. Liyanage, Calibration of the hall a high resolution spectrometers using the new optimizer, Technical report, Jefferson Lab, Newport News, VA, United States, July 2002. URL http://hallaweb.jlab.org/publications/Technotes/ files/2002/02-012.pdf.

[78] C. Gu, Spectrometer optics study for E08-027. Technical report, University of Virginia, Charlottesville, VA, United States, January 2016.

[79] Hall A Collaboration, Event Scanning Program for Hall A Collaboration Experiments, Technical report, Jefferson Lab, Newport News, VA, United States, August 2002.

[80] J. Liu, Radiation Effects in Simulation, Technical Report, University of Virginia, Virginia, USA, May 2015.

[81] C. Gu, Target Field Mapping and Uncertainty Estimation. Technical Report, University of Virginia, Charlottesville, VA, United States, 2015.

[82] C.W. De Jager, et al., Atom. Data Nucl. Data Tab., 14(5):479-508, 1974.

[83] J. W. Lightbody, J. S. OConnell, Computers in Phys., 2(3):57-64, 1988.

[84] P. E. Bosted, V. Mamyan, arXiv:1203.2262.

[85] R. Brun and F. Rademakers, ROOT - An Object Oriented Data Analysis Framework, Proceedings AIHENP'96 Workshop, Lausanne, Sep. 1996, Nucl. Inst. & Meth. in Phys. Res. A 389 (1997) 81-86. See also http://root.cern.ch/.

[86] P. Bevington, Data Reduction and Error Analysis for the Physical Sciences, (McGraw-Hill Inc., 2003).

[87] K. Heyde, Basic Ideas and Concepts in Nuclear Physics: An Introductory Approach, (The Institute of Physics Publishing, Bristol UK, 2004).

[88] M. Paolone et al., Phys. Rev. Lett. 105, 072001, 2010.